

SCALE 6.2.4 Validation: Radiation Shielding



Cihangir Celik
Douglas E. Peplow
Mathieu N. Dupont
Georgeta Radulescu

November 2022



DOCUMENT AVAILABILITY

Reports produced after January 1, 1996, are generally available free via OSTI.GOV.

Website www.osti.gov

Reports produced before January 1, 1996, may be purchased by members of the public from the following source:

National Technical Information Service
5285 Port Royal Road
Springfield, VA 22161
Telephone 703-605-6000 (1-800-553-6847)
TDD 703-487-4639
Fax 703-605-6900
E-mail info@ntis.gov
Website <http://classic.ntis.gov/>

Reports are available to DOE employees, DOE contractors, Energy Technology Data Exchange representatives, and International Nuclear Information System representatives from the following source:

Office of Scientific and Technical Information
PO Box 62
Oak Ridge, TN 37831
Telephone 865-576-8401
Fax 865-576-5728
E-mail reports@osti.gov
Website <http://www.osti.gov/>

This report was prepared as an account of work sponsored by an agency of the United States Government. Neither the United States Government nor any agency thereof, nor any of their employees, makes any warranty, express or implied, or assumes any legal liability or responsibility for the accuracy, completeness, or usefulness of any information, apparatus, product, or process disclosed, or represents that its use would not infringe privately owned rights. Reference herein to any specific commercial product, process, or service by trade name, trademark, manufacturer, or otherwise, does not necessarily constitute or imply its endorsement, recommendation, or favoring by the United States Government or any agency thereof. The views and opinions of authors expressed herein do not necessarily state or reflect those of the United States Government or any agency thereof.

Nuclear Energy and Fuel Cycle Division

SCALE 6.2.4 VALIDATION: RADIATION SHIELDING

Cihangir Celik
Douglas E. Peplow
Mathieu N. Dupont
Georgeta Radulescu

November 2022

Prepared by
OAK RIDGE NATIONAL LABORATORY
Oak Ridge, TN 37831
managed by
UT-BATTELLE, LLC
for the
US DEPARTMENT OF ENERGY
under contract DE-AC05-00OR22725

CONTENTS

LIST OF FIGURES	v
LIST OF TABLES	ix
ABBREVIATIONS	xi
ABSTRACT.....	1
1. SCALE SHIELDING CAPABILITIES.....	1
1.1 MAVRIC.....	1
1.1.1 CADIS.....	2
1.1.2 FW-CADIS	2
2. VALIDATION MODELS AND RESULTS	3
2.1 NEUTRON TRANSMISSION THROUGH AN IRON SPHERE.....	3
2.1.1 Benchmark Model.....	4
2.1.2 Benchmark Results	6
2.2 NEUTRONS THROUGH A HEAVY WATER SPHERE.....	9
2.2.1 Benchmark Model.....	9
2.2.2 Benchmark Results	12
2.3 CONCRETE LABYRINTH	15
2.3.1 Benchmark Model.....	15
2.3.2 Benchmark Results	19
2.4 AM-BE NEUTRON LEAKAGE THROUGH SEVERAL MATERIALS	39
2.4.1 Benchmark Model.....	39
2.4.2 Benchmark Results	40
2.5 D-T NEUTRONS THROUGH AN IRON SPHERE.....	50
2.5.1 Benchmark Model.....	50
2.5.2 Benchmark Results	50
2.6 UEKI SHIELDING MEASUREMENTS	52
2.6.1 Benchmark Model.....	52
2.6.2 Benchmark Results	55
2.7 SKYSHINE BENCHMARK	64
2.7.1 Benchmark Model.....	66
2.7.2 Benchmark Results	66
2.8 SILENE CRITICAL ASSEMBLY BENCHMARK.....	68
2.8.1 Benchmark Model.....	68
2.8.2 Benchmark Results	71
3. SUMMARY	72
4. REFERENCES	73

LIST OF FIGURES

Figure 1. Simplified iron sphere model.	4
Figure 2. Detailed iron sphere model.	5
Figure 3. ^{252}Cf neutron source distributions given by Sajo et al. [10].	5
Figure 4. Calculated and measured neutron fluxes by NRI with the simplified model.	7
Figure 5. Calculated and measured neutron fluxes by Skoda with the simplified model.	7
Figure 6. Neutron mean free path (mfp) in iron and neutron flux spectra for the iron sphere.	8
Figure 7. Calculated and measured neutron fluxes by Skoda with the detailed model.	8
Figure 8. Calculated and measured neutron fluxes by NRI with the detailed model.	9
Figure 9. Unit 3: A8 source design (height 2.5 cm).	11
Figure 10. Unit 81: source holder for A8 source (height ≈ 16 cm).	11
Figure 11. Unit 4: A25 source to contain A8 (height 3.5 cm).	11
Figure 12. Unit 5: holder for A25 source (height ≈ 17.9 cm).	11
Figure 13. Model of fully assembled A8 configuration (radius 15 cm).	11
Figure 14. Model of the fully assembled A25 configuration with the spherical shell segment tally zone 75 cm from the center of the sphere and wrapping around 360°	12
Figure 15. Measured fluxes (per unit source) for the A8 source as a function of neutron energy and MAVRIC-simulated values.	13
Figure 16. Ratio of the MAVRIC-simulated fluxes to the measured fluxes for the A8 source as a function of neutron energy.	13
Figure 17. Measured fluxes (per unit source) for the A25 source as a function of neutron energy and MAVRIC-simulated values.	14
Figure 18. Ratio of the MAVRIC-simulated fluxes to the measured fluxes for the A25 source as a function of neutron energy.	14
Figure 19. Horizontal section of the labyrinth, corresponding to Case 1.	15
Figure 20. View of the labyrinth from the front at the Cut A.	15
Figure 21. Case 2: polyethylene plates covered by 0.08 cm of cadmium, placed in the first corner of the labyrinth (see Figure 22).	16
Figure 22. Cases 2 and 3, polyethylene plate dimensions in the first corner of the labyrinth.	16
Figure 23. Case 4: borated concrete plates in the first and second corners of the labyrinth.	17
Figure 24. Case 5: polyethylene plates in the middle of the second straight section of the labyrinth.	17
Figure 25. Case 6, dead end at the end of the first straight section of the labyrinth.	18
Figure 26. 2 in. Bonner sphere detector response function.	20
Figure 27. 3 in. Bonner sphere detector response function.	21
Figure 28. 5 in. Bonner sphere detector response function.	21
Figure 29. 5 in. Bonner sphere detector response function without Cd layer.	22
Figure 30. 8 in. Bonner sphere detector response function.	22
Figure 31. 10 in. Bonner sphere detector response function.	23
Figure 32. 12 in. Bonner sphere detector response function.	23
Figure 33. Case 1A C/E calculation results ratio for the different measurement positions and all Bonner spheres.	28
Figure 34. Case 1B C/E calculation results ratio for the different measurement positions and all Bonner spheres.	28
Figure 35. Case 2A C/E calculation results ratio for the different measurement positions and all Bonner spheres.	29
Figure 36. Case 2B C/E calculation results ratio for the different measurement positions and all Bonner spheres.	29
Figure 37. Case 3A C/E calculation results ratio for the different measurement positions and all Bonner spheres.	30

Figure 38. Case 3B C/E calculation results ratio for the different measurement positions and all Bonner spheres.....	30
Figure 39. Case 4A C/E calculation results ratio for the different measurement positions and all Bonner spheres.....	31
Figure 40. Case 4B C/E calculation results ratio for the different measurement positions and all Bonner spheres.....	31
Figure 41. Case 5A C/E calculation results ratio for the different measurement positions and all Bonner spheres.....	32
Figure 42. Case 6A C/E calculation results ratio for the different measurement positions and all Bonner spheres.....	32
Figure 43. Case 6B C/E calculation results ratio for the different measurement positions and all Bonner spheres.....	33
Figure 44. Case 1A MAVRIC/MCNP calculation results ratio for the different measurement positions and all Bonner spheres.....	34
Figure 45. Case 1B MAVRIC/MCNP calculation results ratio for the different measurement positions and all Bonner spheres.....	34
Figure 46. Case 2A MAVRIC/MCNP calculation results ratio for the different measurement positions and all Bonner spheres.....	35
Figure 47. Case 2B MAVRIC/MCNP calculation results ratio for the different measurement positions and all Bonner spheres.....	35
Figure 48. Case 3A MAVRIC/MCNP calculation results ratio for the different measurement positions and all Bonner spheres.....	36
Figure 49. Case 3B MAVRIC/MCNP calculation results ratio for the different measurement positions and all Bonner spheres.....	36
Figure 50. Case 4A MAVRIC/MCNP calculation results ratio for the different measurement positions and all Bonner spheres.....	37
Figure 51. Case 4B MAVRIC/MCNP calculation results ratio for the different measurement positions and all Bonner spheres.....	37
Figure 52. Case 5A MAVRIC/MCNP calculation results ratio for the different measurement positions and all Bonner spheres.....	38
Figure 53. Case 6A MAVRIC/MCNP calculation results ratio for the different measurement positions and all Bonner spheres.....	38
Figure 54. Case 6B MAVRIC/MCNP calculation results ratio for the different measurement positions and all Bonner spheres.....	39
Figure 55. Leakage flux measurements and MAVRIC simulation from the Case 1 bare source module.....	41
Figure 56. Ratio of the MAVRIC-simulated leakage fluxes to the measurements from the Case 1 bare source module.	42
Figure 57. Leakage flux measurements and MAVRIC simulation from the Case 2 beryllium spherical shell.	42
Figure 58. Ratio of the MAVRIC-simulated leakage fluxes to the measurements from the Case 2 beryllium spherical shell.	43
Figure 59. Leakage flux measurements and MAVRIC simulation from the Case 3 polyethylene spherical shell.....	43
Figure 60. Ratio of the MAVRIC-simulated leakage fluxes to the measurements from the Case 3 polyethylene spherical shell.....	44
Figure 61. Leakage flux measurements and MAVRIC simulation from the Case 4 lead spherical shell.	44
Figure 62. Ratio of the MAVRIC-simulated leakage fluxes to the measurements from the Case 4 lead spherical shell.....	45

Figure 63. Leakage flux measurements and MAVRIC simulation from the Case 5 niobium spherical shell.	45
Figure 64. Ratio of the MAVRIC-simulated leakage fluxes to the measurements from the Case 5 niobium spherical shell.	46
Figure 65. Leakage flux measurements and MAVRIC simulation from the Case 6 molybdenum spherical shell.	46
Figure 66. Ratio of the MAVRIC-simulated leakage fluxes to the measurements from the Case 6 molybdenum spherical shell.	47
Figure 67. Leakage flux measurements and MAVRIC simulation from the Case 7 tantalum spherical shell.	47
Figure 68. Ratio of the MAVRIC-simulated leakage fluxes to the measurements from the Case 7 tantalum spherical shell.	48
Figure 69. Leakage flux measurements and MAVRIC simulation from the Case 8 small tungsten spherical shell.	48
Figure 70. Ratio of the MAVRIC-simulated leakage fluxes to the measurements from the Case 8 small tungsten spherical shell.	49
Figure 71. Leakage flux measurements and MAVRIC simulation from the Case 9 large tungsten spherical shell.	49
Figure 72. Ratio of the MAVRIC-simulated leakage fluxes to the measurements from the Case 9 large tungsten spherical shell.	50
Figure 73. Measured values of the neutron leakage spectrum from a D-T/D-D source inside an iron sphere and the MAVRIC simulation results.	51
Figure 74. Type 1 measurement geometry: ^{252}Cf source at the apex of a cone cutout in a 50 cm paraffin cube (yellow) with different thicknesses of a single material (light gray) and a neutron detector (N).	52
Figure 75. Type 2 measurement geometry: 25 cm of stainless steel (gray) and different thicknesses of polyethylene (green).	53
Figure 76. Type 3 measurement geometry – 15 cm of polyethylene (green) at different positions in stainless steel (gray) for a total of 40 cm thickness.	53
Figure 77. Response functions for computing neutron dose rate ($\mu\text{Sv/h}$) per unit flux ($\text{n cm}^{-2} \text{s}^{-1}$) using a log-log plot.	56
Figure 78. Response functions for computing neutron dose rate ($\mu\text{Sv/h}$) per unit flux ($\text{n cm}^{-2} \text{s}^{-1}$), using a semi-log plot.	57
Figure 79. Type 1 measurements: ratio of simulated to measured dose rates with varying thicknesses of polyethylene.	58
Figure 80. Type 1 measurements: ratio of simulated to measured dose rates with varying thickness of NS4-FR.	58
Figure 81. Type 1 measurements: ratio of simulated to measured dose rate with varying thickness of Resin-F.	59
Figure 82. Type 1 measurements: ratio of simulated-to-measured dose rate with varying thickness of KRAFTON-HB.	60
Figure 83. Type 1 measurements: ratio of simulated-to-measured dose rate with varying thickness of SUS-304 (stainless steel).	60
Figure 84. Type 2 measurement: ratio of simulated-to-measured dose rate with 25 cm of steel first and a varying thickness of polyethylene second.	61
Figure 85. Type 2 measurement: ratio of simulated-to-measured dose rate with a varying thickness of polyethylene first and a 25 cm of stainless steel second.	62
Figure 86. Type 3 measurement: ratio of simulated-to-measured neutron dose rate with a varying position of 15 cm polyethylene in a 40 cm steel/polyethylene shield.	62
Figure 87. Type 3 measurement: ratio of simulated-to-measured photon dose rate with a varying position of 15 cm polyethylene in a 40 cm steel/polyethylene shield.	63

Figure 88. Type 3 measurement: ratio of simulated-to-measured total dose rate with a varying position of 15 cm polyethylene in a 40 cm steel/polyethylene shield.	63
Figure 89. Type 3 measurement: measured and simulated dose rates as a function of the position of the polyethylene with a 40 cm steel/polyethylene shield.....	64
Figure 90. Schematic of the silo used in the experiment, corresponding to Fig. 2–4 from [36].	65
Figure 91. Topography of KSU Nuclear Engineering Shielding Facility, corresponding to Figures 1–3 from [1].	65
Figure 92. SCALE MAVRIC model of the silo used in the experiment.	66
Figure 93. Radial distribution of the exposure rate calculated by MAVRIC for the source with 3804 Ci activity.....	68
Figure 94. Experimental setup for SILENE Pulse 1 [43].	69
Figure 95. Benchmark model of SILENE Pulse 1.	69
Figure 96. SILENE assembly model.....	70
Figure 97. Fission rate spectrum for SILENE Pulse 1 [43].	70

LIST OF TABLES

Table 1. Composition of materials used in the iron sphere experiments.	3
Table 2. Summary of Concrete labyrinth configurations and Cases studied.	18
Table 3. Summary of experiment measurement points ordered by concrete labyrinth configuration.	19
Table 4. Summary of MAVRIC and MCNP benchmark calculation points ordered by concrete labyrinth configuration.	19
Table 5. MAVRIC calculation results (pulses per second) for Case 1A.	24
Table 6. MAVRIC calculation results (pulses per second) for Case 1B.	24
Table 7. MAVRIC calculation results (pulses per second) for Case 2A.	24
Table 8. MAVRIC calculation results (pulses per second) for Case 2B.	25
Table 9. MAVRIC calculation results (pulses per second) for Case 3A.	25
Table 10. MAVRIC calculation results (pulses per second) for Case 3B.	25
Table 11. MAVRIC calculation results (pulses per second) for Case 4A.	26
Table 12. MAVRIC calculation results (pulses per second) for Case 4B.	26
Table 13. MAVRIC calculation results (pulses per second) for Case 5A.	26
Table 14. MAVRIC calculation results (pulses per second) for Case 6A.	27
Table 15. MAVRIC calculation results (pulses per second) for Case 6B.	27
Table 16. Summary of Am-Be source module spherical shells cases studied.	40
Table 17. Measured values from Type 1 measurements, read from Ueki et al. [29] Figure 2.	54
Table 18. Measured values from Type 2 measurements, read from Ueki et al. [29], Figure 3.	54
Table 19. Measured values, read from Ueki et al. [29], Figure 4.	54
Table 20. Measured values from Type 3 measurements, read from Ueki et al. [29], Figure 8.	54
Table 21. Measured values from Type 1 measurements using polyethylene, read from Ueki et al. [29] Figures 2 and 4: results should be the same.	55
Table 22. Measured values from measurements using 25 cm of stainless steel and various thicknesses of polyethylene, taken from different Ueki et al. [29] Figures 2–4: results should be the same.	55
Table 23. Measured values from Type 3 measurements, comparing the total dose rate to the sum of the neutron and photon dose rates: results should be the same.	55
Table 24. Comparison of exposure rates between measurement and calculation.	67
Table 25. Comparison of SILENE Pulse 1 benchmark results using IRDF [44] responses.	71

ABBREVIATIONS

1D	one-dimensional
3D	three-dimensional
CA	Collimator A
CAAS	criticality accident alarm system
CADIS	Consistent Adjoint Driven Important Sampling
CE	continuous energy
CEA	Commissariat a l'Energie Atomique
D-T	deuterium-tritium
DOE	US Department of Energy
ENDF	Evaluated Nuclear Data File
FF	free field
FW-CADIS	Forward Weighted Consistent Adjoint Driven Important Sampling
HPIC	high-pressure ionization chamber
ICRP	International Commission on Radiological Protection
ICRU	International Commission on Radiation Units
ICSBEP	International Criticality Safety Benchmark Evaluation Project
kerma	kinetic energy release in materials
KSU	Kansas State University
MAVRIC	Monaco with Automated Variance Reduction using Importance Calculations
MC	Monte Carlo
MCNP	Monte Carlo N-Particle
NASA	National Aeronautics and Space Administration
NRI	National Research Institute of the Czech Republic
ORNL	Oak Ridge National Laboratory
PC	personal computer
PNNL	Pacific Northwest National Laboratory
RSICC	Radiation Safety Information Computational Center
SGGP	SCALE General Geometry Package
SINBAD	Shielding Integral Benchmark Archive & Database
TLDs	thermoluminescent dosimeters

ABSTRACT

For safe and reliable use of computer codes by the community, accuracy must be clearly evaluated. In particular, the nuclear reactor engineering and licensing field needs accurate tools for radiation shielding modeling. Monaco with Automated Variance Reduction using Importance Calculations (MAVRIC) is one such tool, with built-in variance reduction methods distributed within the SCALE code, and its validity is demonstrated in this report for the released version 6.2.4. Representative benchmarks corresponding to shielding analysis are selected for the validation study. Typical experimental results analyzed from those benchmarks include neutron fluxes, detector count rates, detector energy response functions, neutron and gamma doses, foil neutron activation rates and activities, neutron leakage fluxes, and skyshine dose rates. Thousands of points of comparison between experiment and calculation are presented in this work. Other than rare outliers typically explained by either a lack of information or large uncertainties in the experiment conditions, material, or dimensions, MAVRIC agrees well with the experiment results. MAVRIC is also compared to Monte Carlo N-Particle (MCNP) calculations when available, and both codes generally produce good agreements within estimated uncertainties. The selected benchmarks are obtained from reliable sources such as the *International Criticality Safety Benchmark Evaluation Project Handbook* (ICSBEP Handbook), the Shielding Integral Benchmark Archive & Database (SINBAD), and other shielding validation work found in the literature. Additional datapoints and benchmarks will be added to future versions of this report to incrementally expand the shielding validation suite incrementally.

1. SCALE SHIELDING CAPABILITIES

SCALE [1], developed and maintained by Oak Ridge National Laboratory (ORNL), is a collection of modules/computer codes used to model nuclear physics phenomena with a focus on nuclear reactor engineering and licensing. This report focuses on validation of SCALE's data and methods for radiation shielding applications. The SCALE module for radiation shielding is the Monaco with Automated Variance Reduction using Importance Calculations (MAVRIC) Monte Carlo code [2]. MAVRIC and its main characteristics are briefly described in the following subsections.

1.1 MAVRIC

MAVRIC is the radiation shielding sequence in SCALE. Monte Carlo calculations in the MAVRIC sequence use Monaco, which can be run with either continuous energy (CE) or multigroup (MG) cross sections. Models used in MAVRIC are created using the SCALE General Geometry Package (SGGP). MAVRIC computes cross sections for Denovo [3] to perform discrete ordinates calculations and to form an importance map and biased source distribution for variance reduction. The cross sections are computed by mixing materials in the model via superimposing a spatial mesh for Denovo calculations. Mixed materials are represented as macromaterials in which the volume fraction of the individual materials for each voxel of the mesh is used to perform calculations. In a MAVRIC calculation, the user must specify several blocks of information: material compositions, geometry, definitions (locations, response functions, grid geometries, distributions), sources (spatial, energy and direction), tallies (region tallies, point detector, mesh tallies), basic calculation parameters, and variance reduction parameters. KENO-VI and MAVRIC can be combined to perform Criticality Accident Alarm System (CAAS) analysis using KENO-VI to create a fission source containing spatial and energy distributions. The distributions are then imported by MAVRIC on a mesh to be used as a fixed-source definition of fission neutrons.

1.1.1 CADIS

Consistent Adjoint Driven Important Sampling (CADIS) [4] is a variance reduction method which optimizes the calculation sampling process to get more particles to an area of interest, such as a region tally or point detector. The CADIS process utilizes a moderate-fidelity adjoint deterministic calculation to create weight windows (based on the adjoint flux) and a consistently biased source. The weight windows and biased source can provide significant reductions in the computational time required to obtain a well-converged Monte Carlo solution.

1.1.2 FW-CADIS

The Forward-Weighted Consistent Adjoint Driven Important Sampling (FW-CADIS) method [5] is a variance reduction technique which was developed to optimize multiple tallies simultaneously. It can be considered to be an extension of the CADIS method. In some problems, multiple tallies at different locations must be optimized. Instead of running separate CADIS-optimized calculations for each tally, FW-CADIS allows for a simultaneous optimization by creating a weighted adjoint source. The weighting factors for the adjoint source locations are based on a moderate-fidelity forward discrete ordinates calculation. Using this weighted adjoint source description, an adjoint discrete ordinates calculation is then run to obtain the weight windows and biased source, as in the CADIS method.

2. VALIDATION MODELS AND RESULTS

The SCALE MAVRIC 6.2.4 simulations described in this report used either CE AMPX cross-section libraries generated from Evaluated Nuclear Data File (ENDF)/B-VII.1 nuclear data [6] or ENDF/B-VII.0 multi-group (200 neutron groups and 47 gamma groups) for all the validation models. In some of the following benchmarks, previous analysis was performed by the community using the Monte Carlo N-Particle (MCNP) code [7]. It is also important to validate SCALE against other codes, so MCNP results are sometimes shown and used for comparison purposes. Common sources for cases are from the *International Criticality Safety Benchmark Evaluation Project Handbook* (ICSBEP Handbook) [8], the Shielding Integral Benchmark Archive & Database (SINBAD) [9], and other shielding work found in the literature.

2.1 NEUTRON TRANSMISSION THROUGH AN IRON SPHERE

In the 1990s, a set of experiments was conducted by Sajo et al. to investigate neutron transmission through an iron sphere [10]. These experiments also have been used to validate SCALE cross-section libraries and the MAVRIC sequence [2, 11]. Experiments were focused on assessing iron neutron inelastic scattering cross sections released with the ENDF/B-VI nuclear data libraries [12]. Among the available configurations used in the experiments, only one configuration—in which a ^{252}Cf neutron source is located at the center of the iron sphere—was selected for the validation of the MAVRIC sequence in this study.

The selected experiment for the validation includes an iron sphere with a radius of 25 cm suspended in the air and a neutron flux detector located 1 m away from the center of the sphere. Compositions of important materials used in the experiment are listed in Table 1. Neutron flux measurements were performed by two independent teams of researchers, one from Skoda Company, and one from the National Research Institute of the Czech Republic (NRI). Each team used their own equipment, and each set of equipment had its own energy grouping for the neutron spectrum.

Table 1. Composition of materials used in the iron sphere experiments.

Component	Composition weight percent (%)		Component	Composition weight percent (%)	
Iron sphere	^{54}Fe	5.767	Transport box and guide tubes	^{27}Al	93.900
	^{56}Fe	91.168		Cu	4.000
	^{57}Fe	2.187		^{54}Fe	0.0406
	^{58}Fe	0.298		^{56}Fe	0.6419
	C	0.070		^{57}Fe	0.0154
	P	0.030		^{58}Fe	0.0021
	S	0.030		Mg	0.500
Stainless steel encapsulation	^{54}Fe	4.071	Si	0.500	
	^{56}Fe	64.371	Mn	0.400	
	^{57}Fe	1.544	Ca	32.130	
	^{58}Fe	0.211	Si	3.448	
	Cr	18.595	^{27}Al	1.083	
	Ni	9.813	^{23}Na	0.0271	
	Mn	1.395	K	0.1138	

Table 1. Composition of materials used in the iron sphere experiments (continued).

Component	Composition weight percent (%)		Component	Composition weight percent (%)	
Dry air				O	41.020
				C	17.520
				Mg	3.265
				H	0.6187
				⁵⁴ Fe	0.0439
				⁵⁶ Fe	0.7153
				⁵⁷ Fe	0.0168
				⁵⁸ Fe	0.0023

2.1.1 Benchmark Model

Given that a ²⁵²Cf neutron source has a fast neutron source spectrum, some simplifications can be made by either homogenizing or ignoring some detailed structures and materials used in the experiment. Two models were developed for validation purposes. To take advantage of the fast neutron spectrum and symmetry of the experimental setup, a simplified model was developed in which the sphere is located in a vacuum, and a spherical region tally is modeled around the iron sphere, as shown in **Error! Reference source not found.**

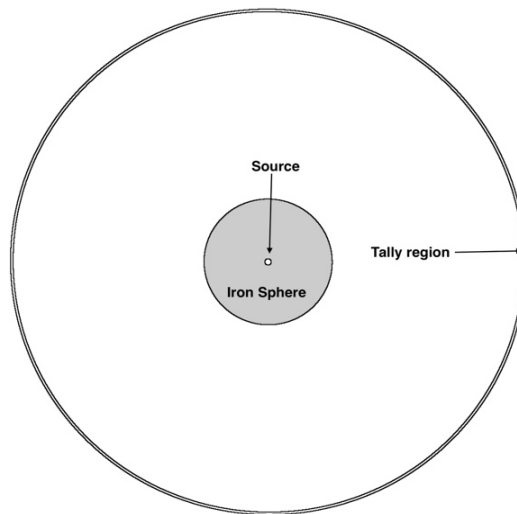


Figure 1. Simplified iron sphere model.

The simplified model ignores the details of the stainless steel source encapsulation and assumes that everything is uniform and symmetric inside the iron sphere. This allows for the spherical tally region to be used without any variance reduction methods other than the implicit capture approximation.

The second model, referred to as the *detailed model*, has more detailed regions. The detailed model includes the source holder comprising a double-layer stainless steel tube and guiding tubes made of aluminum. Dry air is around the sphere, and a 50 cm thick concrete pad is 1.5 m below the center of the sphere. The CADIS variance reduction method was used to optimize neutron flux in a tally ring around the beltline of the sphere, as shown in Figure 2.

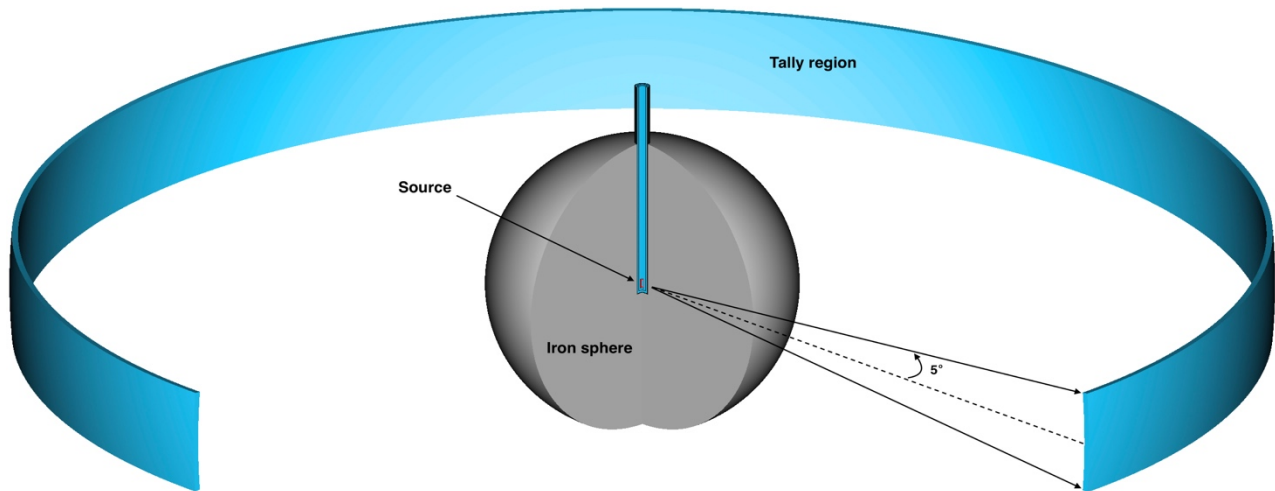


Figure 2. Detailed iron sphere model.

The tally region is constructed to span 5° upwards and downwards from the source center instead of from a single point. This is done to enhance the tally results while minimizing the impact of the asymmetry due to the source holder. The neutron source distribution for the ^{252}Cf is given by Sajo et al. [10] and is also shown in Figure 3.

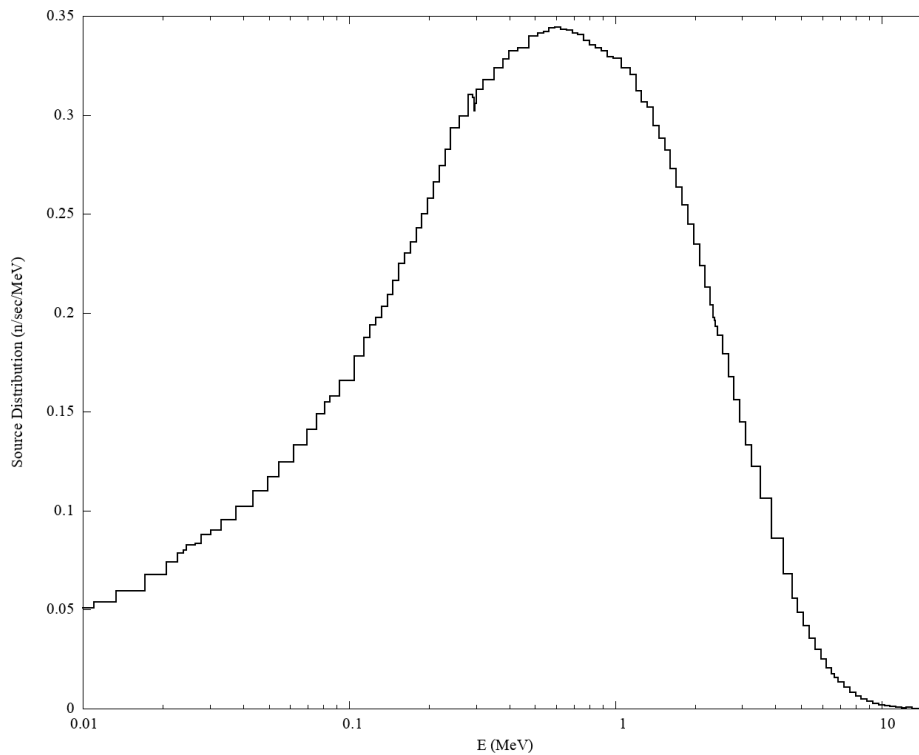


Figure 3. ^{252}Cf neutron source distributions given by Sajo et al. [10].

2.1.2 Benchmark Results

The neutron fluxes for the simplified model are compared to the measured fluxes in Figure 4 and Figure 5 with energy group structures relevant to measured flux spectra by Skoda and NRI. Because the ^{252}Cf source has a fast energy spectrum, as shown in Figure 3, there is good agreement between the measured and simulated neutron flux spectra for energies between 100 keV and 6 MeV. Ratio of the calculated to measured spectra are mostly less than 1.5 over this energy range, and even less for energies between 1 and 6 MeV. Some of the discrepancies between the calculated and measured spectra can be associated with high resonances within a relatively small energy window in the iron neutron cross sections that can impact resolution of the measuring equipment and yield higher uncertainties. For example, there are a few peak-like values with relatively high disagreements in the calculated results. The energy for each of these peaks corresponds to one of the resonance peaks in the cross sections. Figure 6 shows calculated and measured neutron spectra along with the neutron mean free path (mfp) to highlight the resonances in the neutron cross sections of ^{56}Fe . Larger discrepancies below 100 keV can be associated with fewer number of source particles and neutron slowing down from higher energies while making interactions in the resolved resonance region with possibly high uncertainty in the cross sections and low resolution of the detectors in the lower energies. Although the simulations yielded relatively small Monte Carlo uncertainties for the integrated scalar flux, less than 0.1%, the flux spectrum had up to 4% relative uncertainty below 200 keV whereas the measurement uncertainties were changing between 3% and 100% for the same energy region.

It was anticipated that some of the discrepancies between the neutron fluxes and the fluxes from simplified model could be resolved by introducing the major experiment components that were not included in the simplified model but were included in the detailed model. However, the neutron flux spectra from the detailed model also yielded results that were almost identical to those from the simplified model, and there were still some significant discrepancies with the measurements in the energy range below 100 keV, as shown in Figure 7 and Figure 8. Given that iron has big and narrow resonance windows around and below the mean source neutron energies, it is most likely that iron neutron cross sections, energy resolution and detection efficiency of the detector used in the measurements were the reasons for the discrepancies between the measured and calculated neutron flux values for energies lower than 1 MeV. In fact, agreement between measurements from NRI and Skoda also declines below 200 keV. Sajo et al. also concluded in their study that discrepancies could be originated from the iron cross sections and ^{252}Cf source characterization.

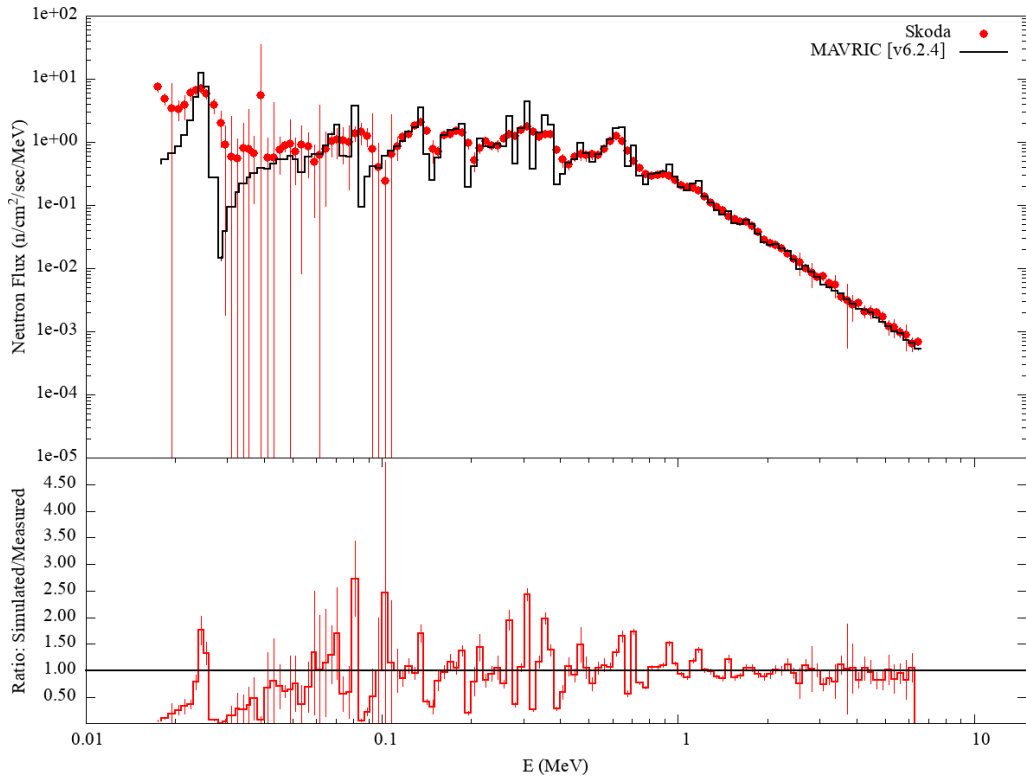


Figure 4. Calculated and measured neutron fluxes by NRI with the simplified model.

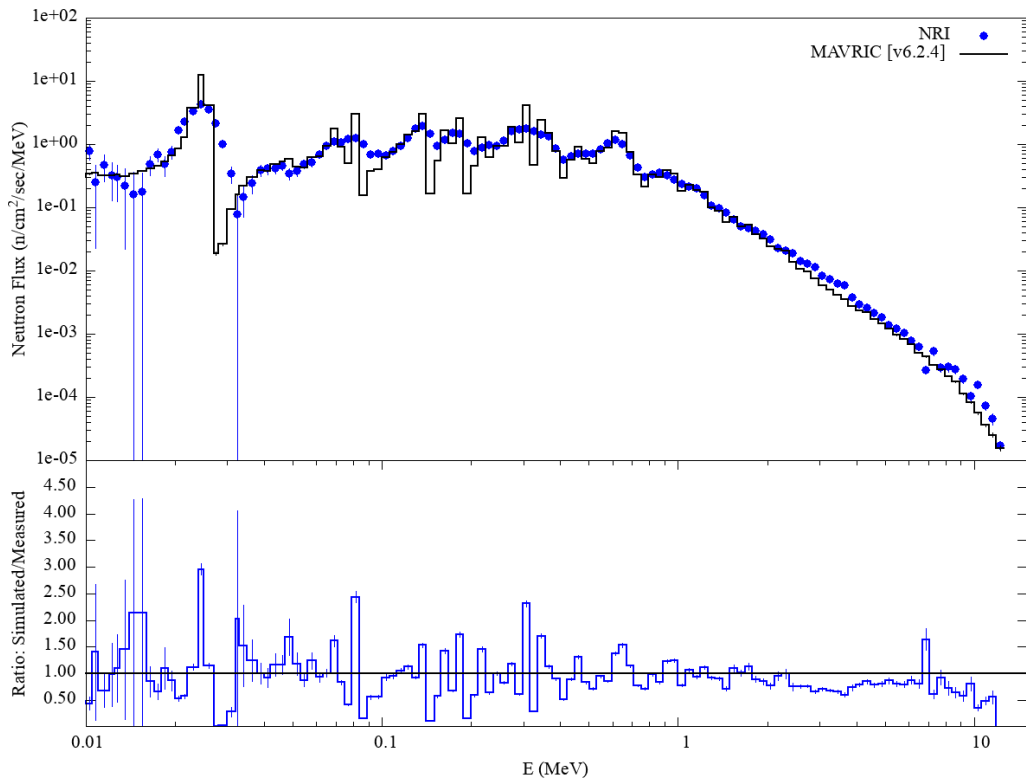


Figure 5. Calculated and measured neutron fluxes by Skoda with the simplified model.

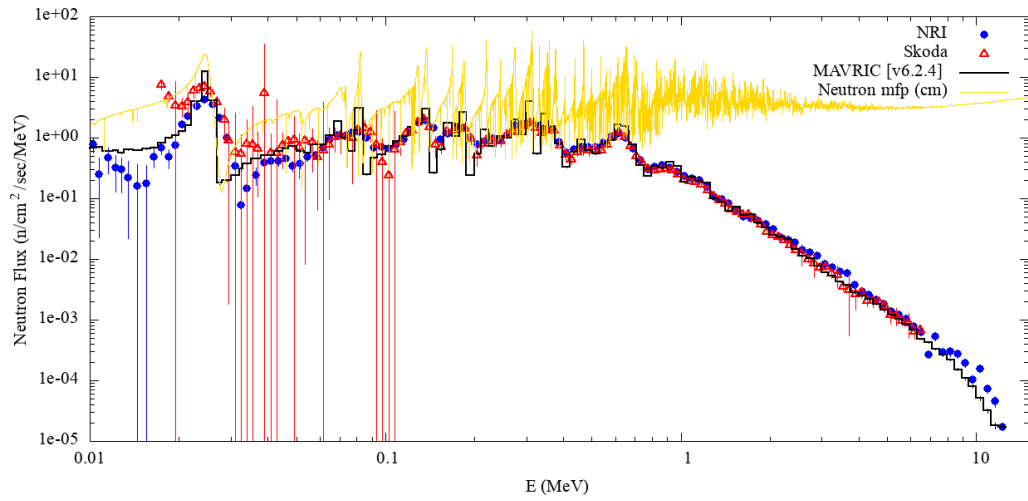


Figure 6. Neutron mean free path (mfp) in iron and neutron flux spectra for the iron sphere.

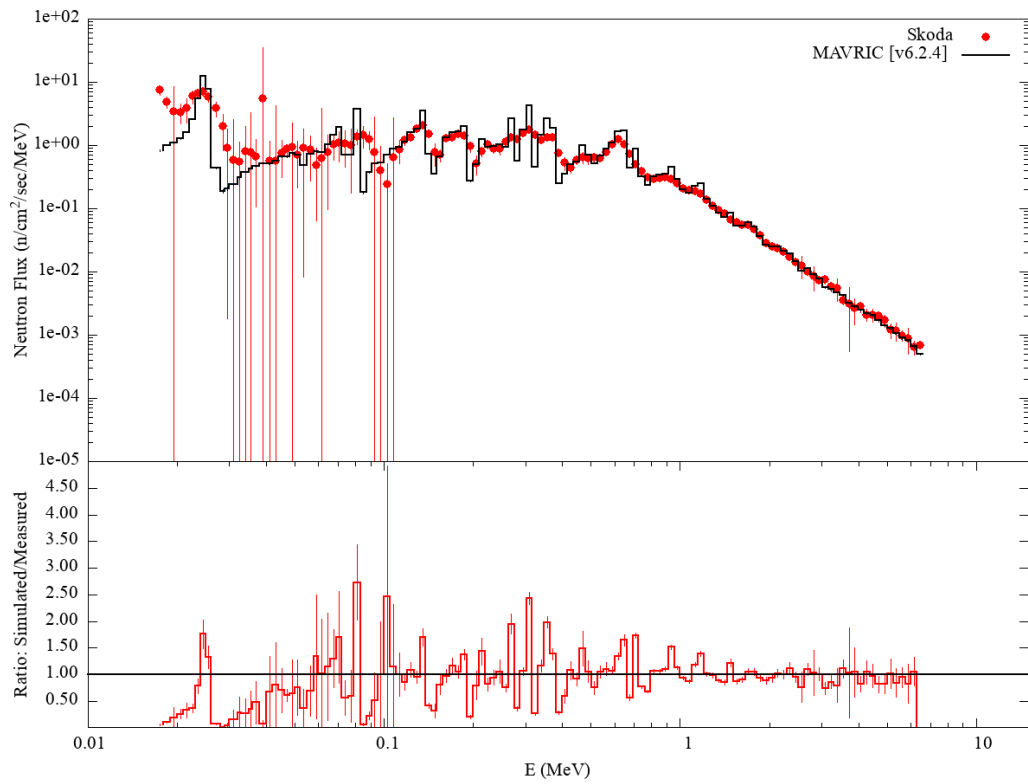


Figure 7. Calculated and measured neutron fluxes by Skoda with the detailed model.

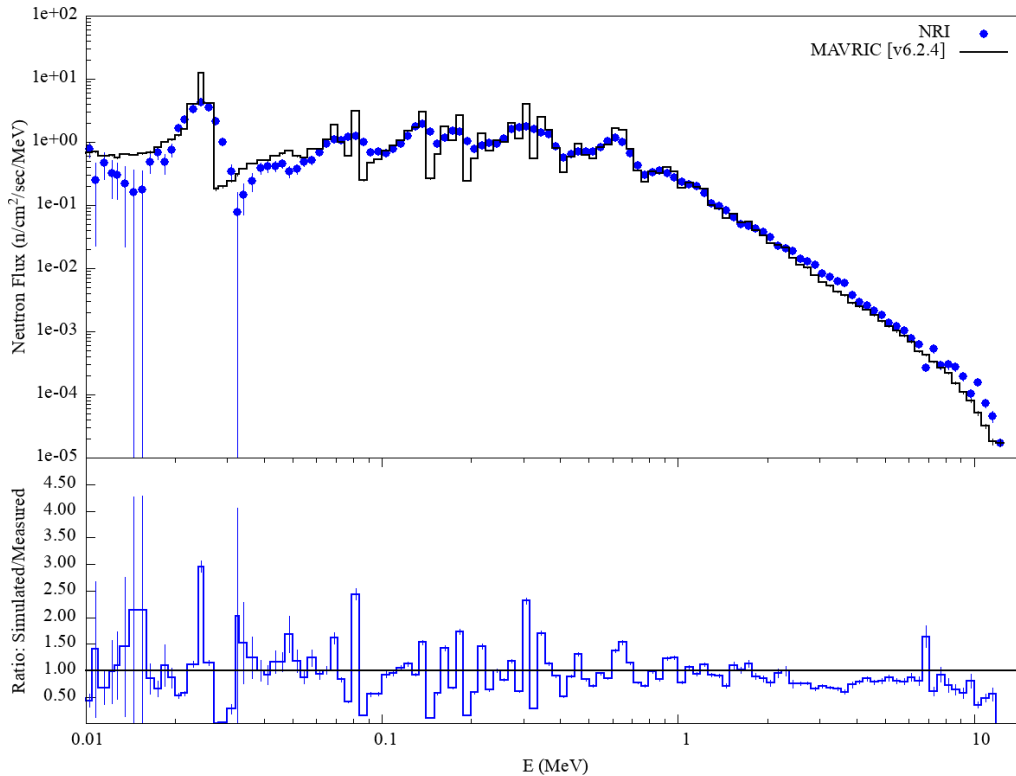


Figure 8. Calculated and measured neutron fluxes by NRI with the detailed model.

2.2 NEUTRONS THROUGH A HEAVY WATER SPHERE

Leakage measurement of ^{252}Cf neutrons through a heavy water shield was one of many measurements performed by Janský et al. in the Czech Republic in the mid-1990s [13]. The leakage spectrum was measured over a range of about 50 keV to 11 MeV using a detector placed 75 cm from the center of the sphere. The experimenters recorded many details about their measurement: the size of the hall where the measurements took place, the detailed geometry of the heavy water sphere and source holders, the recommended composition data of the materials used in the experiments, and many details about the proton recoil spectrometer that was used with stilbene and proportional counter detectors.

2.2.1 Benchmark Model

Two source configurations, A8 and A25, were used in the measurements. For each of these sources, two measurements were made: one with and one without a shadow cone of iron and borated polyethylene placed between the source and the detector. The difference between the two measurements gives a better estimate of the direct flux from the source to the detector, without scatter from the room.

The experimenters also simulated their measurements with MCNP4A using ENDF/B-IV and ENDF/B-VI cross-section data. Their calculated energy-dependent fluxes compared quite well to the measurements, but there were a few highs and lows that were not shown in the simulations. Overall, both the A8 and A25 simulations did well.

Based on the information in the paper by Janský et al. [13], models were built for the A8 and A25 source configurations. The material compositions listed by Janský et al. for steel, aluminum (two types), and heavy water were used, supplemented by SCALE's definition of standard dry air and a definition of felt from PNNL's Compendium of Material Composition Data for Radiation Transport Modeling [14]. The

models assumed that the source material was CfO₂ with a density of 10 g/cm³. With the KenoVI/MAVRIC geometry, the different pieces described in the measurement paper were built as separate units and were then combined to make the A8 or A25 model. Several of the pieces and the full models are shown in Figure 9 through Figure 14. The unit numbers correspond to the figure numbers from Janský et al. for easy comparison. For example, unit 4 is Fig. 4 in Janský et al., and unit 81 is Fig. 8(a) in Jansky et al.

The main D₂O sphere contained a vertical steel-lined channel into which the sources were loaded. This channel broke the spherical symmetry. When the A8 source was used, the channel was filled with other containers of D₂O as shown in Figure 13. If the thin steel and air gaps are ignored, then the arrangement would be close to spherically symmetrical to the channel that is nearly filled with heavy water. Note that the source itself was a long thin cylinder. When the A25 source was used as shown in Figure 14, the channel was only filled below the source, further breaking the spherical symmetry. To take advantage of the remaining azimuthal symmetry, a tally region consisting of a portion of a thin spherical shell was included all the way around the sphere. The region was approximately 10 cm in height and 75 cm from the center of the D₂O sphere. A portion of the tally region (thickness is enlarged for visibility) is shown on the right-hand side of Figure 14.

The multigroup neutron emission spectra given by Janský et al. agrees with the Watt spectrum distribution,

$$p(E) = c e^{-E/a} \sinh(\sqrt{bE}),$$

with parameters $a=1.209$ MeV and $b=0.836$ MeV⁻¹ calculated by Mannhart [15] from a variety of different measurements. Using either the table from Janský et al. or a Watt spectrum with Mannhart's parameters as the source should result in very close flux values. Because the measurement results are listed as flux per unit source, the MAVRIC source strength of $4\pi(75 \text{ cm})^2$ was set so that the total flux at the detector position without any geometry would be 1 s⁻¹.

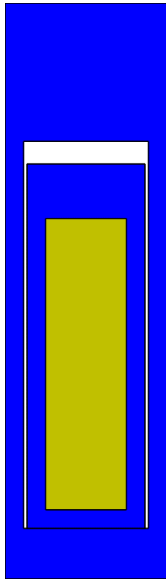


Figure 9. Unit 3:
A8 source design
(height 2.5 cm).



Figure 10. Unit 81:
source holder
for A8 source
(height ≈ 16 cm).

- Californium
- Steel
- Felt
- Aluminum
- Heavy Water

(Color legend for
all model figures)

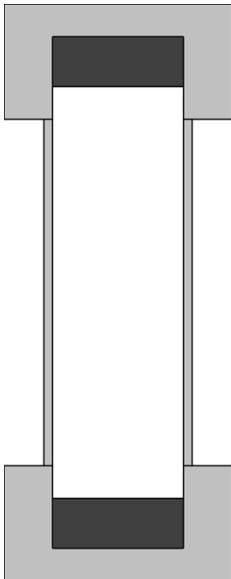


Figure 11. Unit 4:
A25 source to
contain A8
(height 3.5 cm).

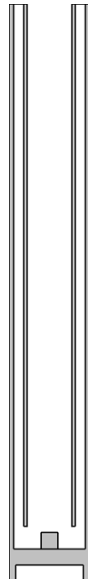


Figure 12. Unit 5:
holder for A25
source (height
 ≈ 17.9 cm).

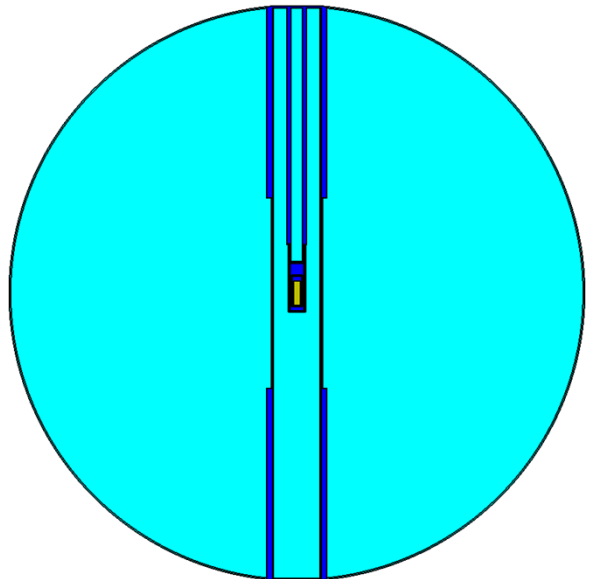


Figure 13. Model of fully assembled A8
configuration (radius 15 cm).

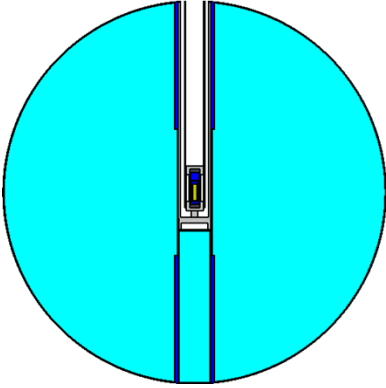


Figure 14. Model of the fully assembled A25 configuration with the spherical shell segment tally zone 75 cm from the center of the sphere and wrapping around 360°.

2.2.2 Benchmark Results

The MAVRIC sequence with FW-CADIS variance reduction was used for this calculation to obtain well converged results in each energy bin of the tally. A low-energy cutoff of 50.119 keV was applied so that neutrons below the lowest tally bin were no longer followed. All simulations were run without the shadow shield. Similar validation studies have been performed by taking the difference of two simulations, one without the shadow cone and one with the shadow cone, has been done in the past [16-19]. Because the measurements were corrected for background and room return, just a single simulation was conducted for each source, and the walls of the room were excluded. This approach seems reasonable, and the simulations match the measurements well.

Figure 15 shows the comparison of the measured and simulated fluxes for the A8 source. Note that the uncertainties for the simulations are within the size of the dots used in the plot. Like the simulations from Janský et al., a few highs and lows seen in measurements are not seen in the simulations. The simulations do match the flux depressions of those in the measurements at 0.45 and 1.0 MeV, as well as the slight dip at 3.5 MeV. Overall, simulations match the measurements well. The ratio of the simulated flux to the measured flux is shown in Figure 16. The uncertainties shown are mostly due to measurement uncertainty. The fraction of simulated values within one standard deviation of a ratio of unity is 53%, within two standard deviations is 79%, and within three standard deviations is 91%.

For the A25 source configuration, the comparison of simulated fluxes to measured fluxes is shown in Figure 17. Like the A8 source, the A25 simulations match the measurements well. The ratio of the simulations to the measured fluxes is shown in Figure 18. The fraction of simulated values within one standard deviation of a ratio of unity is 52%, within two standard deviations is 73%, and within three standard deviations is 86%.

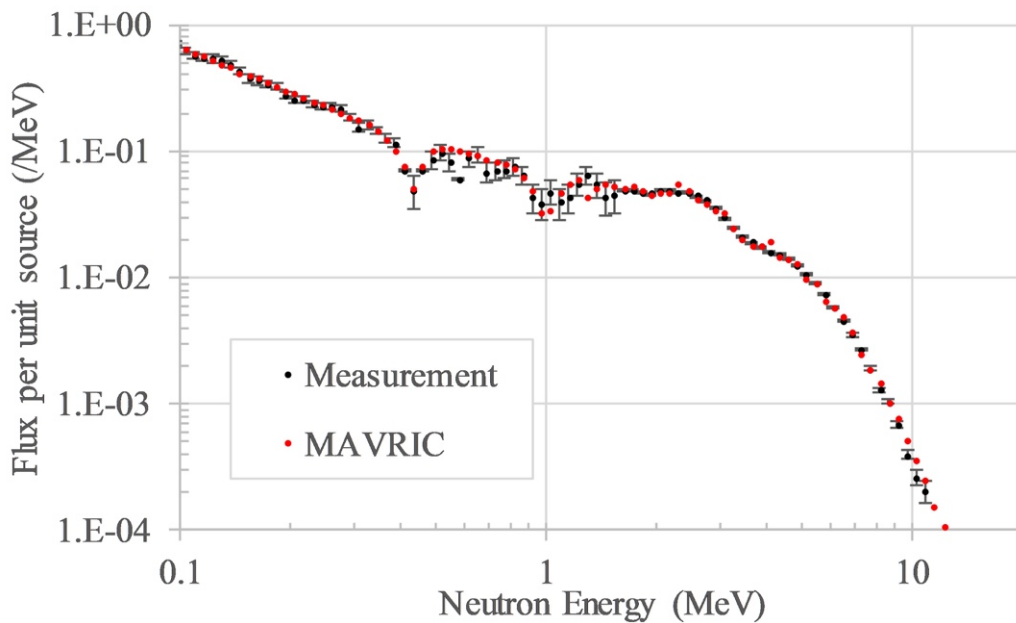


Figure 15. Measured fluxes (per unit source) for the A8 source as a function of neutron energy and MAVRIC-simulated values.

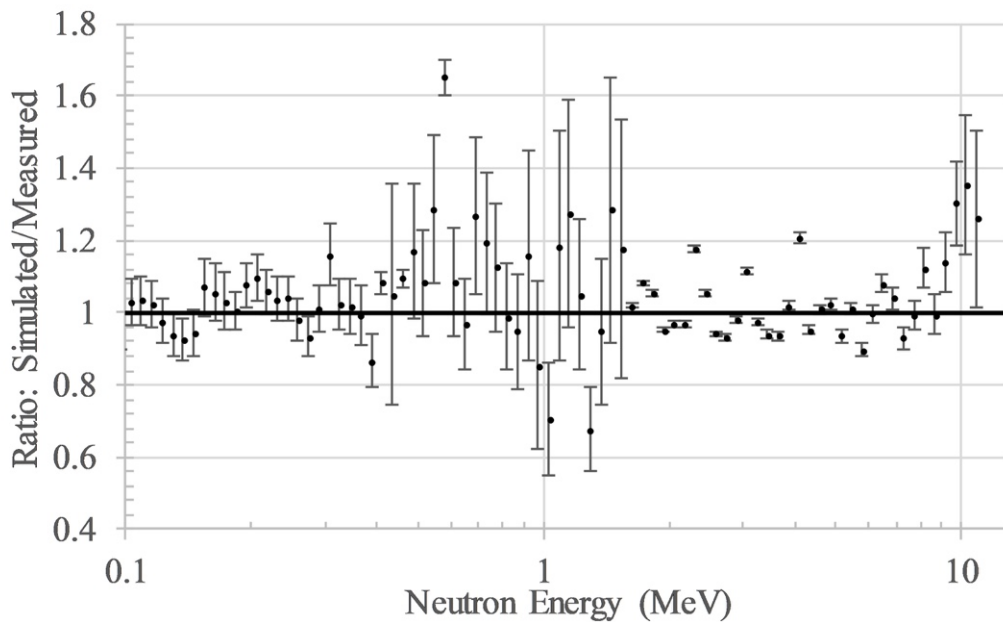


Figure 16. Ratio of the MAVRIC-simulated fluxes to the measured fluxes for the A8 source as a function of neutron energy.

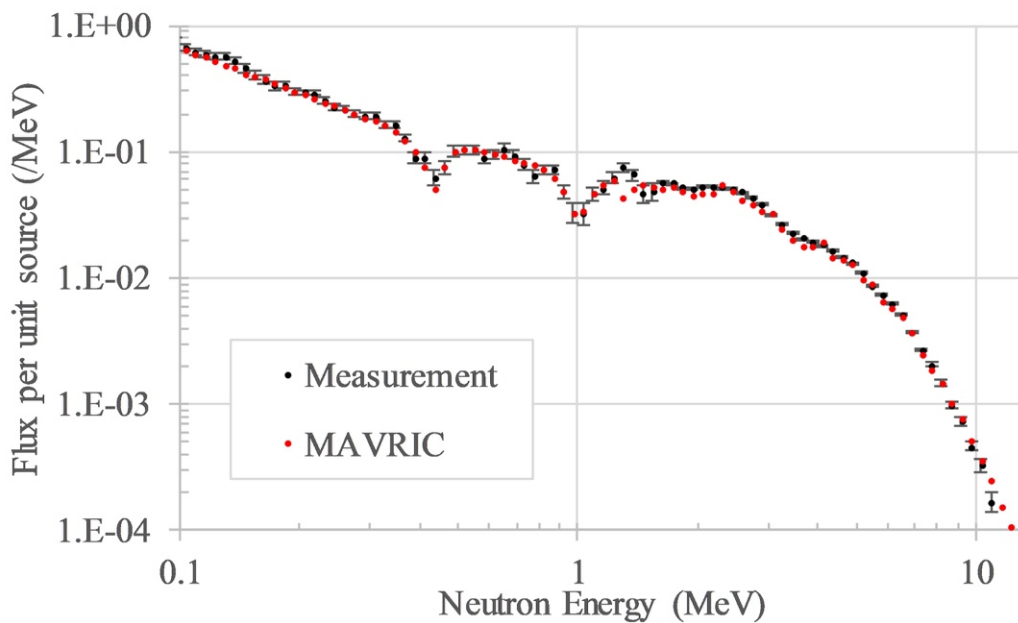


Figure 17. Measured fluxes (per unit source) for the A25 source as a function of neutron energy and MAVRIC-simulated values.

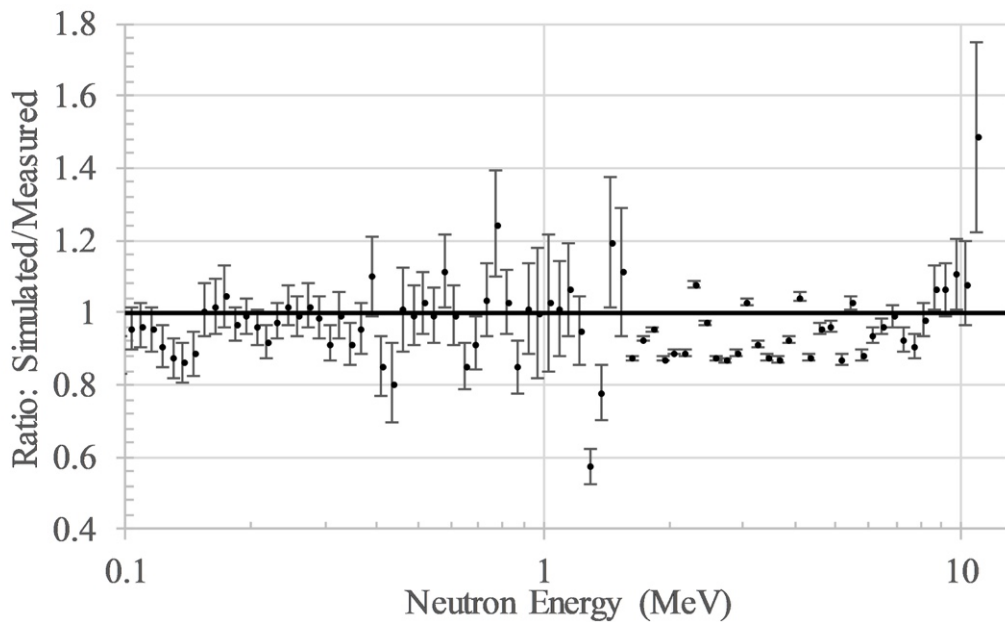


Figure 18. Ratio of the MAVRIC-simulated fluxes to the measured fluxes for the A25 source as a function of neutron energy.

2.3 CONCRETE LABYRINTH

Neutron flux measurements in a large three-section concrete labyrinth were taken during the summer of 1982 at the institute of High Energy Physics at Protvino, near Moscow, Russia. The neutron source used was ^{252}Cf . It was installed at the entrance of the labyrinth and was used in a bare configuration or at the center of a polyethylene sphere. The neutron flux was measured with Bonner spheres of different diameters that were placed at different locations in the labyrinth. The labyrinth configuration was also changed to determine the influence of different materials and air cavities on the neutron flux. The goal of the experiments was to obtain benchmark data for validation of dosimetry computer codes used for the design of the Large Serpoukhov Proton Accelerator. A benchmark was created and published in the ICSBEP Handbook in 2007 under the title “Neutron Fields in Three-section Concrete Labyrinth from Cf-252 Source” and was labeled as *ALARM-CF-AIR-LAB-001* [20].

2.3.1 Benchmark Model

The benchmark model represents an air path with concrete walls. The path changes direction twice, so it is known as a concrete labyrinth. The top and side views of the concrete building from the MAVRIC model are shown in Figure 19 and Figure 20, respectively, representing Cases 1A and 1B from *ALARM-CF-AIR-LAB-001* from screenshots of the SCALE/MAVRIC benchmark model. All the dimensions given are in unit of centimeter. A ^{252}Cf neutron source is placed at the entrance of the labyrinth, as indicated by a purple sphere in Figure 19. The benchmark values derived from the benchmark model are neutron count rates from different locations labeled 1–10 in Figure 19 and are measured by cadmium-covered Bonner sphere detectors of different diameters (2, 3, 5 in., 5 in. without cadmium cover, and 8, 10, and 12 in.). The ^{252}Cf source can be bare (Case XA) or covered by a 30.5 cm diameter polyethylene sphere with a 4 cm diameter spherical central cavity (Case XB). There are 6 different maze configurations, which increases the number of cases of the benchmark, as shown by Figure 21 for Case 2, Figure 22 for Cases 2 and 3, Figure 23 for Case 4, Figure 24 for Case 5, and Figure 25 for Case 6 (figures taken from the SCALE/MAVRIC benchmark models screenshots). This benchmark has been used for MAVRIC validation in the past [21]. The SCALE/MAVRIC calculations were performed using ENDF/B-VII.0 multi-group (200 neutron groups and 47 gamma groups) cross-section library.

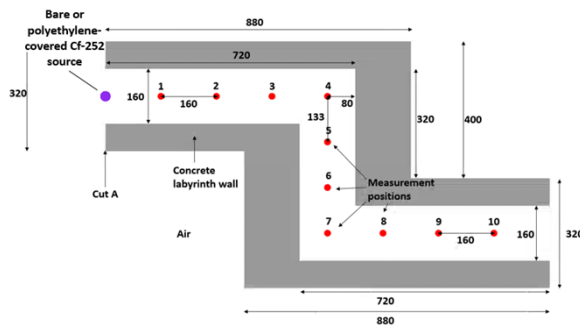


Figure 19. Horizontal section of the labyrinth, corresponding to Case 1.

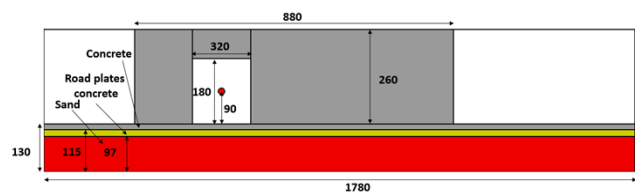


Figure 20. View of the labyrinth from the front at the Cut A.

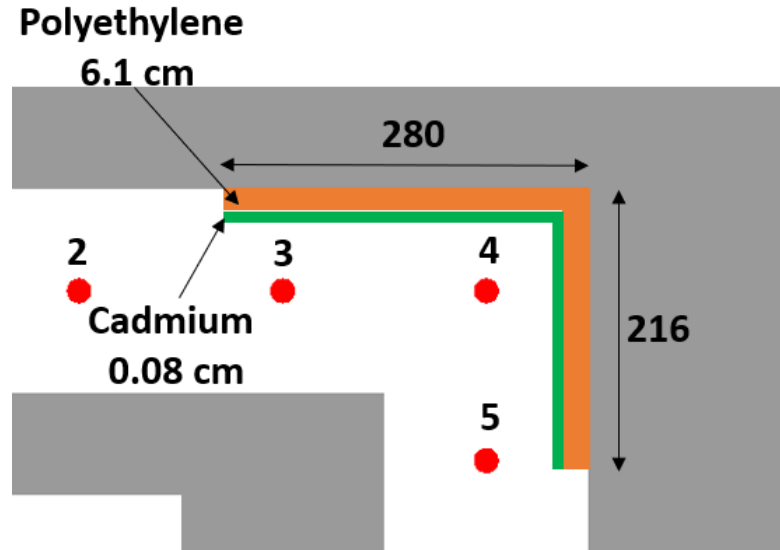


Figure 21. Case 2: polyethylene plates covered by 0.08 cm of cadmium, placed in the first corner of the labyrinth (see Figure 22). Case 3 differs from Case 2 only by the absence of the cadmium cover.

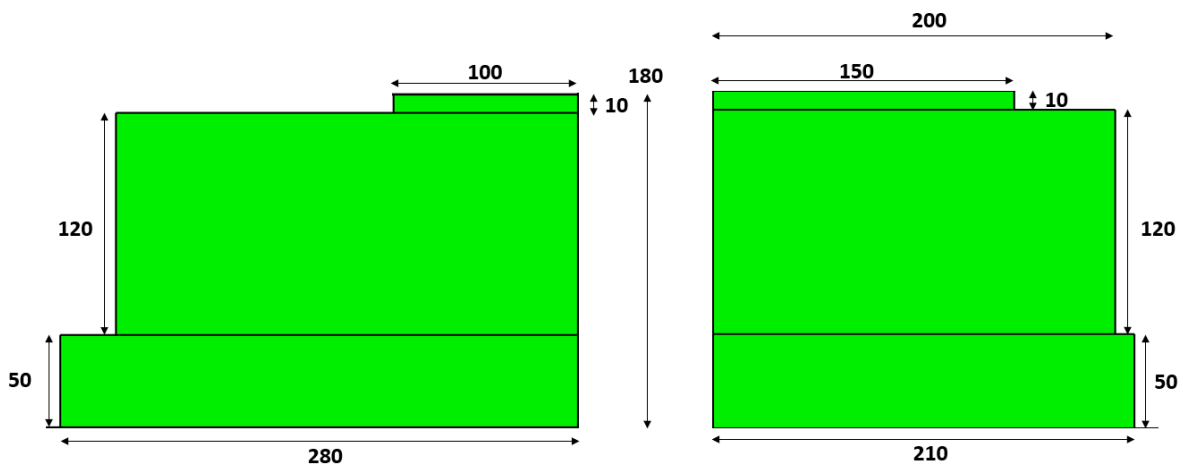


Figure 22. Cases 2 and 3, polyethylene plate dimensions in the first corner of the labyrinth.

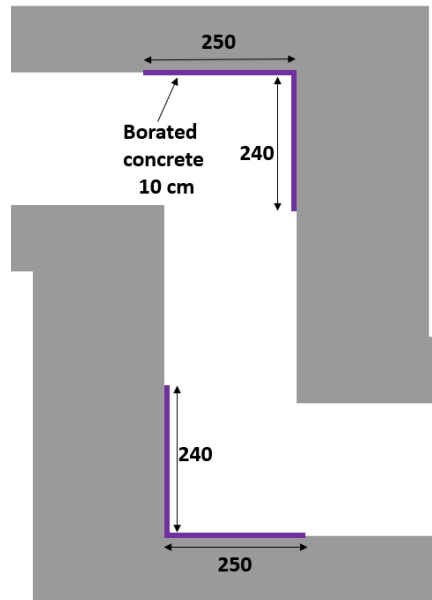


Figure 23. Case 4: borated concrete plates in the first and second corners of the labyrinth.

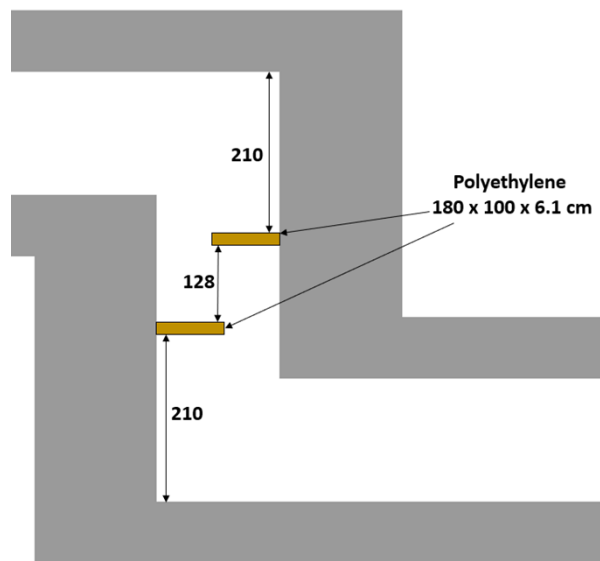


Figure 24. Case 5: polyethylene plates in the middle of the second straight section of the labyrinth.

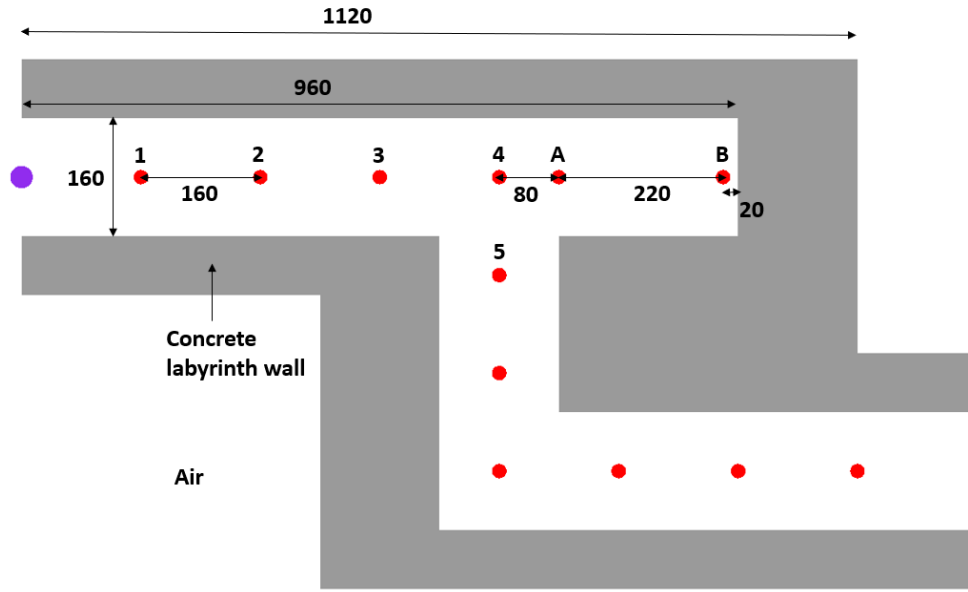


Figure 25. Case 6, dead end at the end of the first straight section of the labyrinth.

The different cases are summarized in Table 2.

Table 2. Summary of Concrete labyrinth configurations and Cases studied.

Labyrinth configuration	Cases	Characteristics
1	1A 1B	Regular labyrinth (Figure 19 and Figure 20)
2	2A 2B	Polyethylene and cadmium plates on first corner (Figure 21 and Figure 22)
3	3A 3B	Polyethylene plates on first corner (Figure 21 and Figure 22)
4	4A 4B	Borated concrete plates on first and second corners (Figure 23)
5	5A	Polyethylene plates on the second straight section (Figure 24)
6	6A 6B	Dead end added at the end of the first straight section (Figure 25)

During the actual experiments, the 10 measurements positions were not always used, resulting in an inconsistent number of measurements, depending on the case. The sample calculations from the ICSBEP report were performed with MCNP5 (ENDF/B-VI.2), all measurement positions were checked, and the calculations that were performed with MAVRIC for this work also checked all measurement positions. Ultimately, the number of points of comparison between SCALE/MAVRIC using ENDF/B-VII.0 cross-section library and the experiments vary, depending on the case. Note that there are no covered source measurements in labyrinth configuration 5 (no Case 5B). The comparison points are summarized in Table 3 and Table 4.

Table 3. Summary of experiment measurement points ordered by concrete labyrinth configuration.

Experiment measurements points											
Measurement position number	Case 1A	Case 1B	Case 2A	Case 2B	Case 3A	Case 3B	Case 4A	Case 4B	Case 5A	Case 6A	Case 6B
1	X	X					X				
2	X	X					X				
3	X	X					X				
4	X	X	X	X	X	X	X				X
5	X	X	X	X	X	X	X	X			X
6	X	X	X		X	X	X	X		X	X
7	X	X	X	X	X	X	X	X	X	X	X
8	X	X	X		X		X	X	X	X	X
9	X	X								X	
10	X	X									
A										X	X
B										X	X

Table 4. Summary of MAVRIC and MCNP benchmark calculation points ordered by concrete labyrinth configuration.

MAVRIC and MCNP benchmark measurement points											
Measurement position number	Case 1A	Case 1B	Case 2A	Case 2B	Case 3A	Case 3B	Case 4A	Case 4B	Case 5A	Case 6A	Case 6B
1	X	X	X	X	X	X	X	X	X	X	X
2	X	X	X	X	X	X	X	X	X	X	X
3	X	X	X	X	X	X	X	X	X	X	X
4	X	X	X	X	X	X	X	X	X	X	X
5	X	X	X	X	X	X	X	X		X	X
6	X	X	X	X	X	X	X	X		X	X
7	X	X	X	X	X	X	X	X	X	X	X
8	X	X	X	X	X	X	X	X	X	X	X
9	X	X	X	X	X	X	X	X	X	X	X
10	X	X	X	X	X	X	X	X	X	X	X
A										X	X
B										X	X

2.3.2 Benchmark Results

2.3.2.1 Detector response function

For the first step of the benchmark modeling, the Bonner spheres detector response functions were obtained through MAVRIC simulations. One calculation was performed for each of the 200 neutron energy groups selected, for each of the 7 Bonner sphere detectors (2, 3, 5 in., 5 in. without cadmium

cover, and 8, 10, and 12 in.), resulting in 1,400 calculations run. The results obtained with MAVRIC compared to the MCNP results from the benchmark report for the 7 Bonner sphere detectors are shown in the following figures: Figure 26 for 2 in., Figure 27 for 3 in., Figure 28 for 5 in., Figure 29 for 5 in. without cadmium cover, Figure 30 for 8 in., Figure 31 for 10 in., and Figure 32 for 12 in. Overall, the MAVRIC and MCNP results agree well. The MAVRIC results are slightly higher than those of MCNP on the 2 and 3 in. Bonner spheres and slightly lower in the other diameters. Also, the use of 200 energy groups allows for a much more precise detector response function than obtained in the MCNP results. The uncertainties were all too low to be displayed graphically.

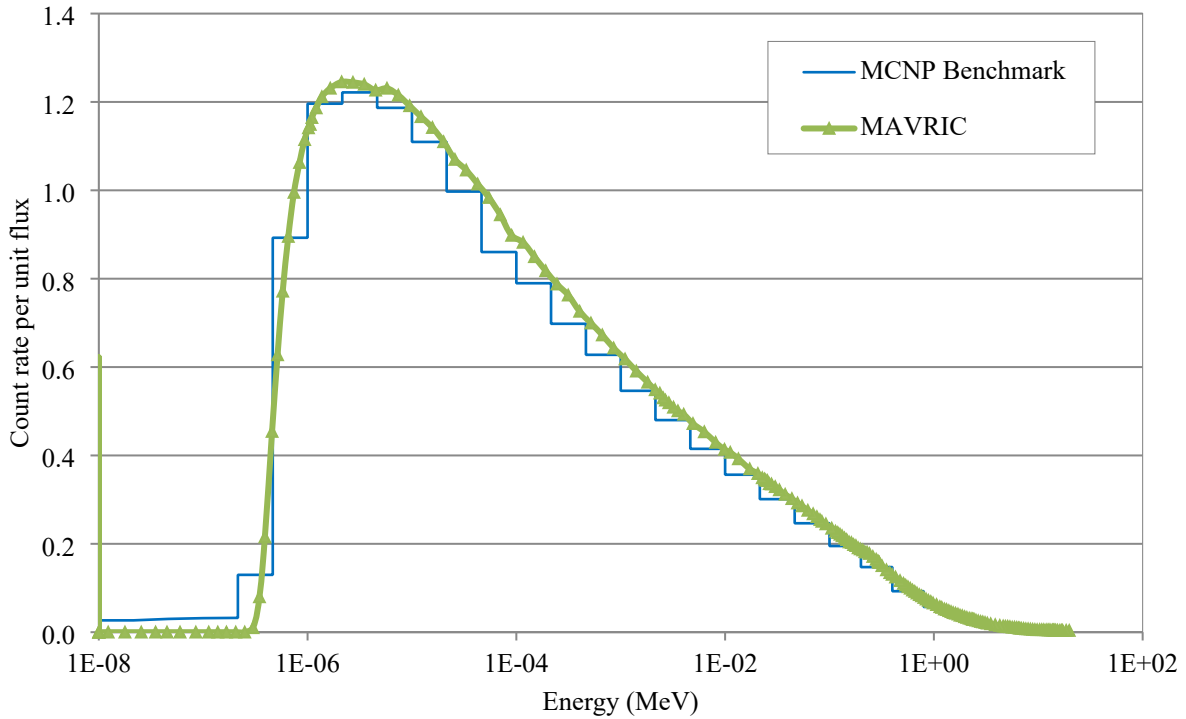


Figure 26. 2 in. Bonner sphere detector response function.

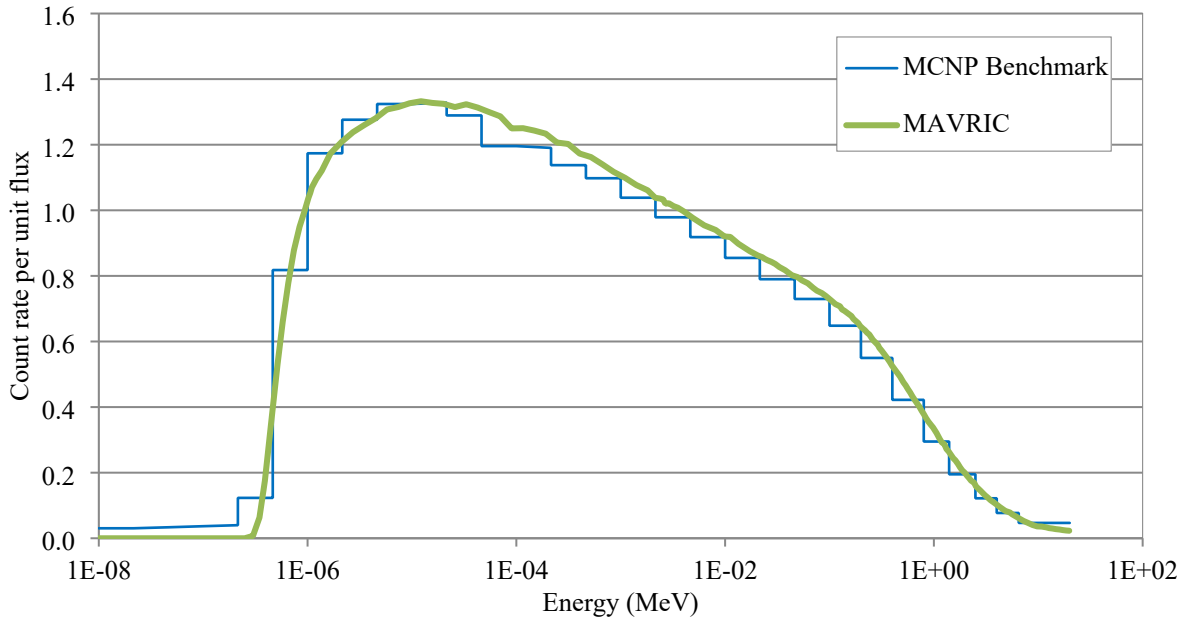


Figure 27.3 in. Bonner sphere detector response function.

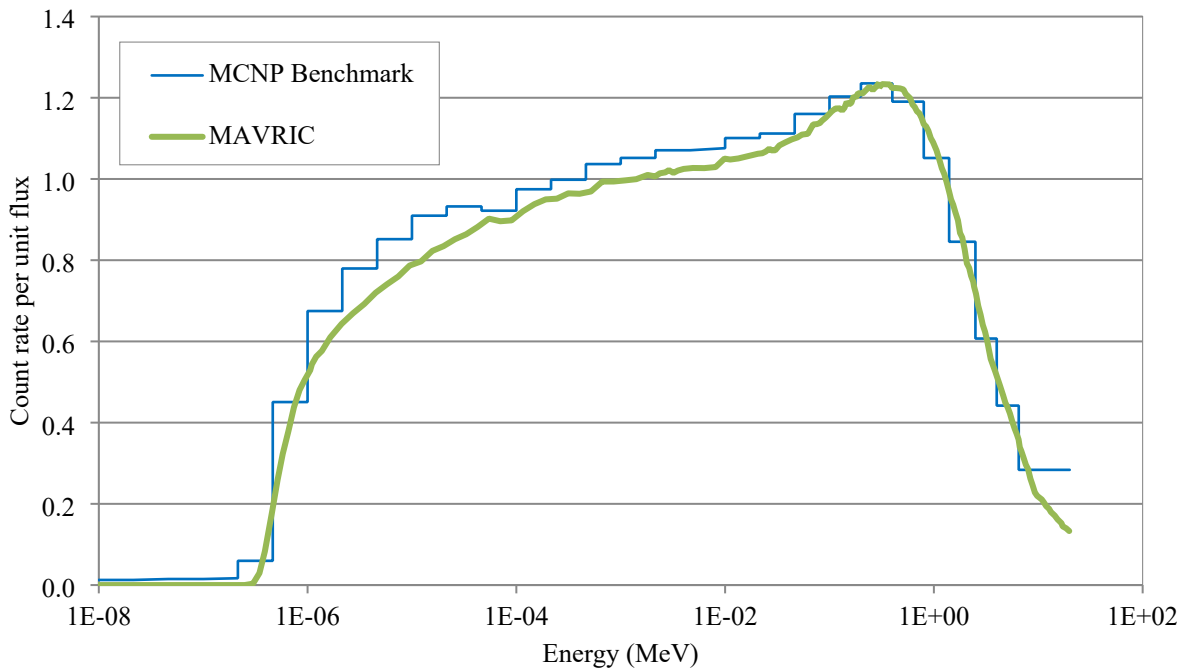


Figure 28.5 in. Bonner sphere detector response function.

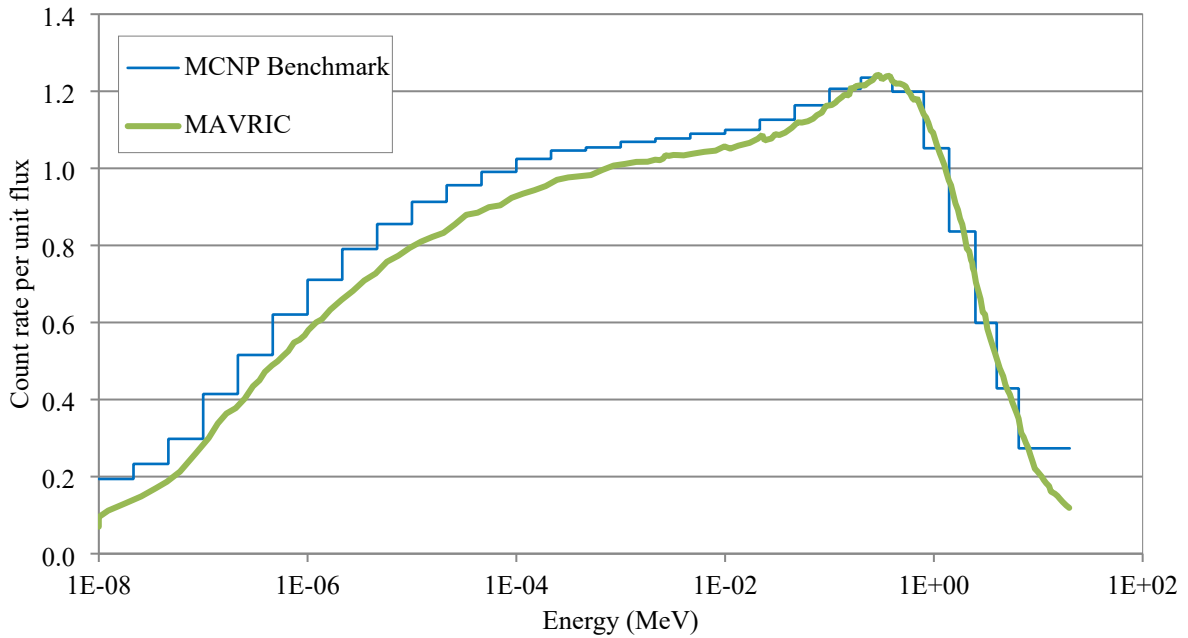


Figure 29. 5 in. Bonner sphere detector response function without Cd layer.

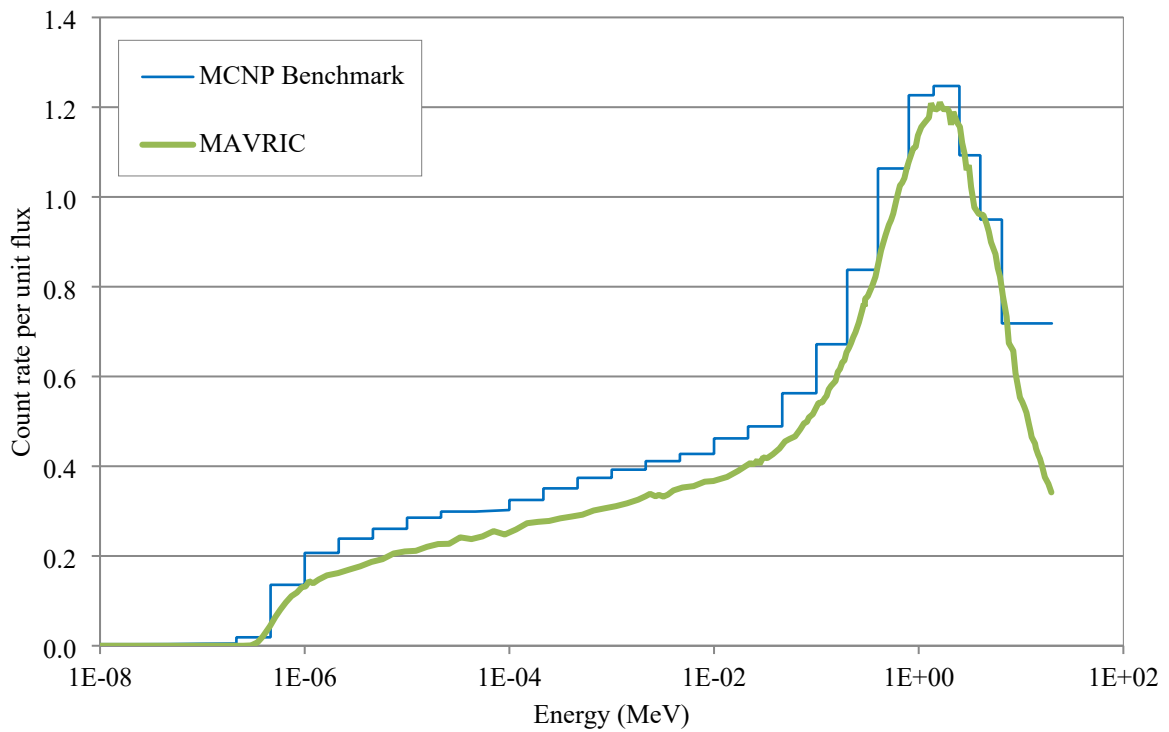


Figure 30. 8 in. Bonner sphere detector response function.

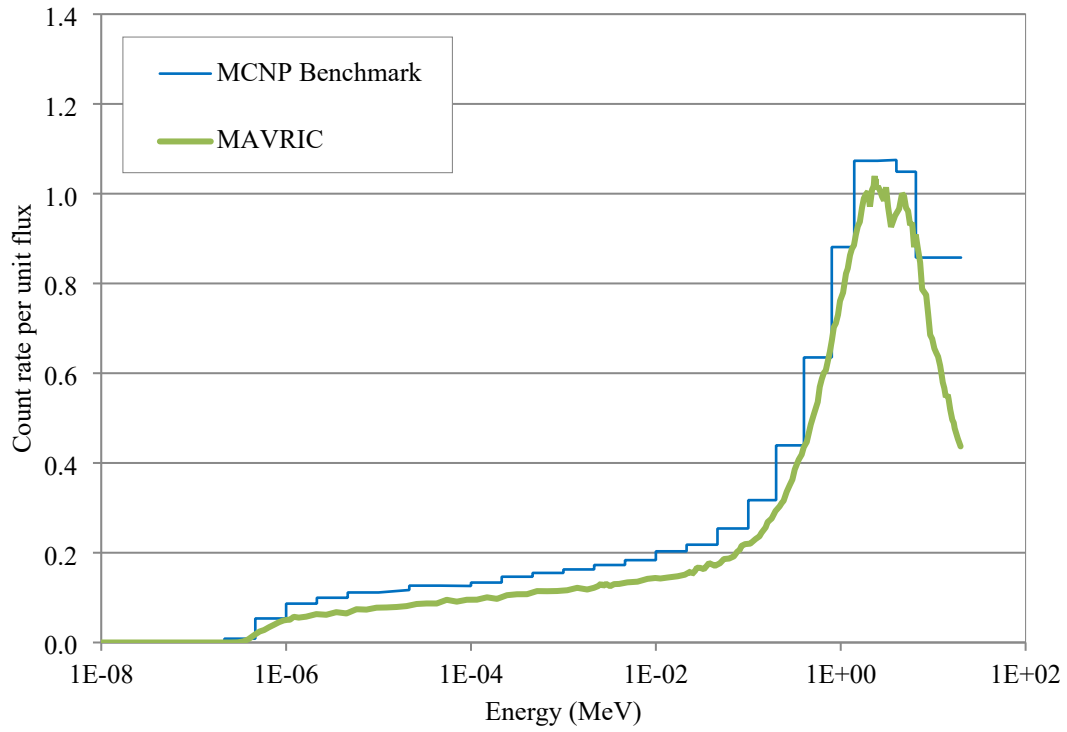


Figure 31. 10 in. Bonner sphere detector response function.

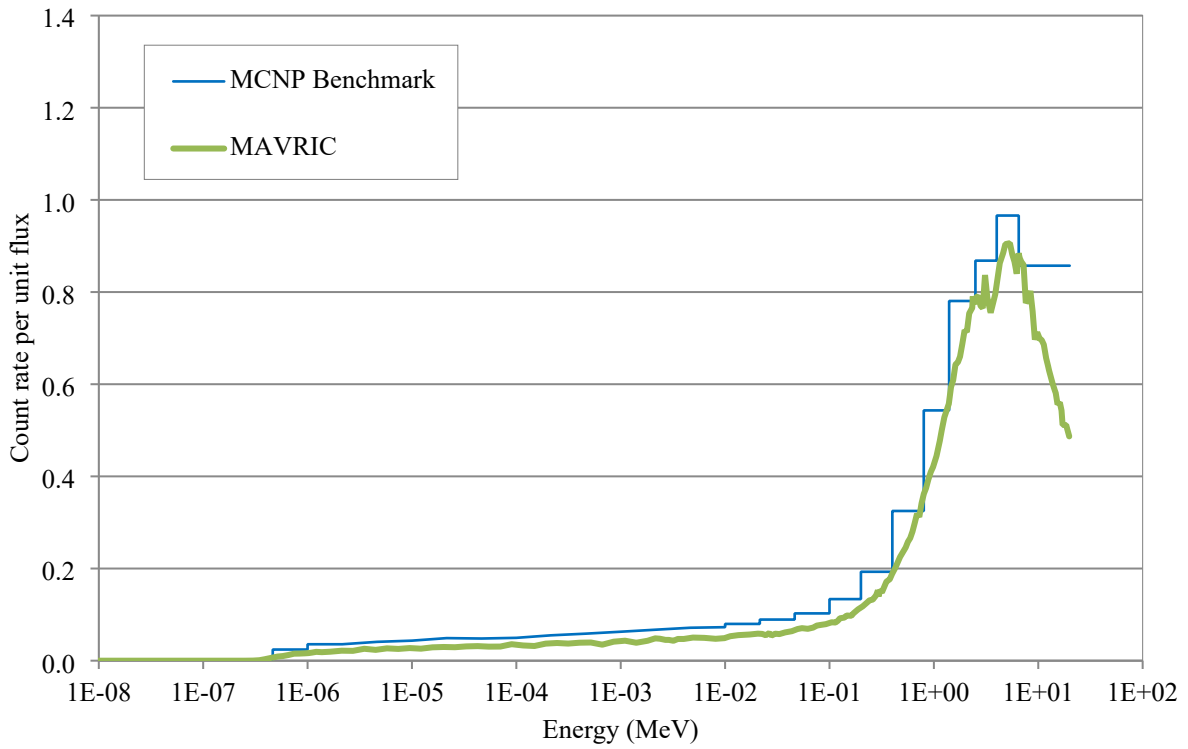


Figure 32. 12 in. Bonner sphere detector response function.

2.3.2.2 MAVRIC detector counts

The detector count rates obtained with MAVRIC for each labyrinth configuration, Bonner sphere detector, and source type are shown in Table 5 for Case 1A, Table 6 for Case 1B, Table 7 for Case 2A, Table 8 for Case 2B, Table 9 for Case 3A,

Table 10 for Case 3B, Table 11 for Case 4A, Table 12 for Case 4B,

Table 13 for Case 5A, Table 14 for Case 6A, and Table 15 for Case 6B. The calculation relative uncertainties for the detector count rates were all below 5%.

Table 5. MAVRIC calculation results (pulses per second) for Case 1A.

Measurement position number	Bonner sphere						
	2 in.	3 in.	5 in.	5 in. no Cd	8 in.	10 in.	12 in.
1	1,814.05	3,609.38	5,821.53	6,272.27	4,519.72	3,033.63	1,907.87
2	783.86	1,447.83	2,092.01	2,349.35	1,502.45	964.05	589.29
3	359.60	640.63	905.60	1,061.24	649.52	416.94	254.00
4	195.27	352.75	501.97	595.22	362.40	234.24	144.56
5	90.66	146.47	167.60	218.46	90.07	48.67	25.73
6	33.58	51.71	54.42	79.66	26.36	13.63	6.73
7	16.12	24.28	24.60	38.21	11.48	5.90	2.90
8	5.02	7.14	6.49	12.74	2.64	1.19	0.53
9	1.49	2.06	1.80	4.30	0.70	0.31	0.13
10	0.57	0.78	0.67	1.78	0.26	0.11	0.05

Table 6. MAVRIC calculation results (pulses per second) for Case 1B.

measurement position number	Bonner sphere						
	2 in.	3 in.	5 in.	5 in. no Cd	8 in.	10 in.	12 in.
1	455.89	757.12	970.95	1,280.89	658.04	427.06	268.24
2	174.01	281.91	346.73	487.93	215.74	135.42	82.30
3	76.41	123.81	149.03	216.31	92.40	58.50	34.93
4	41.80	66.18	80.79	118.09	51.95	33.12	19.85
5	16.24	24.58	25.97	44.96	12.84	6.81	3.61
6	5.79	8.37	8.13	17.05	3.78	1.91	0.94
7	2.63	3.85	3.63	8.33	1.64	0.82	0.41
8	0.76	1.07	0.95	2.93	0.38	0.17	0.07
9	0.23	0.30	0.26	1.05	0.10	0.04	0.02
10	0.08	0.11	0.10	0.44	0.03	0.02	0.01

Table 7. MAVRIC calculation results (pulses per second) for Case 2A.

Measurement position number	Bonner sphere						
	2 in.	3 in.	5 in.	5 in. no Cd	8 in.	10 in.	12 in.
1	1,799.00	3,632.41	5,823.92	6,237.47	4,527.48	3,059.53	1,913.94
2	789.79	1,459.37	2,101.46	2,372.19	1,496.44	971.61	588.10
3	343.85	636.75	926.65	1,051.81	658.22	420.87	254.67
4	169.12	336.89	539.22	565.49	395.08	248.89	148.79
5	78.55	141.83	182.01	201.34	100.56	53.52	26.54
6	31.12	51.38	58.82	70.11	29.03	14.51	6.76
7	15.49	24.53	26.97	32.68	12.83	6.32	2.82

8	5.30	7.84	7.43	10.68	3.02	1.35	0.56
9	1.62	2.35	2.10	3.49	0.80	0.35	0.14
10	0.62	0.89	0.78	1.40	0.30	0.13	0.05

Table 8. MAVRIC calculation results (pulses per second) for Case 2B.

Measurement position number	Bonner sphere						
	2 in.	3 in.	5 in.	5 in. no Cd	8 in.	10 in.	12 in.
1	445.12	760.63	980.67	1,273.75	656.41	427.25	266.33
2	177.58	285.70	342.71	484.31	219.84	135.93	82.74
3	74.50	123.21	153.10	206.12	94.97	59.03	36.09
4	37.49	66.57	87.20	105.52	57.36	35.80	20.80
5	14.28	23.98	28.10	34.80	14.63	7.50	3.70
6	5.33	8.48	8.71	11.70	4.18	2.04	0.95
7	2.51	3.95	4.06	5.67	1.83	0.88	0.39
8	0.84	1.20	1.12	1.87	0.43	0.19	0.08
9	0.25	0.35	0.30	0.61	0.11	0.05	0.02
10	0.10	0.13	0.11	0.25	0.04	0.02	0.01

Table 9. MAVRIC calculation results (pulses per second) for Case 3A.

Measurement position number	Bonner sphere						
	2 in.	3 in.	5 in.	5 in. no Cd	8 in.	10 in.	12 in.
1	1,815.25	3,613.59	5,765.65	6,243.68	4,526.98	3,034.93	1,895.78
2	774.00	1,419.82	2,057.08	2,354.71	1,491.01	958.94	584.31
3	328.12	601.78	840.81	1,005.21	611.28	394.14	244.31
4	153.02	271.04	387.15	491.73	291.48	195.90	123.73
5	63.95	99.22	105.97	160.35	54.21	29.89	15.55
6	21.45	32.09	31.64	56.35	14.64	7.49	3.68
7	9.74	14.25	13.48	27.04	6.01	3.04	1.48
8	2.97	4.09	3.65	9.43	1.43	0.65	0.28
9	0.87	1.16	0.99	3.29	0.37	0.16	0.07
10	0.32	0.43	0.36	1.37	0.14	0.06	0.02

Table 10. MAVRIC calculation results (pulses per second) for Case 3B.

Measurement position number	Bonner sphere						
	2 in.	3 in.	5 in.	5 in. no Cd	8 in.	10 in.	12 in.
1	450.66	755.88	977.91	1,282.08	659.76	424.03	266.50
2	172.61	282.61	338.68	472.81	212.94	133.55	80.73
3	72.06	115.02	138.33	207.76	87.50	54.37	33.68
4	33.29	51.85	63.76	105.43	42.69	27.35	17.07
5	11.06	16.66	16.10	38.03	7.93	4.27	2.19
6	3.72	5.12	4.83	13.99	2.16	1.09	0.53
7	1.67	2.37	1.98	6.98	0.92	0.44	0.21
8	0.46	0.62	0.53	2.54	0.21	0.09	0.04
9	0.14	0.17	0.14	0.93	0.05	0.02	0.01
10	0.05	0.07	0.05	0.39	0.02	0.01	0.00

Table 11. MAVRIC calculation results (pulses per second) for Case 4A.

Measurement position number	Bonner sphere						
	2 in.	3 in.	5 in.	5 in. no Cd	8 in.	10 in.	12 in.
1	1,825.34	3,606.59	5,824.99	6,261.21	4,522.74	3,034.35	1,912.69
2	780.37	1,444.49	2,096.07	2,333.36	1493.09	956.84	591.55
3	343.57	631.90	895.62	1,005.13	637.41	408.97	254.56
4	165.33	311.78	461.04	496.63	338.40	222.17	139.94
5	72.84	120.83	140.61	159.67	76.30	42.02	22.21
6	24.18	38.59	41.66	48.27	20.36	10.71	5.34
7	10.50	16.44	17.08	19.58	8.26	4.27	2.14
8	3.10	4.60	4.26	5.25	1.79	0.83	0.37
9	0.91	1.27	1.14	1.56	0.44	0.20	0.08
10	0.34	0.48	0.42	0.61	0.16	0.07	0.03

Table 12. MAVRIC calculation results (pulses per second) for Case 4B.

Measurement position number	Bonner sphere						
	2 in.	3 in.	5 in.	5 in. no Cd	8 in.	10 in.	12 in.
1	447.06	758.46	971.23	1,282.20	658.15	422.58	264.08
2	173.37	284.11	342.93	474.79	215.39	133.90	82.01
3	73.19	119.92	146.82	200.63	91.31	57.63	35.05
4	34.77	61.22	73.59	92.70	47.78	31.04	19.45
5	12.68	20.13	21.82	28.57	10.71	5.90	3.10
6	4.22	6.11	6.21	8.28	2.90	1.45	0.76
7	1.78	2.65	2.59	3.29	1.17	0.60	0.30
8	0.48	0.68	0.63	0.87	0.25	0.12	0.05
9	0.14	0.19	0.16	0.27	0.06	0.03	0.01
10	0.05	0.07	0.06	0.10	0.02	0.01	0.00

Table 13. MAVRIC calculation results (pulses per second) for Case 5A.

Measurement position number	Bonner sphere						
	2 in.	3 in.	5 in.	5 in. no Cd	8 in.	10 in.	12 in.
1	1,833.77	3,633.53	5,803.70	6,273.80	4,528.82	3,032.06	1,918.40
2	783.90	1,443.27	2,093.30	2,359.38	1,498.18	959.52	592.56
3	359.38	646.93	913.12	1,056.73	641.17	415.28	254.30
4	197.50	357.40	505.33	598.84	360.90	236.77	143.48
5	N/A	N/A	N/A	N/A	N/A	N/A	N/A
6	N/A	N/A	N/A	N/A	N/A	N/A	N/A
7	1.91	2.86	2.92	6.20	1.52	0.83	0.45
8	0.94	1.36	1.31	2.98	0.59	0.29	0.14
9	0.26	0.36	0.33	0.95	0.14	0.06	0.03
10	0.09	0.13	0.12	0.39	0.05	0.02	0.01

Table 14. MAVRIC calculation results (pulses per second) for Case 6A.

Measurement position number	Bonner sphere						
	2 in.	3 in.	5 in.	5 in. no Cd	8 in.	10 in.	12 in.
1	1,841.00	3,611.91	5,787.85	6,284.80	4,542.52	3,036.27	1,907.42
2	781.92	1,434.07	2,072.13	2,339.25	1,480.06	959.71	581.25
3	341.05	622.76	886.86	1,024.54	625.20	410.68	253.47
4	156.90	284.69	418.78	488.67	309.75	206.51	130.46
5	71.61	113.38	129.56	169.57	70.29	38.46	20.08
6	25.71	39.39	41.58	60.77	20.38	10.50	5.17
7	12.30	18.42	18.49	29.59	8.77	4.43	2.20
8	3.85	5.48	5.02	9.85	2.03	0.95	0.41
9	1.14	1.57	1.37	3.32	0.53	0.24	0.10
10	0.43	0.61	0.51	1.37	0.20	0.08	0.04
A	115.19	214.34	315.31	371.18	235.04	155.30	98.97
B	94.05	172.18	243.21	287.68	175.70	112.06	70.78

Table 15. MAVRIC calculation results (pulses per second) for Case 6B.

Measurement position number	Bonner sphere						
	2 in.	3 in.	5 in.	5 in. no Cd	8 in.	10 in.	12 in.
1	445.11	751.92	975.43	1,263.99	656.62	428.36	266.38
2	173.48	282.07	342.87	487.71	217.51	135.00	81.70
3	74.18	122.23	142.51	213.66	91.23	58.56	34.63
4	34.15	55.77	68.96	104.04	45.89	29.63	17.62
5	12.77	19.26	20.05	35.42	10.16	5.47	2.86
6	4.40	6.51	6.22	13.11	2.91	1.50	0.73
7	2.08	2.87	2.80	6.43	1.25	0.63	0.30
8	0.60	0.83	0.74	2.29	0.29	0.13	0.06
9	0.18	0.23	0.20	0.81	0.08	0.03	0.01
10	0.07	0.09	0.07	0.34	0.03	0.01	0.01
A	26.50	41.88	52.60	76.37	34.52	22.33	13.36
B	19.36	31.45	39.57	57.68	25.20	16.29	9.37

2.3.2.3 Comparison to Experiment results

The ratios of the MAVRIC calculation results to the experiment results are shown in Figure 33 for Case 1A, Figure 34 for Case 1B, Figure 35 for Case 2A, Figure 36 for Case 2B, Figure 37 for Case 3A, Figure 38 for Case 3B, Figure 39 for Case 4A, Figure 40 for Case 4B, Figure 41 for Case 5A, Figure 42 for Case 6A, and Figure 43 for Case 6B. These figures provide comparisons for the different labyrinth and source configurations, measurement positions, and the 7 Bonner spheres. Overall, considering that the experimental relative uncertainties are between 5 and 30%, the MAVRIC calculations agree well with the experiment results, mostly within 30% and with a few outliers at a maximum of 70% off. The measurement location 10 calculation result differs the most from the experiment results. This is because location 10 is the farthest away from the source, so the count rates are very low, and the ratio is relatively high. Compared to the benchmark report, the MAVRIC results are overall slightly closer to the experiment results than the MCNP results. As described in the ICSBEP evaluation, the experiment results for Case 5A measurement position 8 is erroneous as it seems to be the same result as for the detector placed in the 7th position, so they have been removed from the comparison. The calculation uncertainties were all too low to be displayed graphically.

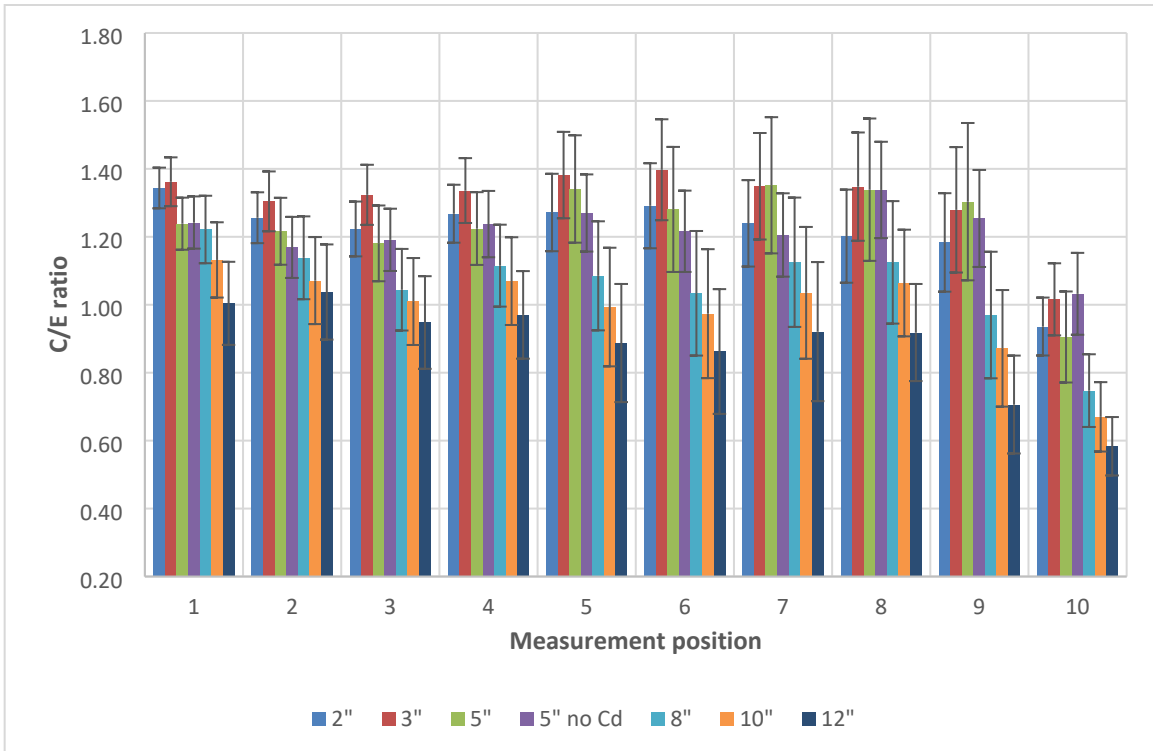


Figure 33. Case 1A C/E calculation results ratio for the different measurement positions and all Bonner spheres.

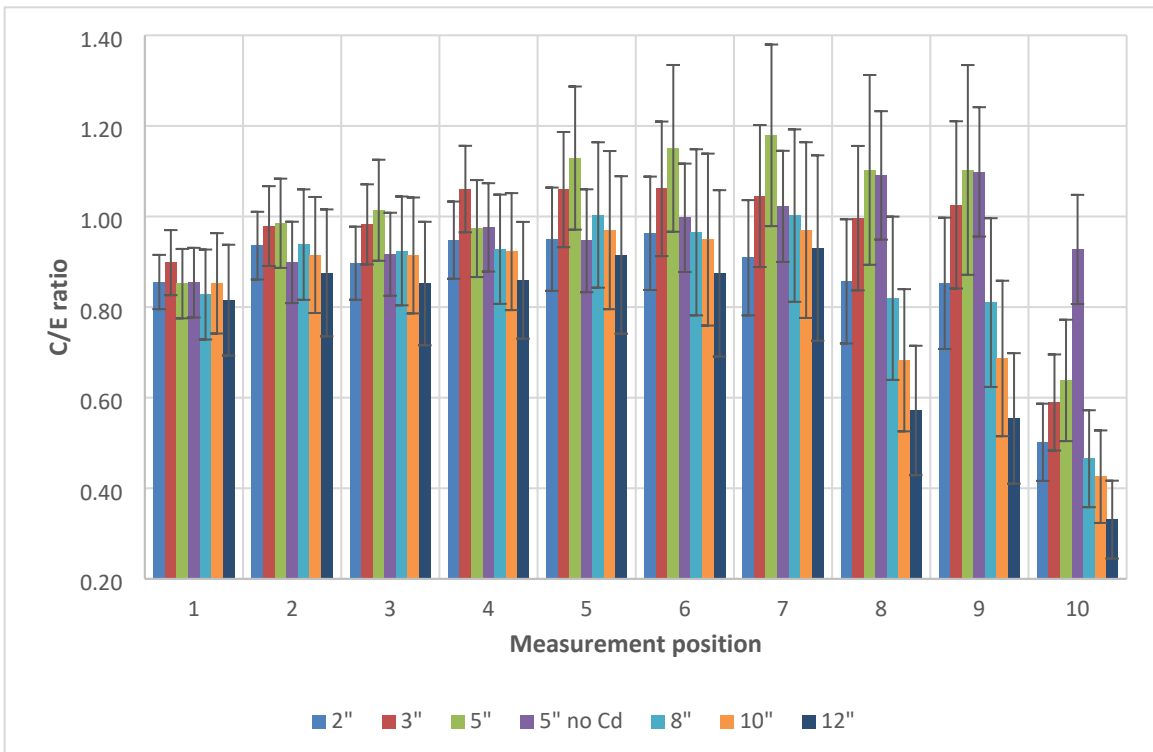


Figure 34. Case 1B C/E calculation results ratio for the different measurement positions and all Bonner spheres.

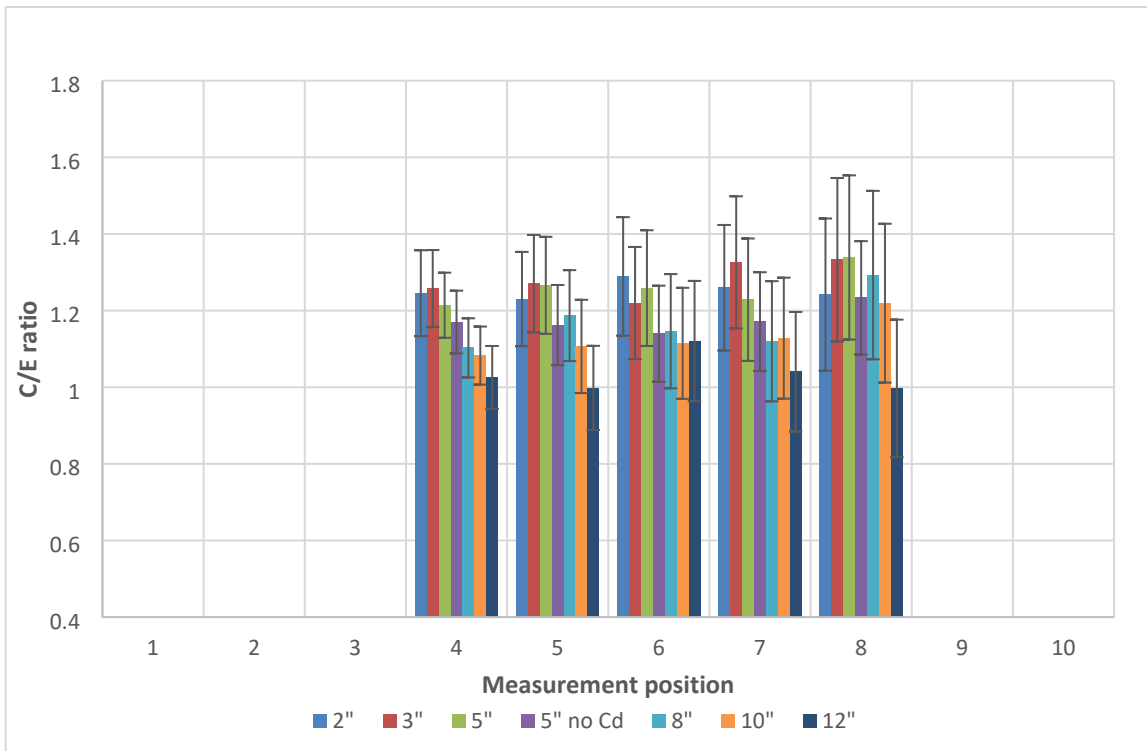


Figure 35. Case 2A C/E calculation results ratio for the different measurement positions and all Bonner spheres.

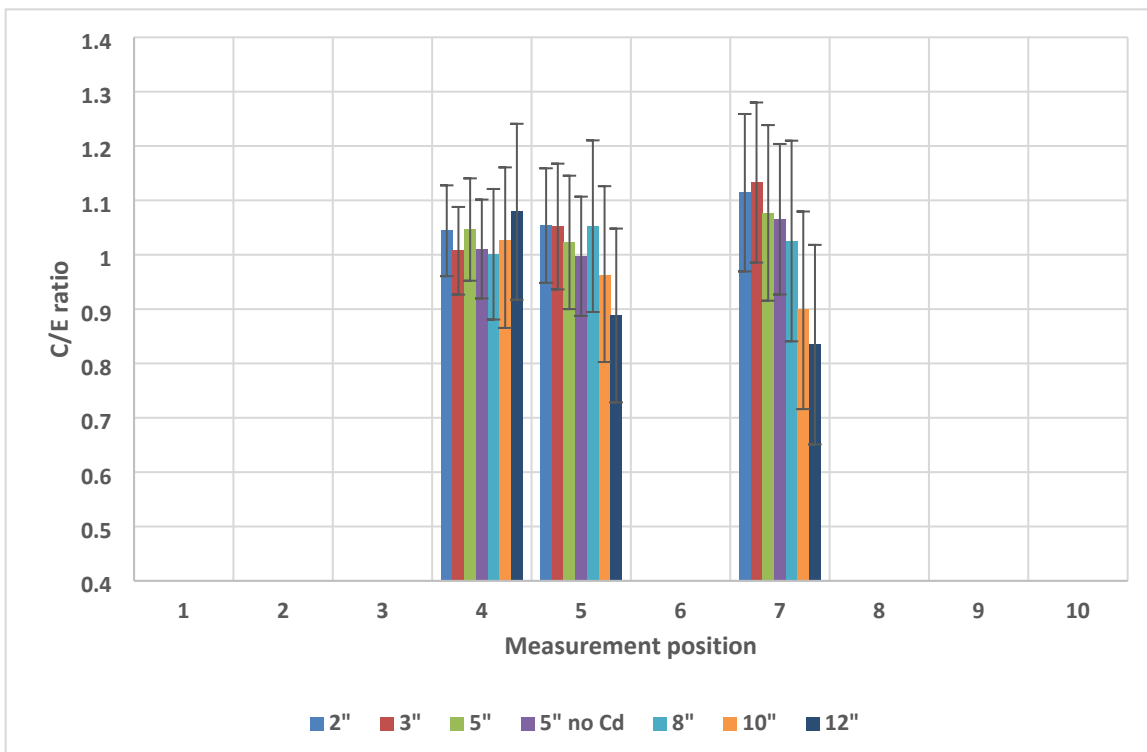


Figure 36. Case 2B C/E calculation results ratio for the different measurement positions and all Bonner spheres.

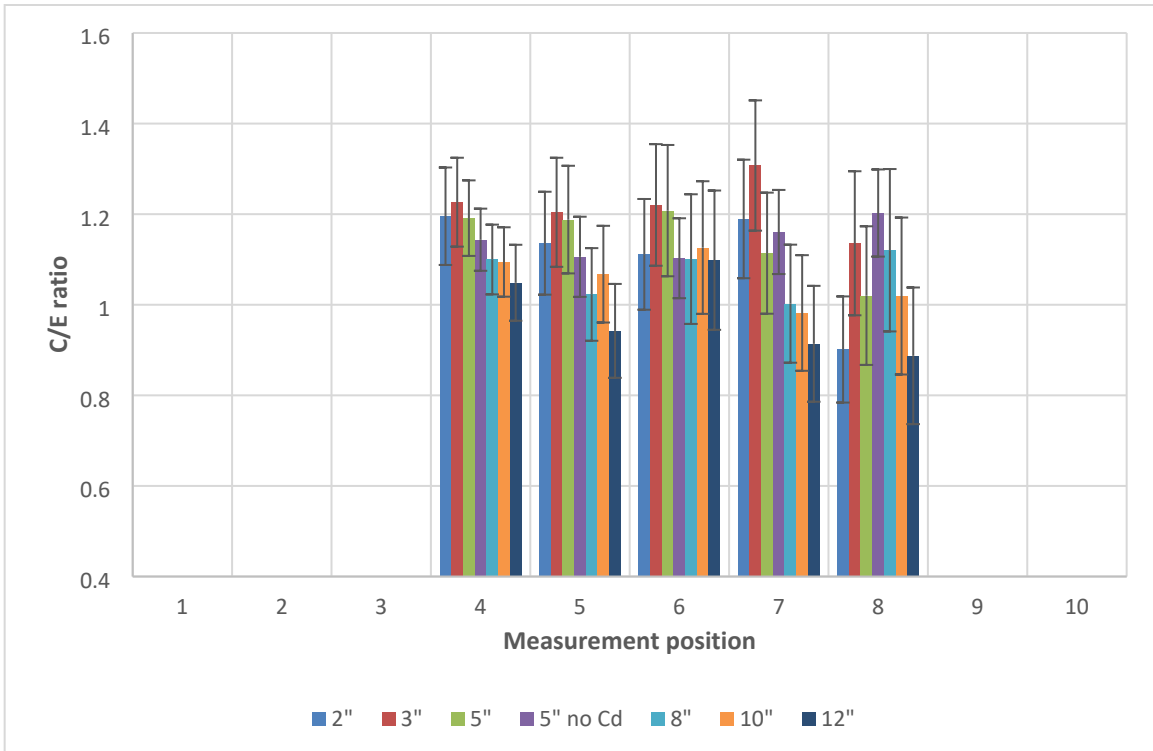


Figure 37. Case 3A C/E calculation results ratio for the different measurement positions and all Bonner spheres.

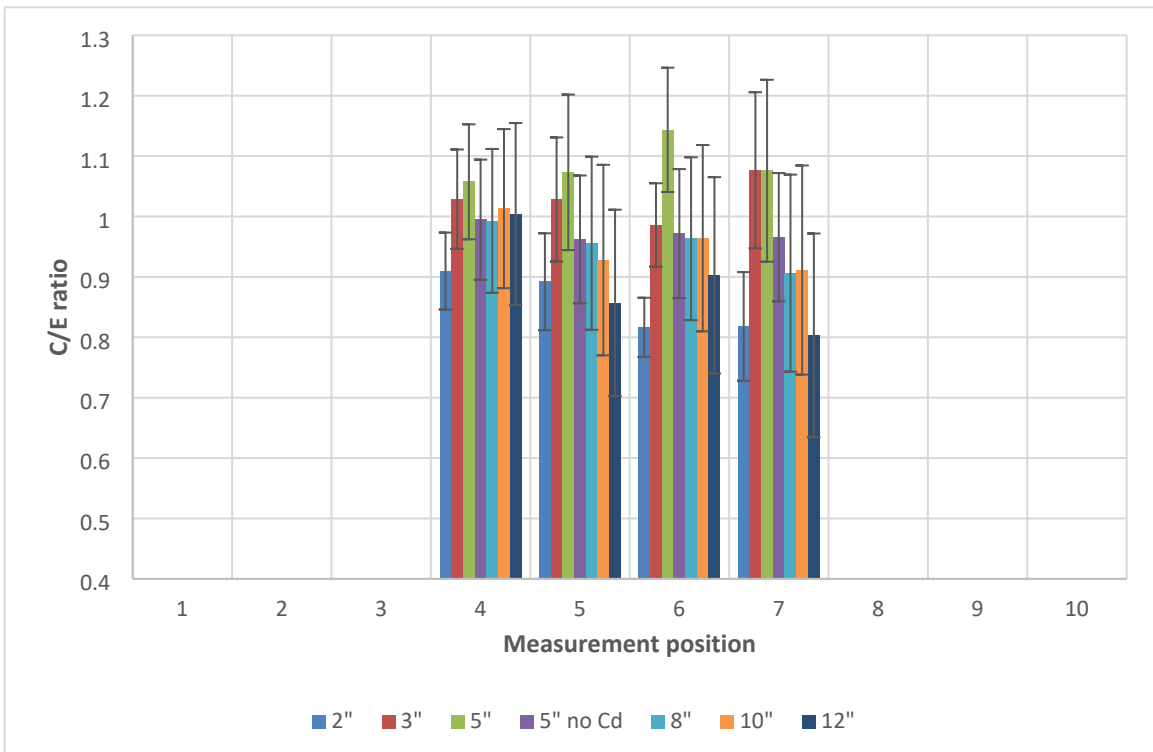


Figure 38. Case 3B C/E calculation results ratio for the different measurement positions and all Bonner spheres.

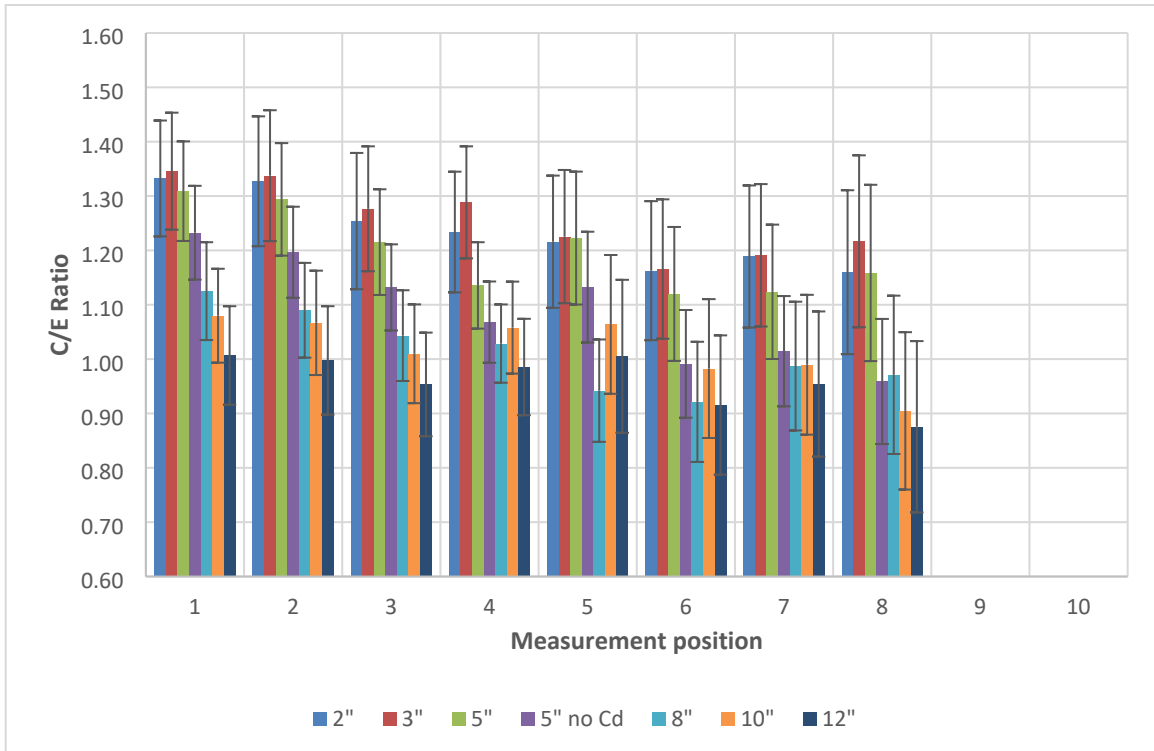


Figure 39. Case 4A C/E calculation results ratio for the different measurement positions and all Bonner spheres.

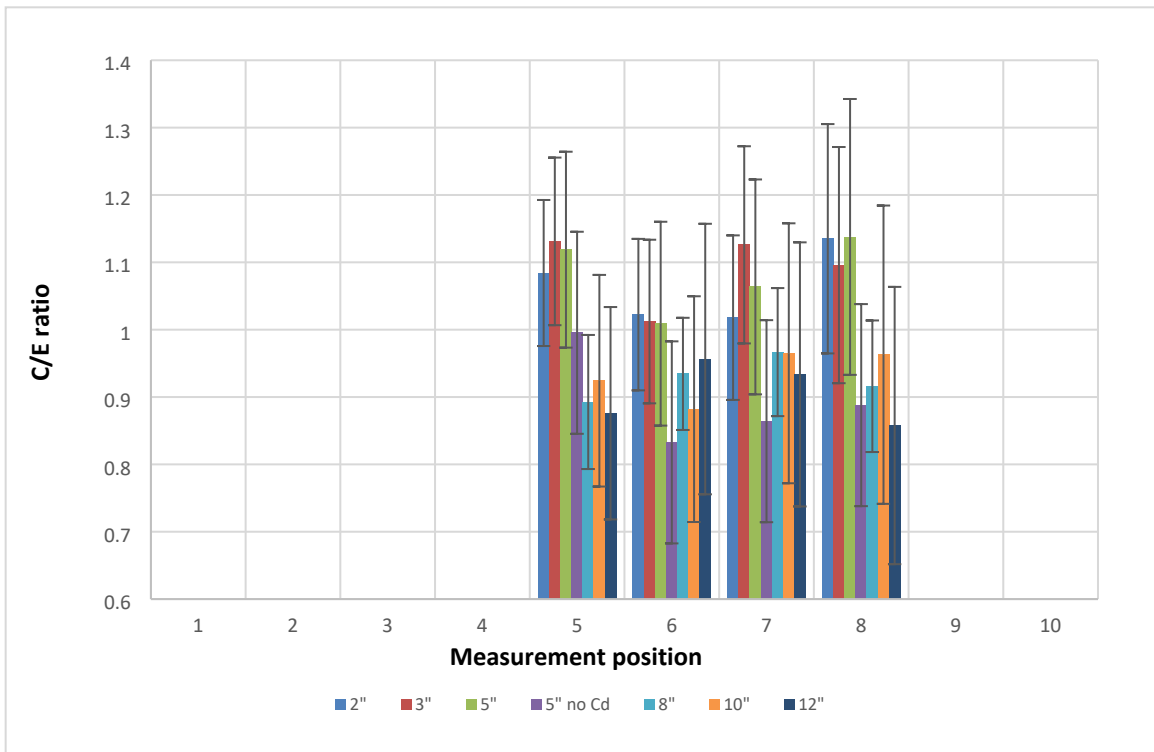


Figure 40. Case 4B C/E calculation results ratio for the different measurement positions and all Bonner spheres.

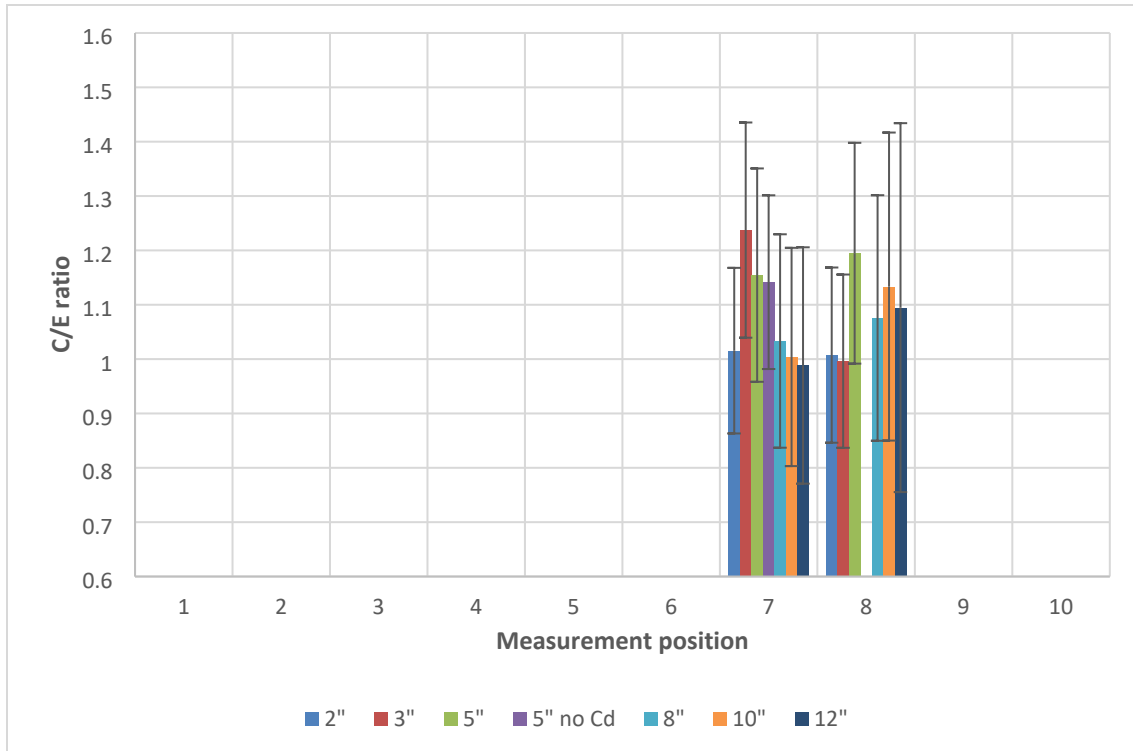


Figure 41. Case 5A C/E calculation results ratio for the different measurement positions and all Bonner spheres.

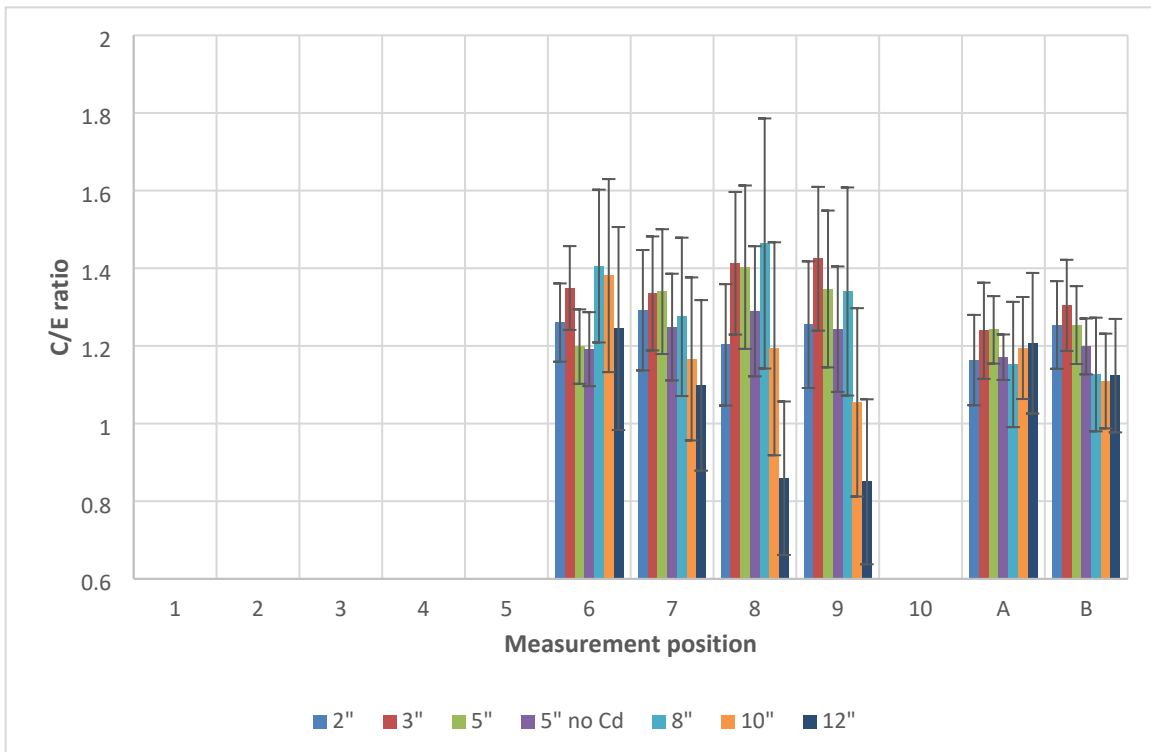


Figure 42. Case 6A C/E calculation results ratio for the different measurement positions and all Bonner spheres.

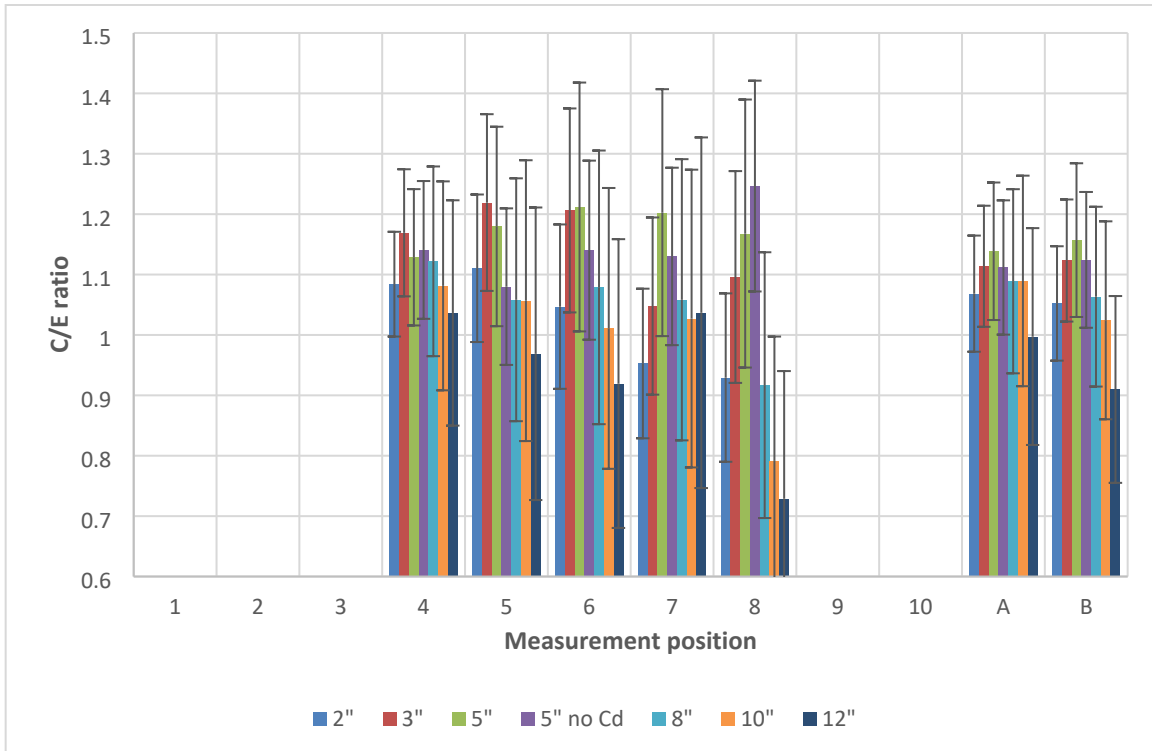


Figure 43. Case 6B C/E calculation results ratio for the different measurement positions and all Bonner spheres.

2.3.2.4 Comparison to Benchmark MCNP sample calculation results

The ratio of the MAVRIC calculation results to the MCNP calculation results is shown in Figure 44 for Case 1A, Figure 45 for Case 1B, Figure 46 for Case 2A, Figure 47 for Case 2B, Figure 48 for case 3A, Figure 49 for Case 3B, Figure 50 for Case 4A, Figure 51 for Case 4B, Figure 52 for Case 5A, Figure 53 for Case 6A, and Figure 54 for Case 6B. These figures provide comparisons for the different labyrinth and source configurations, measurement positions, and the 7 Bonner spheres. Overall, MAVRIC and MCNP agree within 40%. The difference between MCNP and MAVRIC results might be due to the different cross-section libraries used, ENDF/B-VI.2 continuous energy for MCNP5 and ENDF/B-VII.0 multi-group (200n47g) for SCALE/MAVRIC 6.2.4. The uncertainties were all too low to be displayed graphically.

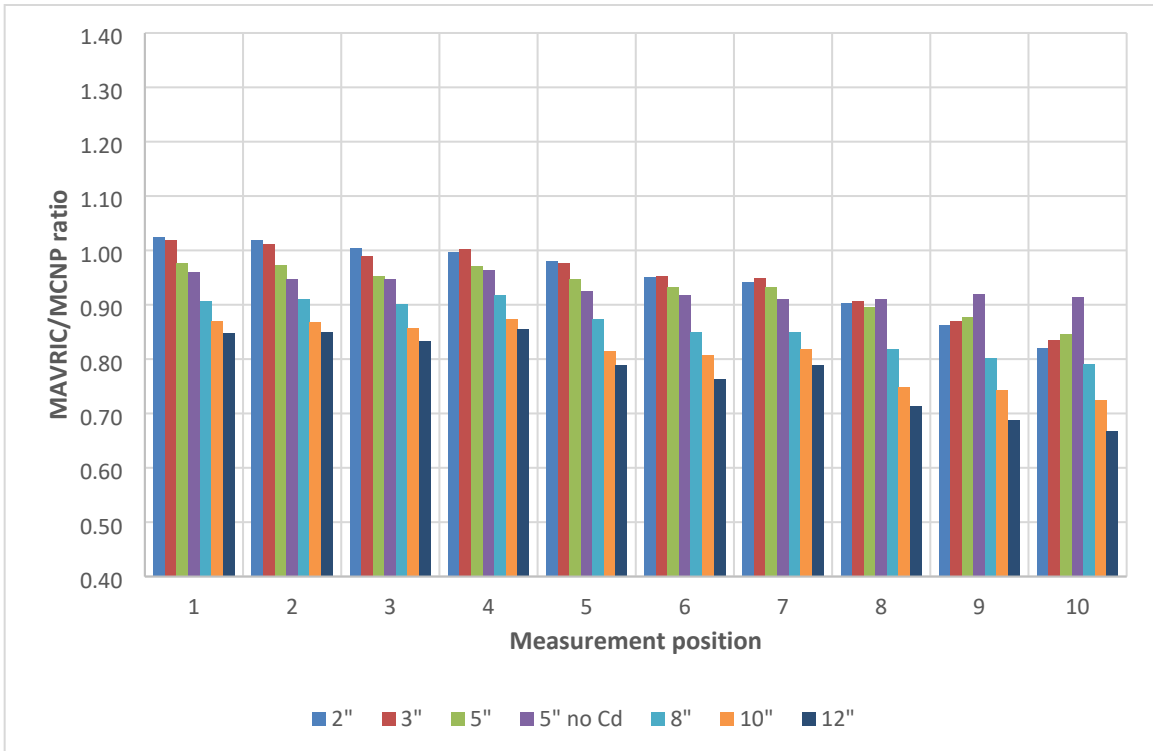


Figure 44. Case 1A MAVRIC/MCNP calculation results ratio for the different measurement positions and all Bonner spheres.

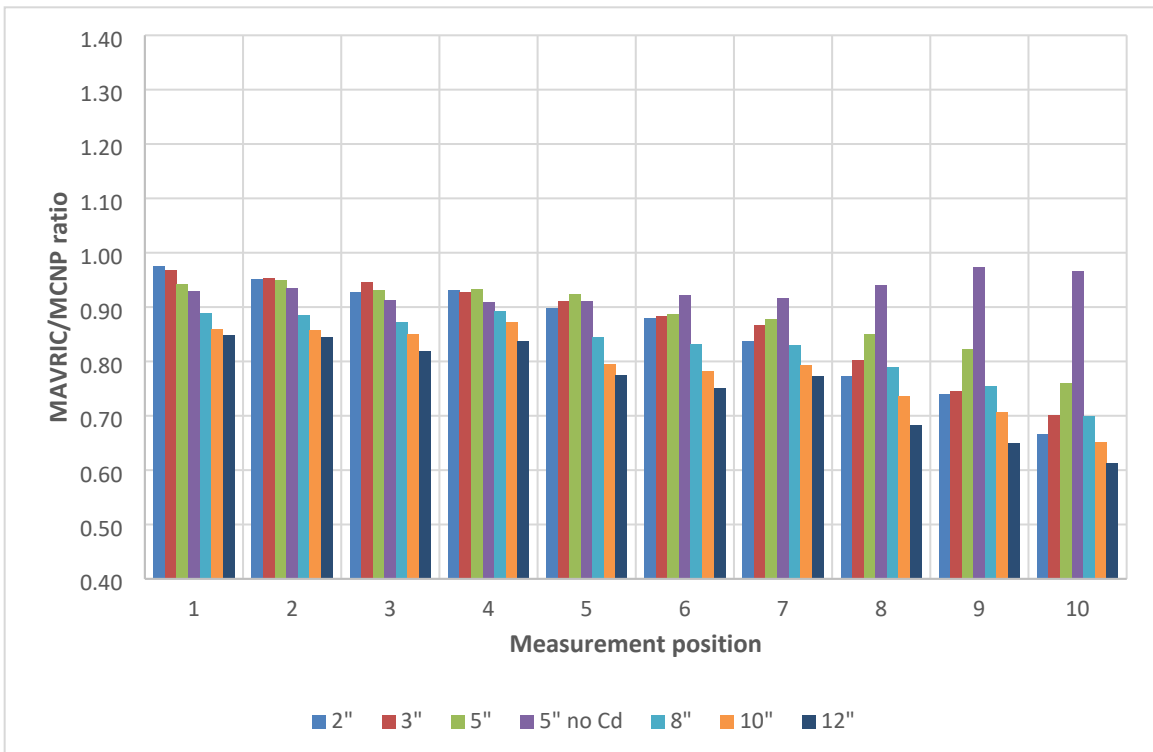


Figure 45. Case 1B MAVRIC/MCNP calculation results ratio for the different measurement positions and all Bonner spheres.

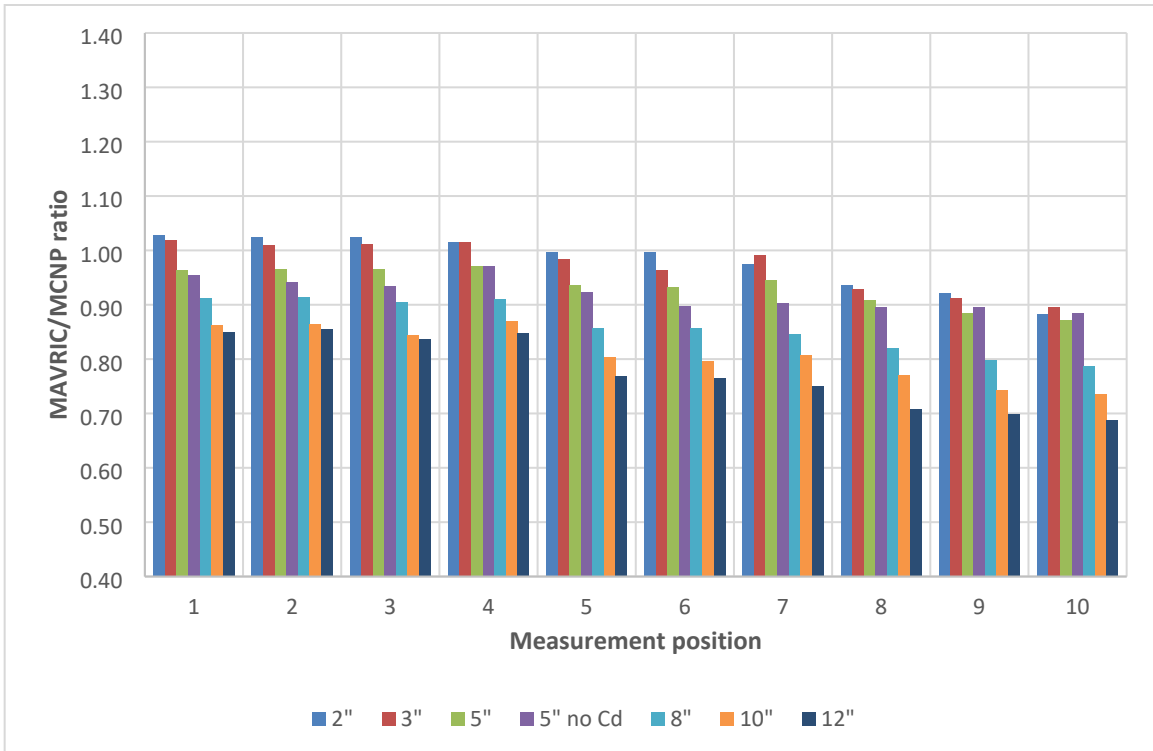


Figure 46. Case 2A MAVRIC/MCNP calculation results ratio for the different measurement positions and all Bonner spheres.

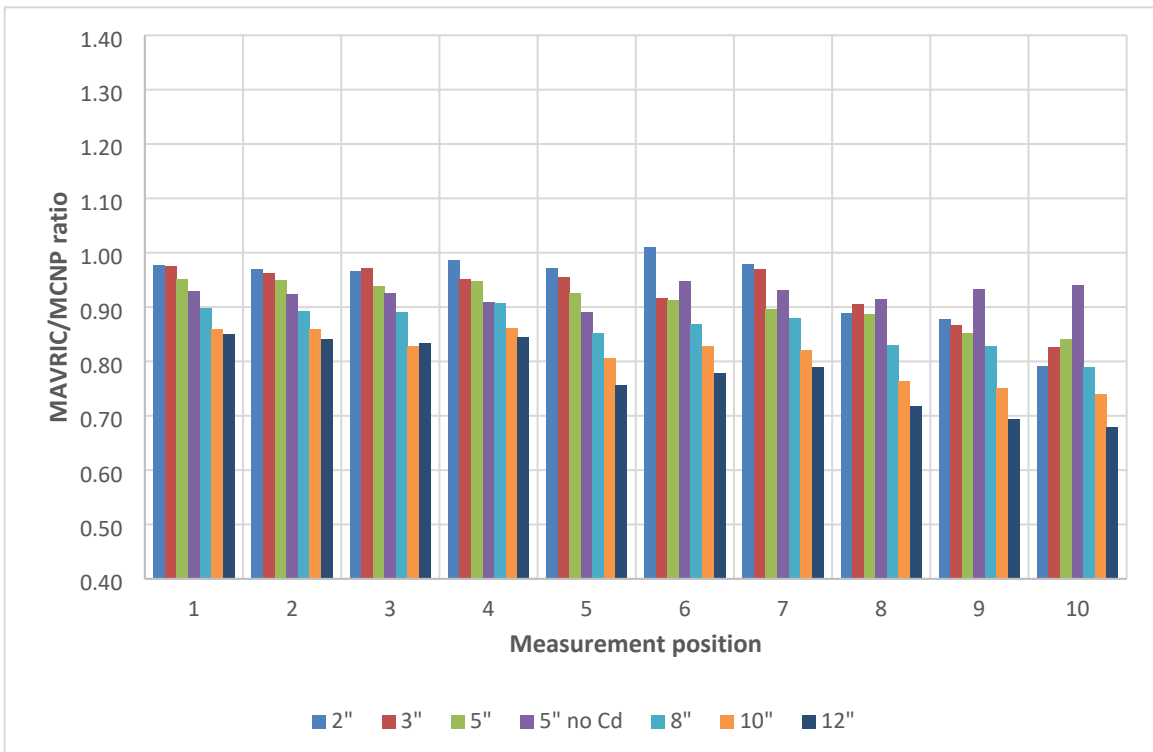


Figure 47. Case 2B MAVRIC/MCNP calculation results ratio for the different measurement positions and all Bonner spheres.

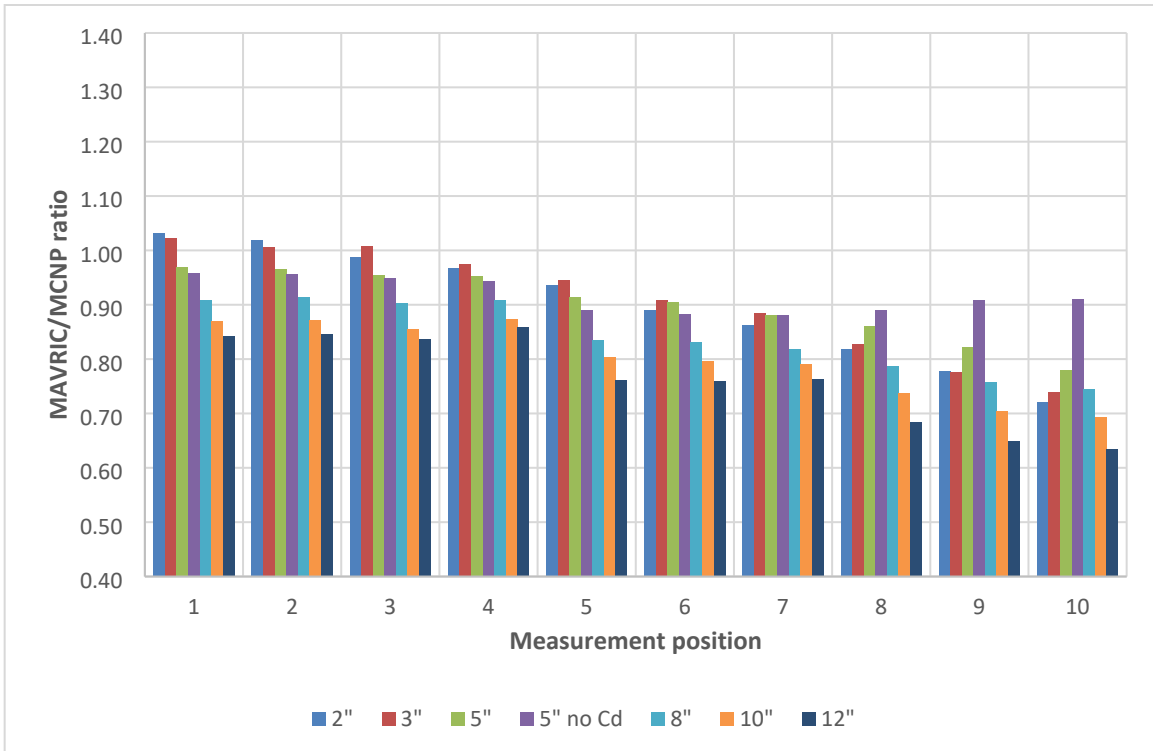


Figure 48. Case 3A MAVRIC/MCNP calculation results ratio for the different measurement positions and all Bonner spheres.

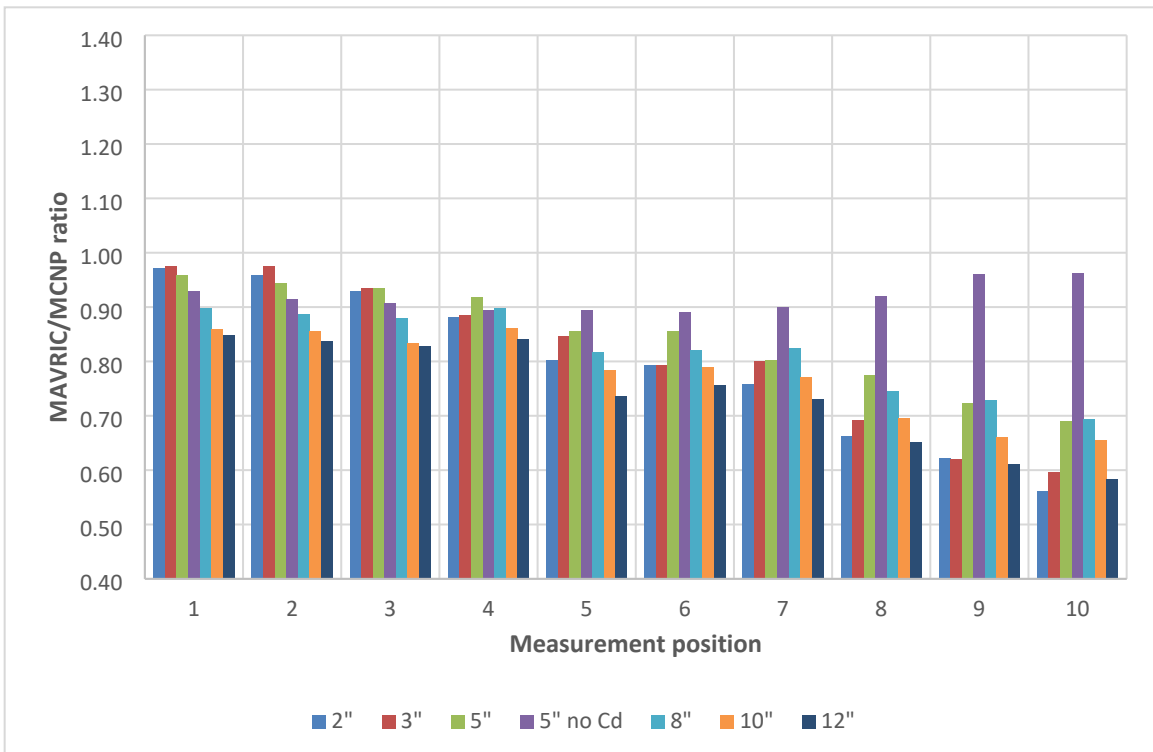


Figure 49. Case 3B MAVRIC/MCNP calculation results ratio for the different measurement positions and all Bonner spheres.

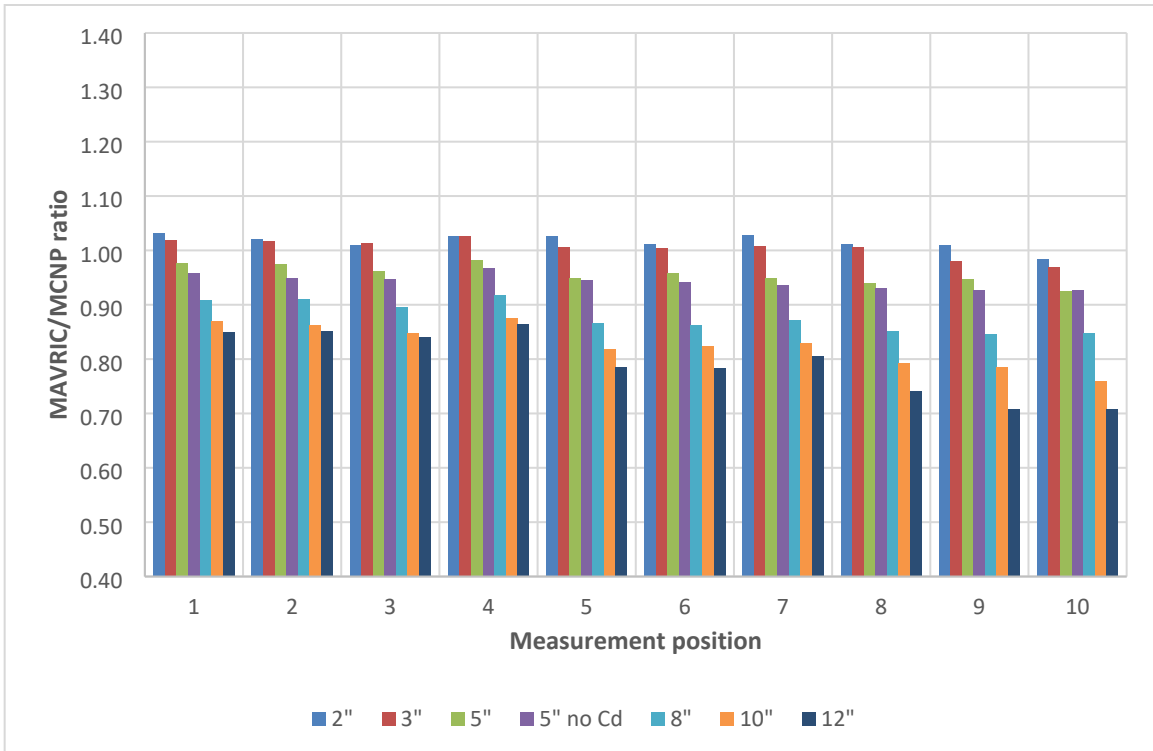


Figure 50. Case 4A MAVRIC/MCNP calculation results ratio for the different measurement positions and all Bonner spheres.

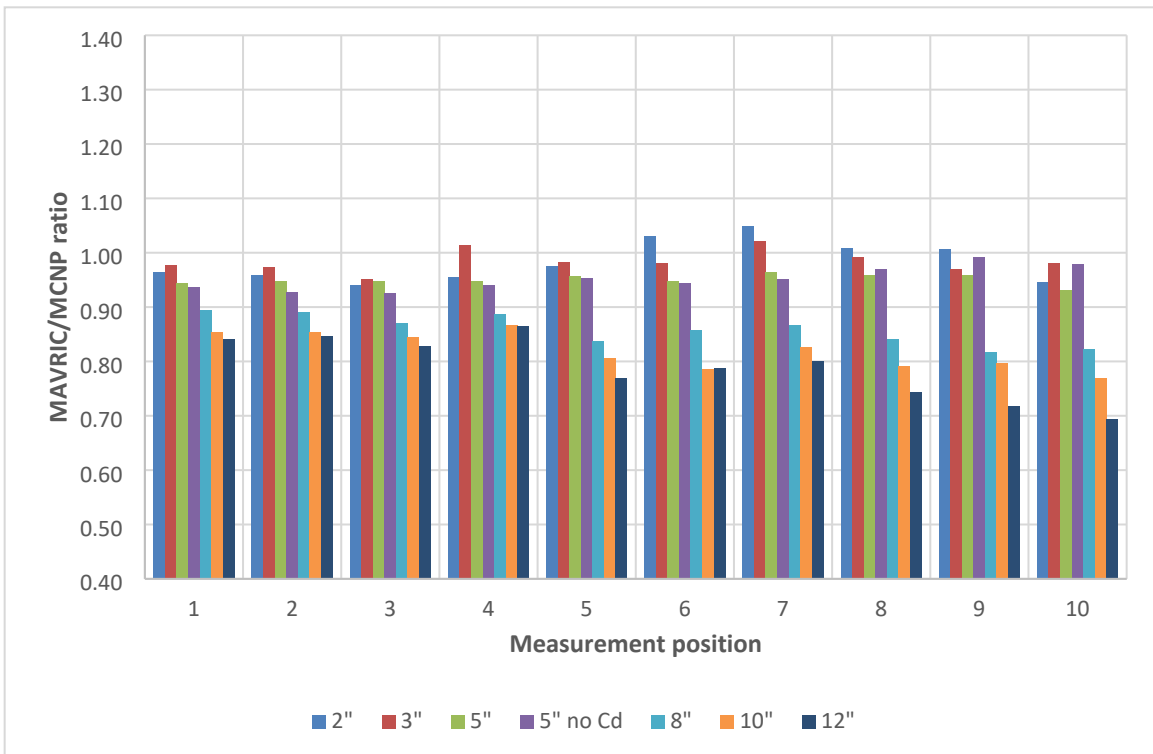


Figure 51. Case 4B MAVRIC/MCNP calculation results ratio for the different measurement positions and all Bonner spheres.

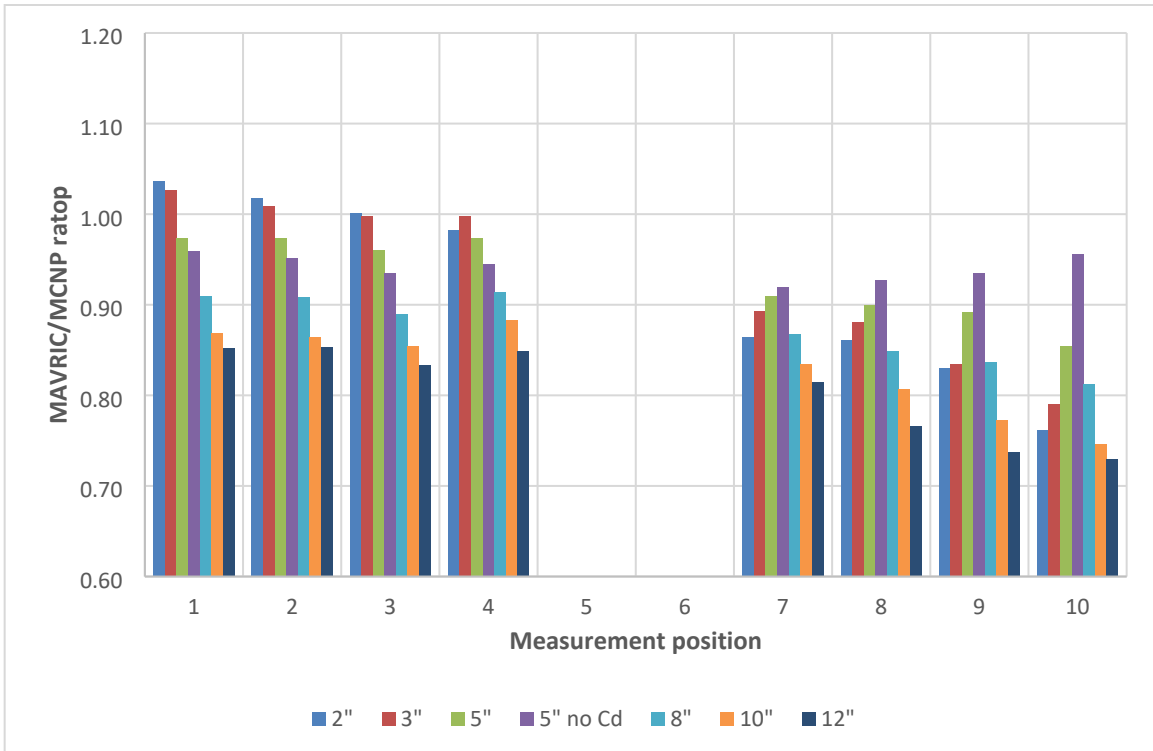


Figure 52. Case 5A MAVRIC/MCNP calculation results ratio for the different measurement positions and all Bonner spheres.

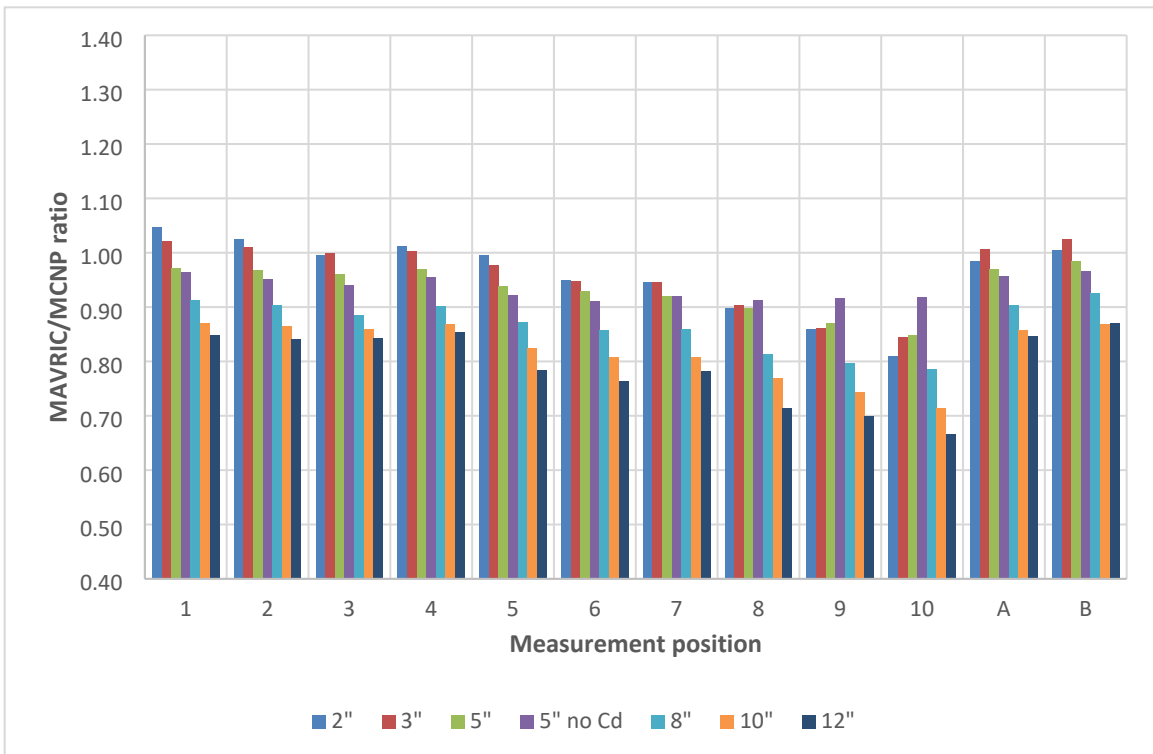


Figure 53. Case 6A MAVRIC/MCNP calculation results ratio for the different measurement positions and all Bonner spheres.

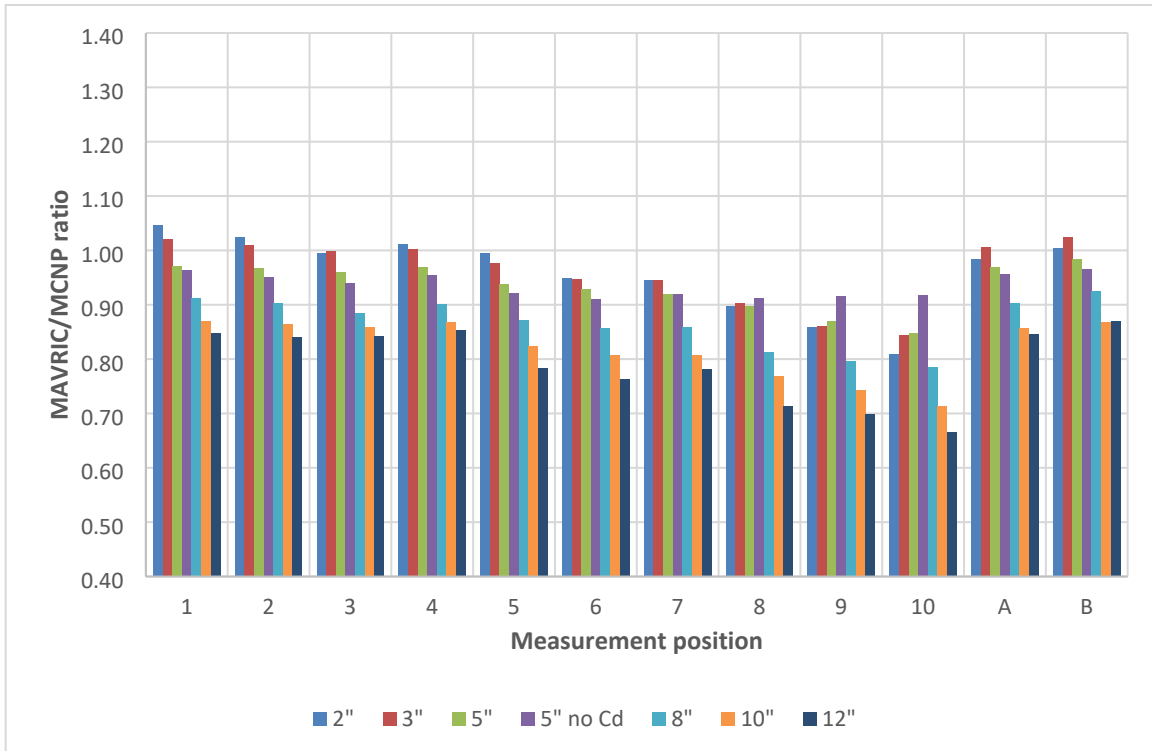


Figure 54. Case 6B MAVRIC/MCNP calculation results ratio for the different measurement positions and all Bonner spheres.

2.4 AM-BE NEUTRON LEAKAGE THROUGH SEVERAL MATERIALS

As part of a larger effort to develop better cross-section libraries, at the National Aeronautics and Space Administration (NASA) Lewis Research Center near Cleveland, Ohio, an experimental team recorded leakage measurements of neutrons from a strong americium-beryllium (Am-Be) source through spherical shells of several materials, mostly metals [22]. The team simulated the experiments, and the results matched the measurements well except for tantalum, but this discrepancy was due to poor cross sections used in the simulations.

2.4.1 Benchmark Model

Bogart’s report describes a series of measurements that included Am-Be neutrons leaking through spherical shells of beryllium, polyethylene, lead, niobium, molybdenum, tantalum, and two different thicknesses of tungsten. The neutron source module was also measured without any surrounding material. Neutron fluxes 2 meters from the source were recorded with a 5×5 cm cylindrical NE-213 liquid scintillator proton-recoil spectrometer. Two measurements were taken, one with and one without a paraffin shadow cone between the source and the detector, to remove background neutrons scattered from the floor and walls.

The source module was made from 16.7 g of Am and 66.8 g of Be that was “intimately mixed” and then cold pressed into a thin steel encapsulation. A second thin steel encapsulation was included to complete the source module. More details on the source can be found in the literature [23]. The emission rate of the source module was measured as $(1.30 \pm 0.08) \times 10^8$ neutrons per second in January 1967. The dates of the transmission measurements are not stated, but the paper containing the results was submitted in August

1973 [22]. Presumably, the measurements occurred within this span of 6 years and 8 months. With a half-life of 432.7 years for ^{241}Am , the nominal source strength could have dropped no more than 1.06%.

The spherical shells for beryllium, polyethylene, lead, niobium, and tantalum were made with solid pieces. Molybdenum was in powder form and was contained within thin stainless steel spheres. Tungsten was in the form of “fine balls” and was also contained by thin stainless steel spheres. Final results for the absolute neutron leakage flux at 2 m after passing through the various materials are presented for about 70 energy bins covering the range of 0.4–12 MeV [22].

The experimental team also performed simulations using a source strength 4.2% less than the stated strength to account for the $^9\text{Be}(n,2n)$ multiplication that occurs inside the source material. The team also give a table of the neutron source energy distribution for the “virgin (α,n) spectrum”—the energy distribution of the neutrons directly from the $^9\text{Be}(\alpha,n)$ —which was obtained from measurements using a smaller (higher resolution) scintillator. The authors also processed their simulated fluxes with a resolution function for their NE-213 liquid scintillator to their simulations, which tended to smear out the peaks of the simulations to match the measurements better.

2.4.2 Benchmark Results

Nine MAVRIC simulations were performed for the nine cases presented in Table III of the report from Bogart et al.: the bare source module and spherical shells of beryllium, polyethylene, lead, niobium, molybdenum, tantalum, and tungsten (small and large shells), as shown in Table 16. Material densities and compositions were given, as well as the dimensions of the spherical shells and thicknesses of the steel containers for Mo and W. The geometry of the simulation consisted of spherical shells: several for the source module, a few for the shield material, and two to define a tally region at 2 meters.

Table 16. Summary of Am-Be source module spherical shells cases studied.

Cases	Source module spherical shell characteristics	Simulated and measured flux comparisons
1	Bare source module	Figures 55 and 56
2	Beryllium shell	Figures 57 and 58
3	Polyethylene shell	Figures 59 and 60
4	Lead shell	Figures 61 and 62
5	Niobium shell	Figures 63 and 64
6	Molybdenum shell	Figures 65 and 66
7	Tantalum shell	Figures 67 and 68
8	Tungsten small shell	Figures 69 and 70
9	Tungsten large shell	Figures 71 and 72

MAVRIC is a fully three-dimensional (3D) code, but these models were spherically symmetric, so they were essentially one-dimensional (1D). For the simulations in this work, the virgin source distribution was used with a strength of 1.235×10^8 n/s, which was 5% below the January 1967 emission rate. This accounts for some drop in strength for when the measurements were made, and it avoids double counting the $^9\text{Be}(n,2n)$ multiplication in the source material. CE cross sections were used, and each simulation was run for about 30 minutes on a desktop computer to reduce the relative uncertainties in the tally bins. In most simulations, all energy bins had less than 1% uncertainty; the others had at least 93% of the bins with less than 1% uncertainty. No detector resolution function was applied to the energy-dependent fluxes computed by MAVRIC.

Comparisons of the simulated results to the measured results, as well as the bin-by-bin ratio of simulation flux to measurement flux, are shown in the Figure 55 through Figure 72. For each of the nine cases, a first figure shows the MAVRIC and measured leakage fluxes along with their uncertainties. The second figure for each simulated case shows the ratio on the simulated values to the measured values. Note that these figures show comparisons of the absolute flux at 2 meters for the given source strength: these are not normalized distributions. The error bars shown in the ratio plots are almost entirely due to measurement uncertainty (not the uncertainties in the simulated values). Overall, the simulations match the measured leakage energy distributions, but they contain several features that would be “smoothed out” by the detector energy resolution. The reader should also note that the virgin source distribution included neutrons up to 11.331 MeV, but the measurements show leakage fluxes in three bins above that maximum source energy, which again shows the impact of the detector resolution function.

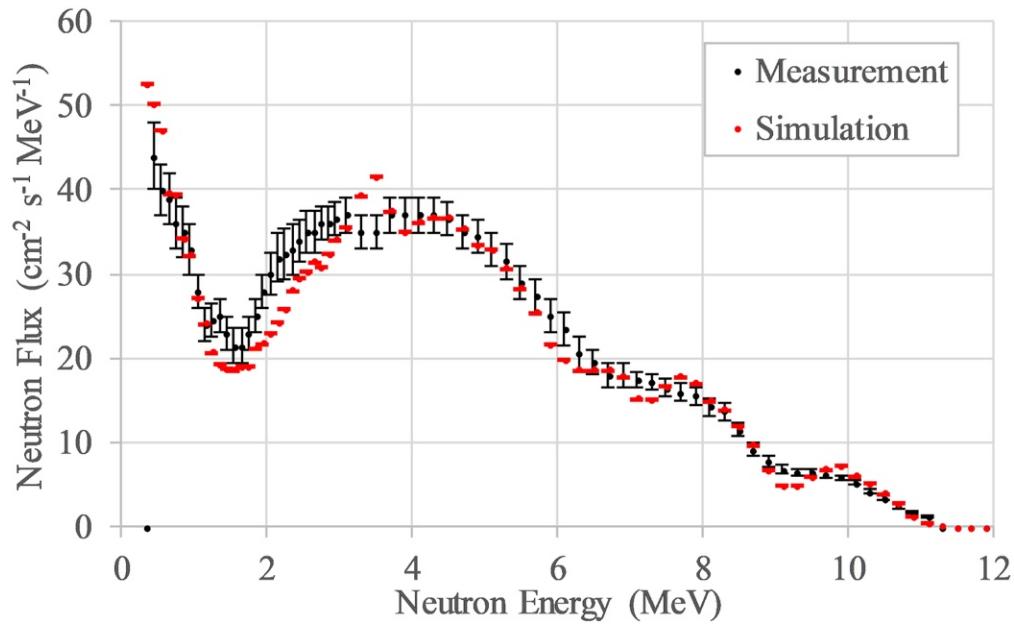


Figure 55. Leakage flux measurements and MAVRIC simulation from the Case 1 bare source module.

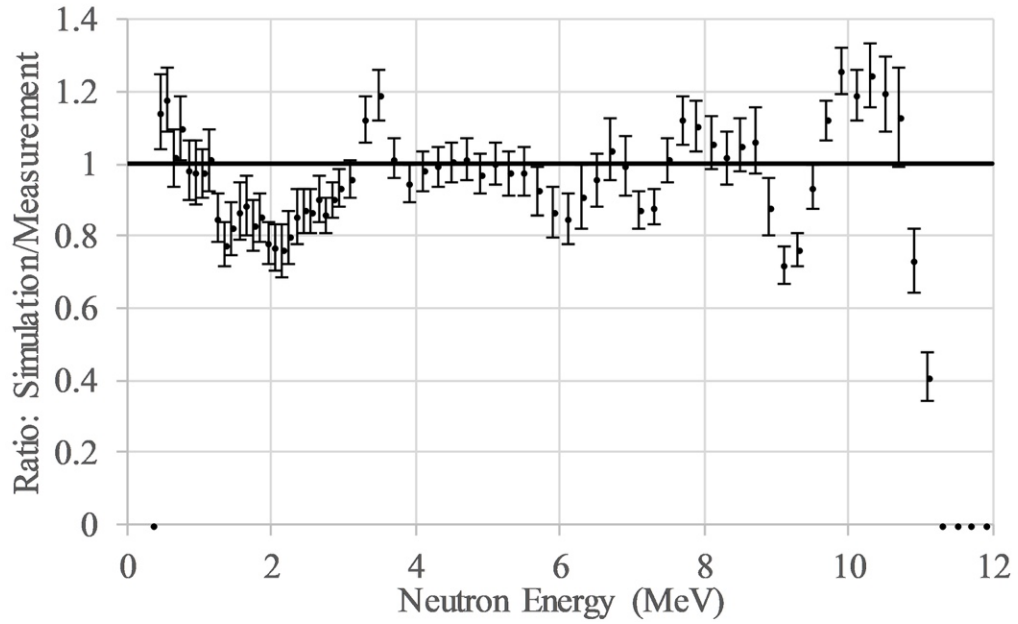


Figure 56. Ratio of the MAVRIC-simulated leakage fluxes to the measurements from the Case 1 bare source module.

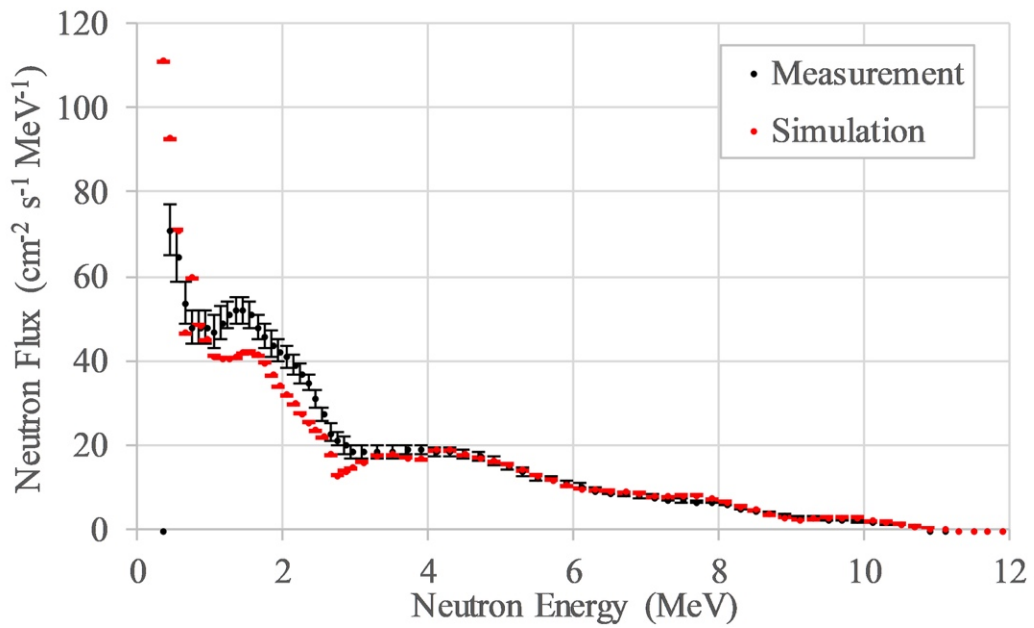


Figure 57. Leakage flux measurements and MAVRIC simulation from the Case 2 beryllium spherical shell.

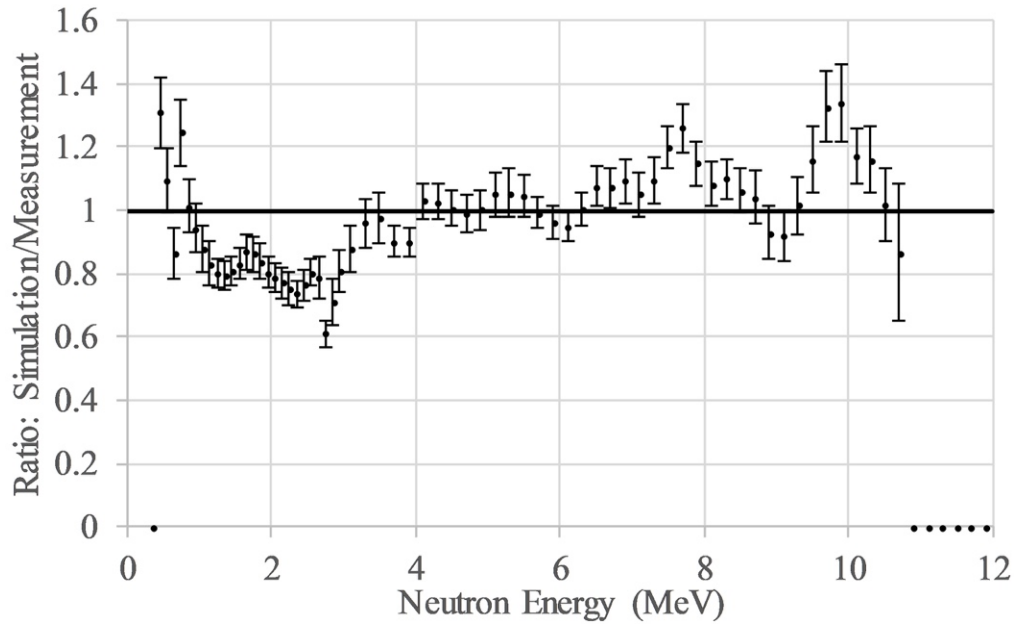


Figure 58. Ratio of the MAVRIC-simulated leakage fluxes to the measurements from the Case 2 beryllium spherical shell.

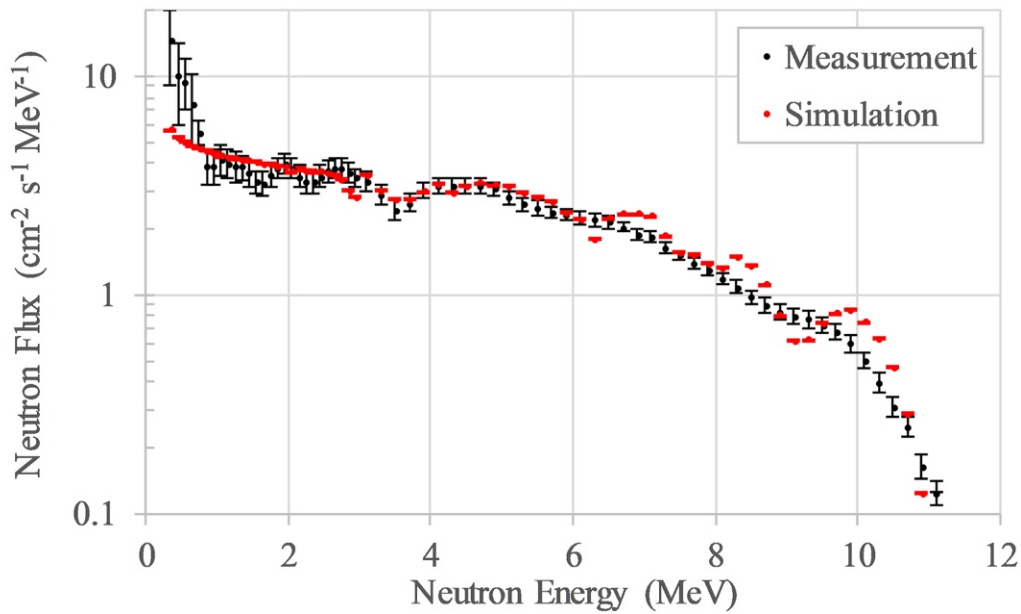


Figure 59. Leakage flux measurements and MAVRIC simulation from the Case 3 polyethylene spherical shell.

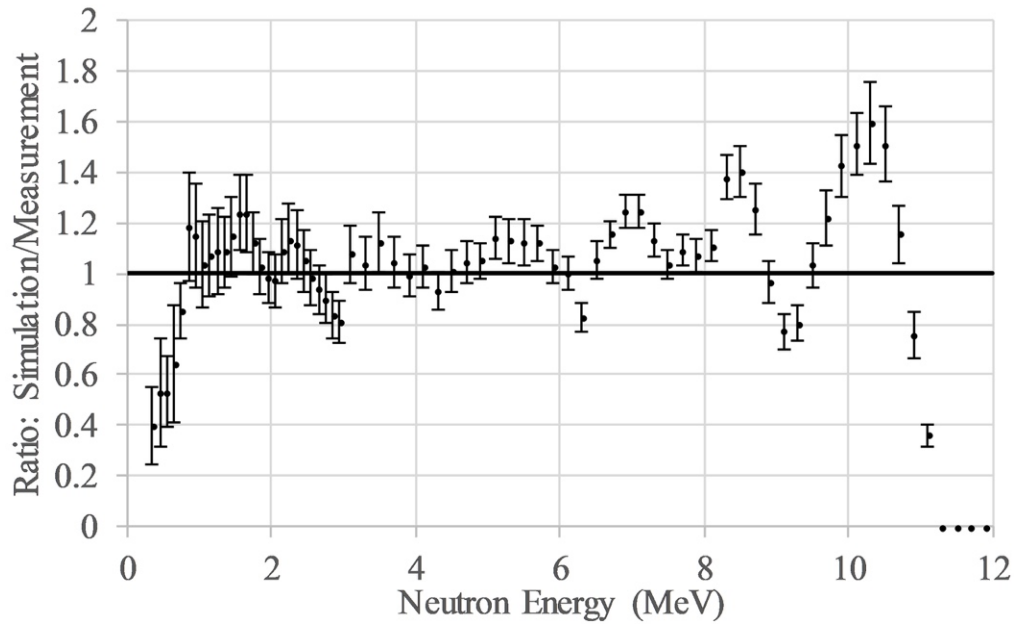


Figure 60. Ratio of the MAVRIC-simulated leakage fluxes to the measurements from the Case 3 polyethylene spherical shell.

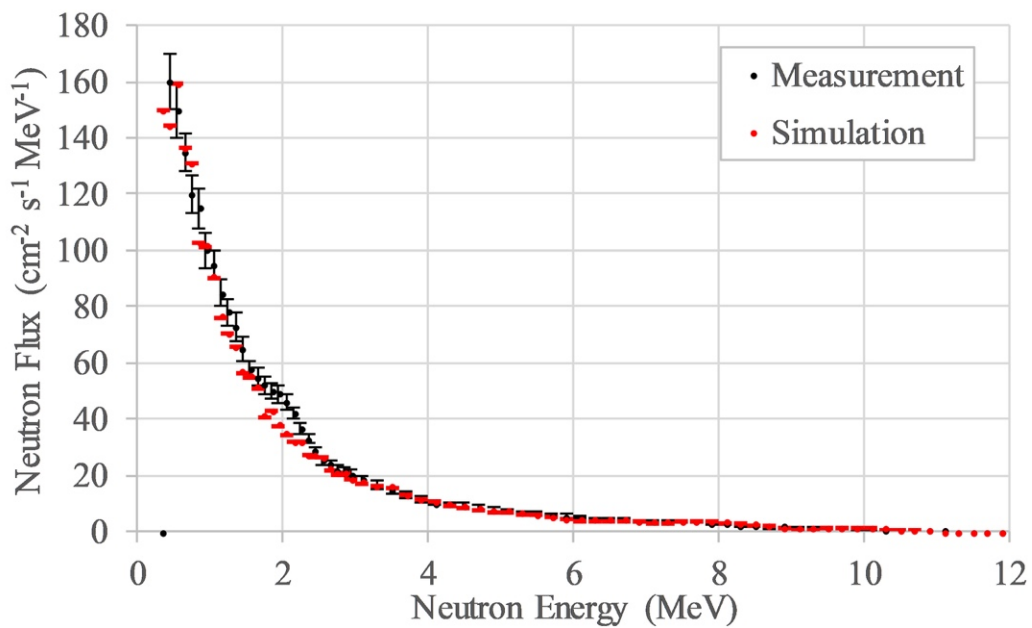


Figure 61. Leakage flux measurements and MAVRIC simulation from the Case 4 lead spherical shell.

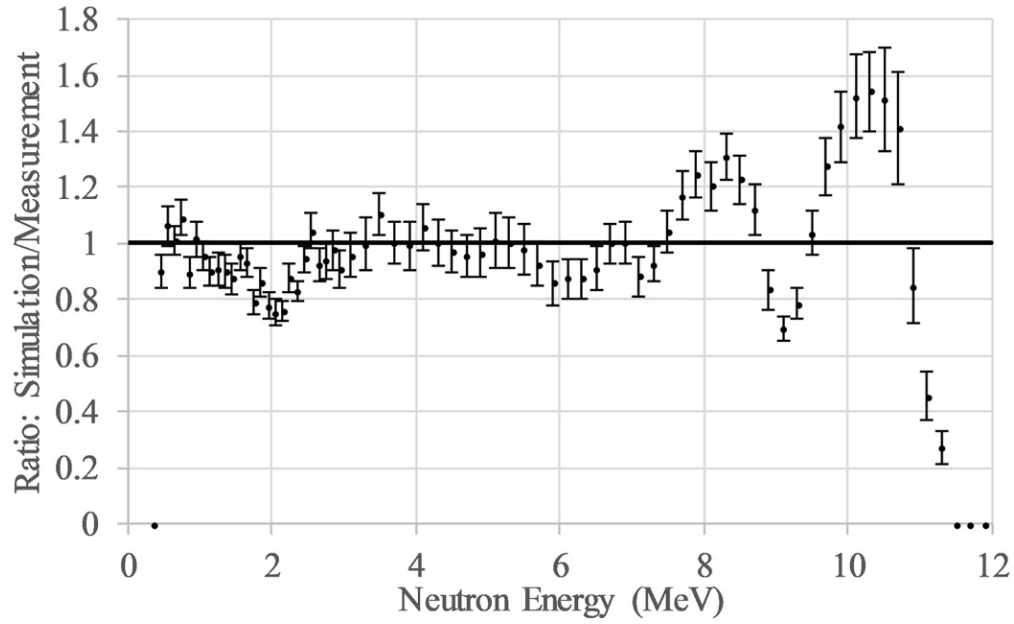


Figure 62. Ratio of the MAVRIC-simulated leakage fluxes to the measurements from the Case 4 lead spherical shell.

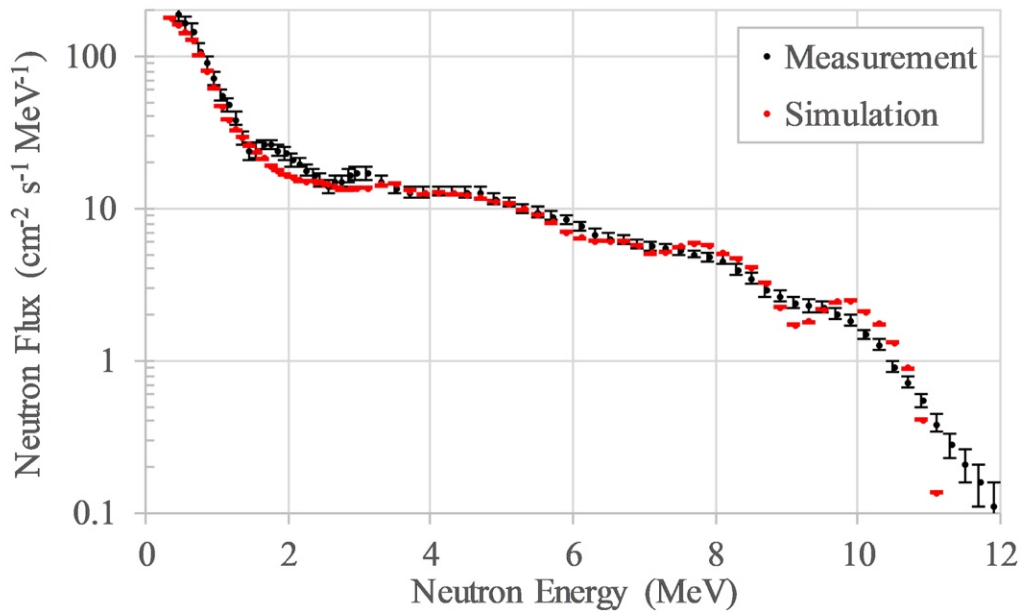


Figure 63. Leakage flux measurements and MAVRIC simulation from the Case 5 niobium spherical shell.

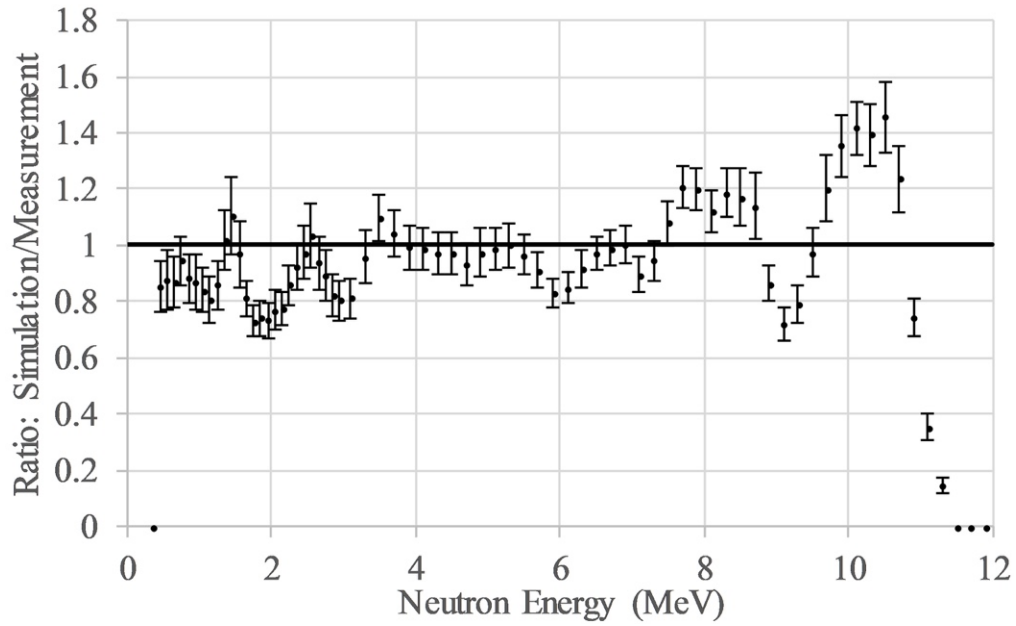


Figure 64. Ratio of the MAVRIC-simulated leakage fluxes to the measurements from the Case 5 niobium spherical shell.

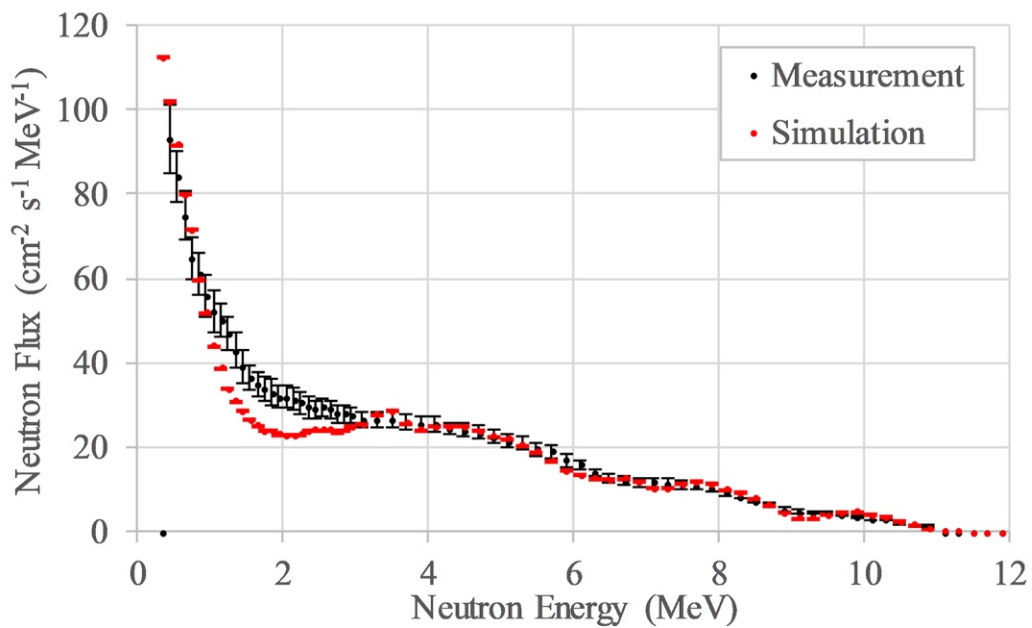


Figure 65. Leakage flux measurements and MAVRIC simulation from the Case 6 molybdenum spherical shell.

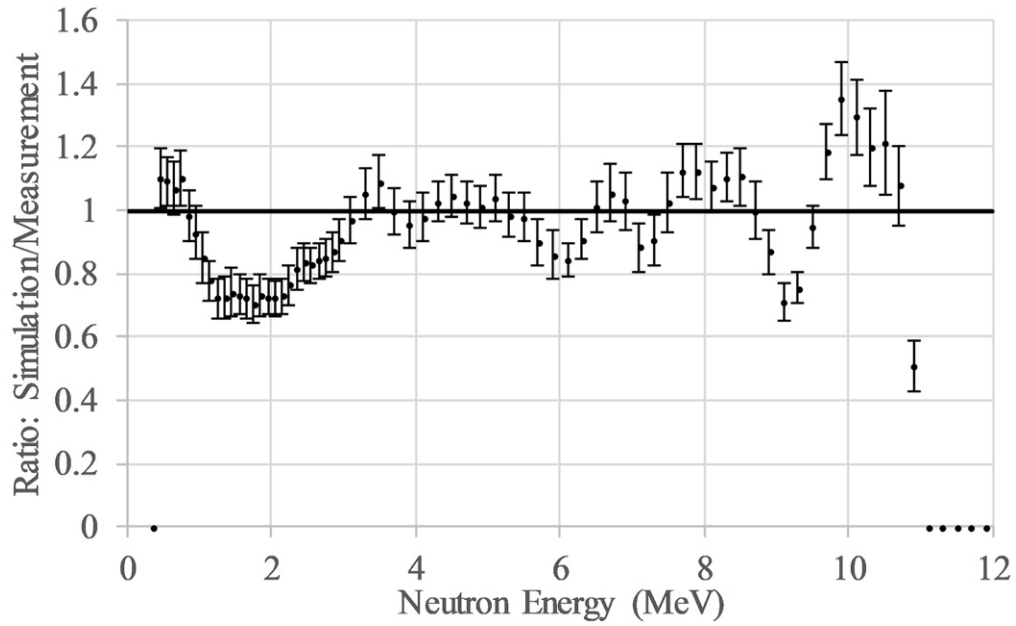


Figure 66. Ratio of the MAVRIC-simulated leakage fluxes to the measurements from the Case 6 molybdenum spherical shell.

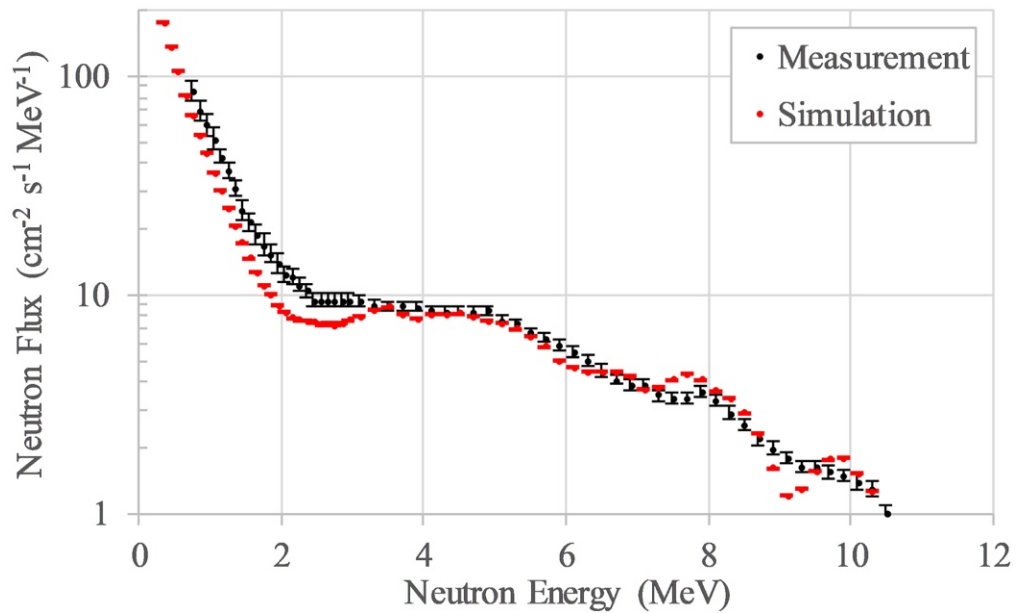


Figure 67. Leakage flux measurements and MAVRIC simulation from the Case 7 tantalum spherical shell.

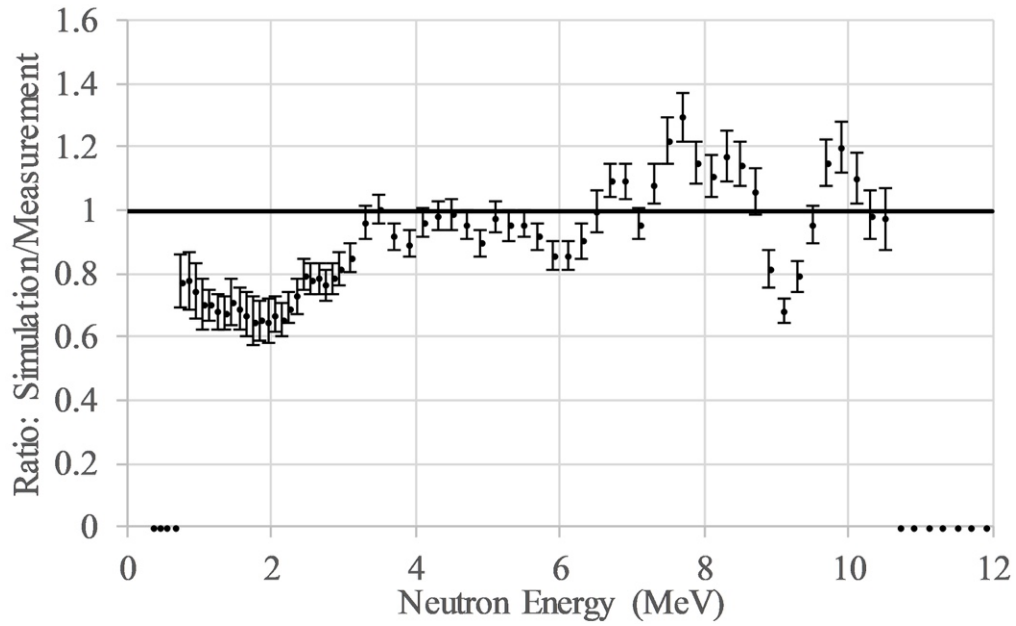


Figure 68. Ratio of the MAVRIC-simulated leakage fluxes to the measurements from the Case 7 tantalum spherical shell.

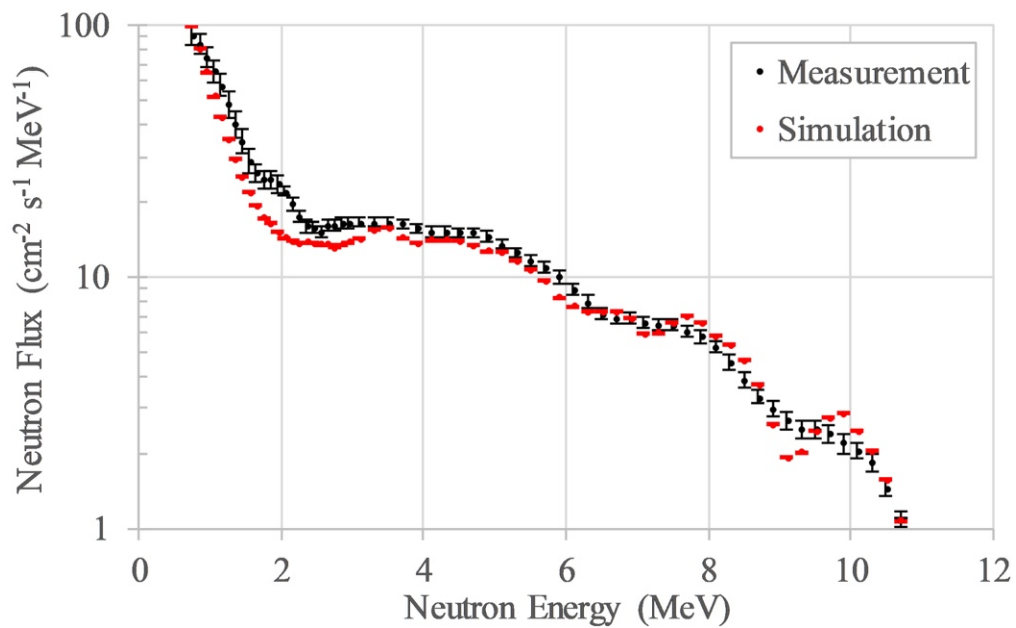


Figure 69. Leakage flux measurements and MAVRIC simulation from the Case 8 small tungsten spherical shell.

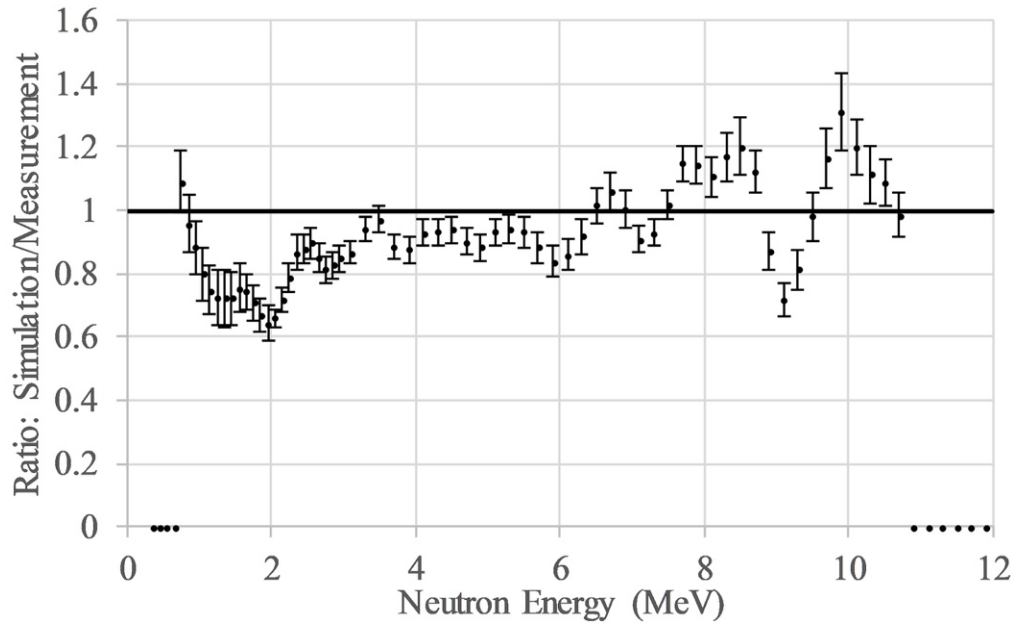


Figure 70. Ratio of the MAVRIC-simulated leakage fluxes to the measurements from the Case 8 small tungsten spherical shell.

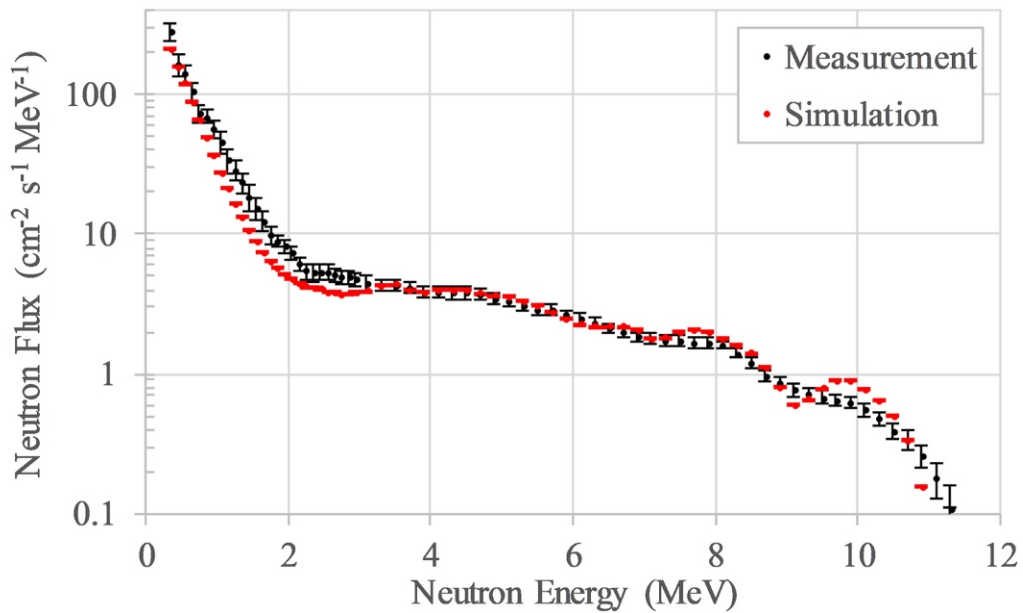


Figure 71. Leakage flux measurements and MAVRIC simulation from the Case 9 large tungsten spherical shell.

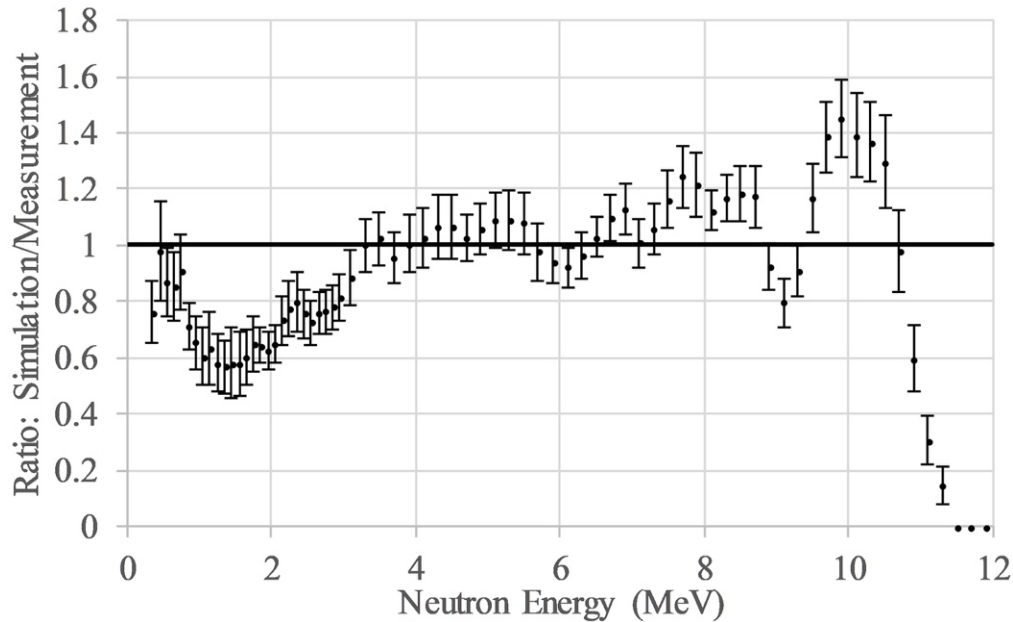


Figure 72. Ratio of the MAVRIC-simulated leakage fluxes to the measurements from the Case 9 large tungsten spherical shell.

2.5 D-T NEUTRONS THROUGH AN IRON SPHERE

Hertel et al. [24, 25] measured the neutron leakage spectra from a deuterium-tritium (D-T) source contained in an iron spherical shell. Williams et al. [26] used these measurements and provided the D-T/D-D source energy distribution and a tabulation of Hertel’s measured leakage values. This measurement is also listed in the SINBAD shielding database [27].

2.5.1 Benchmark Model

The experimental descriptions in the literature are quite detailed. The shell was made of six pairs of symmetric truncated cones with holes to allow placement of the D-T source. The composition of the iron shell is given (0.21% C, 0.013% P, 0.0024 S, 0.47% Mn, balance Fe), as well as the density (7.87 g/cm^3) and the inner and outer radii (7.65 and 38.10 cm). The D-T source was found to have a 5% D-D component and was carefully monitored to accurately scale the measured leakage flux values, with the final result expressed as flux per unit source. The detector was an NE-213 spectrometry system. The source and detector were both located 1m above the concrete floor, with a distance of $265 \pm 1 \text{ cm}$ between them. A second measurement with a paraffin shadow cone was made to account for background. The differences between the two measurements were processed with an unfolding code to arrive at the final leakage spectrum values. Uncertainties in the final values were as small as a few percent, ranging up to 83%. The experimenters reported that the “neutron leakage spectrum has oscillations above 4 MeV that have not been attributed to structure in the neutron energy spectrum in this work” [24].

2.5.2 Benchmark Results

The MAVRIC simulation source used the D-T/D-D source energy distribution [25] over a sphere with a radius of 0.24 cm in the center of the central void, similar to that of Hertel’s simulations [24]. A spherically symmetric geometry was used (no penetrations), and the flux was tabulated for a thin spherical shell at a radius of 265 cm. The tally used bins with center energies corresponding to the energies of the measurement data given by Williams et al. A lower neutron energy cutoff corresponding

to the lowest tally bin was used to improve the speed of the simulation. Without any variance reduction, MAVRIC sampled 10^8 neutrons from the source distribution, giving less than 1% uncertainty in all energy bins in 75 minutes on a desktop computer.

As in the work performed by Hertel et al. and Williams et al. which used older codes and older cross-section evaluations, the leakage values computed by MAVRIC match the measurement peak above 10 MeV well, but the leakage values are significantly lower than the measurement values in the 1–5 MeV range. A comparison of the MAVRIC simulation to the measured values is shown in Figure 73.

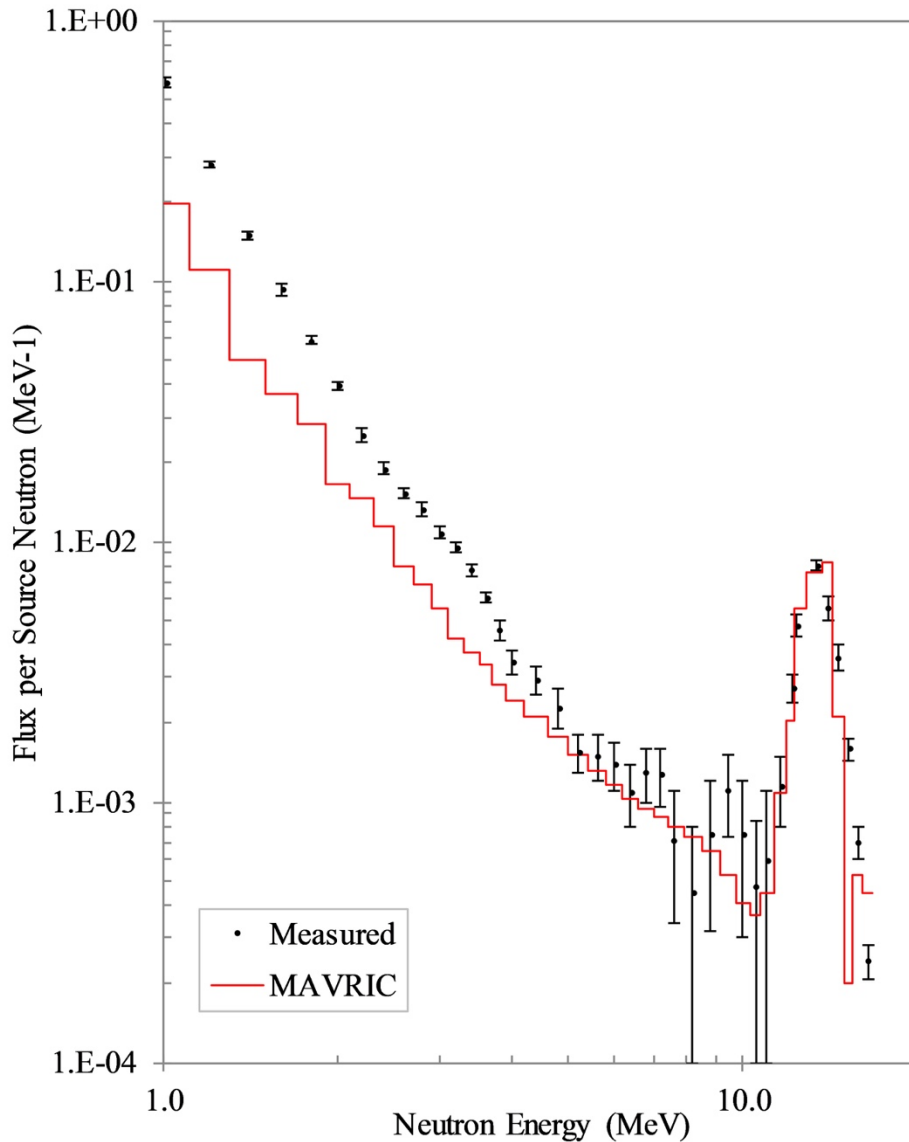


Figure 73. Measured values of the neutron leakage spectrum from a D-T/D-D source inside an iron sphere and the MAVRIC simulation results. MAVRIC uncertainties are too small to be seen.

2.6 UEKI SHIELDING MEASUREMENTS

In the mid-1990s, Ueki and colleagues [28, 29] conducted ^{252}Cf neutron transmission measurements through slab layers of different shielding materials, as well as combinations of different shield materials layered together. During all measurements, the ^{252}Cf source was at the center of a $50 \times 50 \times 50$ cm cube of paraffin with a 45° cone cutout facing the shields and detector. (Note that Ref. 28 says the source was located in a block of paraffin and Ref. 29 shows figures with the block labeled as paraffin, but the text of Ref. 29 mentions that a “polyethylene cone” was used to fill the cone-shaped cutout of the block.) The position of the neutron detector was fixed at 115 cm from the source, and the detector side of the shields was fixed at 100 cm from the source. The shield layers were added on the source side, working from the detector toward the source. A measurement was done with no shields to establish the baseline. To account for room shine, the reported measurements were the difference between a measurement without the cone in the paraffin block and a measurement with the cone in place.

2.6.1 Benchmark Model

Three basic types of measurements were performed. Type 1 measurements used 5 or 6 slabs of single material: polyethylene, NS-4-FR, Resin-F, KRAFTON-HB, and stainless steel (SUS-304). Shield slabs were 5 cm thick (except KRAFTON-HB, which was 5.3 cm thick) and were separated by 1 cm when in place. Ueki listed the composition and density of these materials. Figure 74 shows the Type 1 geometry for 3 layers of shielding. Type 2 measurements used either 5 slabs of steel (25 cm) on the source side of the shield and a varying number of polyethylene slabs or a varying number of polyethylene slabs and 5 slabs of steel. This was intended to show the difference in shielding attenuation based on the order and number of shields. Figure 75 shows a Type 2 measurement with 5 layers of steel and 3 layers of polyethylene. Type 3 measurements used eight slabs of material (40 cm), with 5 slabs made of steel (25 cm) and 3 slabs (15 cm) made of polyethylene. The 3 slabs of polyethylene were placed in five possible positions within the set of eight slabs, ranging from starting the first 0–15 cm on the source side to the last 25–40 cm on the detector side. These measurements also used a photon dosimeter that was located 105 cm from the source. Figure 76 shows a Type 3 measurement in which the polyethylene starts at 10 cm from the source side of the shield.

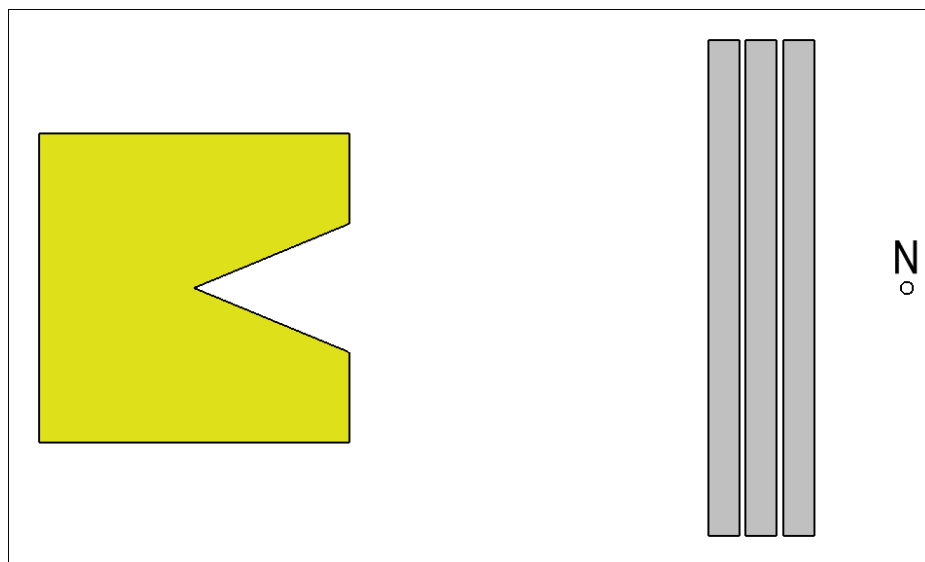


Figure 74. Type 1 measurement geometry: ^{252}Cf source at the apex of a cone cutout in a 50 cm paraffin cube (yellow) with different thicknesses of a single material (light gray) and a neutron detector (N).

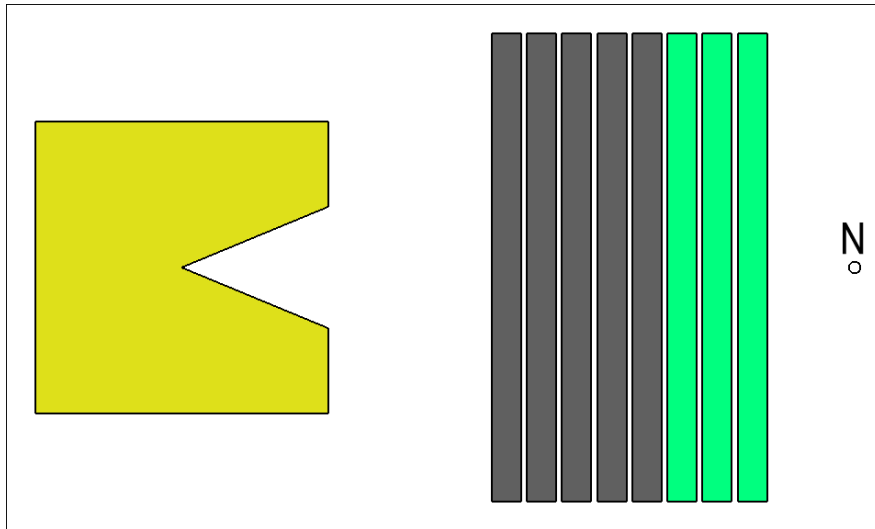


Figure 75. Type 2 measurement geometry: 25 cm of stainless steel (gray) and different thicknesses of polyethylene (green).

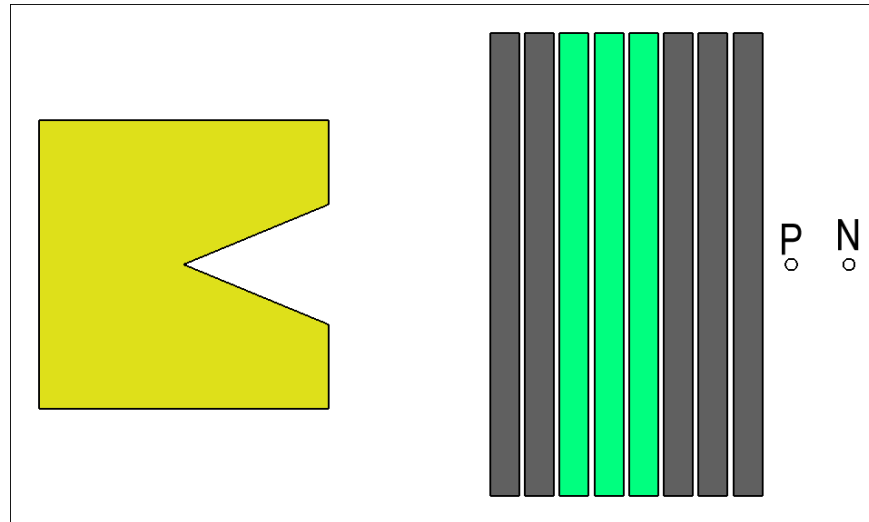


Figure 76. Type 3 measurement geometry – 15 cm of polyethylene (green) at different positions in stainless steel (gray) for a total of 40 cm thickness. Both a neutron counter (N) and a photon counter (P) were used.

Two californium sources were used: one of strength 5.45×10^7 n/s for most of the Type 1 measurements, and one of strength 5.33×10^7 n/s for the steel Type 1 measurements and all the Type 2 and Type 3 measurements. The detector was a “moderator-type neutron survey meter,” and the count rates were converted to dose rate values in $\mu\text{Sv/h}$. The photon detector was a “scintillation-type survey meter.”

Instead of listing final dose rates for measurements, the work by Ueki et al. includes plotted data. The values read from four plots are listed in Table 17 through Table 20, with values corresponding to the different measurement types. There is some uncertainty in reading points from semi-logarithmic plots, which was the approach used to obtain the data in Table 21 through Table 23. These tables show the dose rate values read from different plots for the same experimental setup, and the amount of uncertainty in the process of reading points from plots is evident. For each row in these tables, the measured dose rates should have the same value.

Table 17. Measured values from Type 1 measurements, read from Ueki et al. [29] Figure 2.

Thickness (cm)	Neutron dose equivalent rate ($\mu\text{Sv/h}$)				
	Polyethylene	NS-4-FR	Resin-F	KRAFTON-HB	SUS-304
0	695.2				687.6
5	294.4	297.6	339.7	297.6	488.6
10	110.4	139.2	148.7	123.3	358.9
15	43.11	60.10	64.94	55.00	263.7
20	17.78	27.08	29.59	25.06	191.6
25	7.908	12.62	13.79	12.07	139.2
30	3.058		6.762	5.980	101.1

Table 18. Measured values from Type 2 measurements, read from Ueki et al. [29], Figure 3.

Poly (cm)	Neutron dose rate ($\mu\text{Sv/h}$)	
	Stainless	Polyethylene
	first	first
0	136.3	136.3
5	22.52	49.24
10	4.806	17.52
15	1.566	6.482
20	0.739	2.565
25	0.362	1.179

Table 19. Measured values, read from Ueki et al. [29], Figure 4.

Poly (cm)	Neutron dose rate ($\mu\text{Sv/h}$)	
	Polyethylene	Stainless
	only	first
0	694.0	775.6
5	294.4	339.7
10	113.5	126.9
15	39.81	47.41
20	16.89	20.76
25	7.770	9.687
30	3.476	

Table 20. Measured values from Type 3 measurements, read from Ueki et al. [29], Figure 8.

Poly (cm)	Dose rate ($\mu\text{Sv/h}$)		
	Neutron	Photon	Total
0	6.413	0.100	6.472
5	4.039	0.151	4.151
10	2.735	0.233	2.968
15	2.034	0.351	2.353
20	1.665	0.708	2.353
25	1.591	1.874	3.448

Table 21. Measured values from Type 1 measurements using polyethylene, read from Ueki et al. [29] Figures 2 and 4: results should be the same.

Poly (cm)	Neutron dose rate (μSv/h)	
	Figure 2	Figure 4
0	695.2	694.0
5	294.4	294.4
10	110.4	113.5
15	43.11	39.81
20	17.78	16.89
25	7.908	7.770
30	3.058	3.476

Table 22. Measured values from measurements using 25 cm of stainless steel and various thicknesses of polyethylene, taken from different Ueki et al. [29] Figures 2–4: results should be the same.

Poly (cm)	Neutron dose rate (μSv/h)		
	Figure 2	Figure 3	Figure 4
0	139.2	136.3	135.2
5		22.52	22.48
10		4.806	4.942
15		1.566	1.460
20		0.739	0.694
25		0.362	0.351

Table 23. Measured values from Type 3 measurements, comparing the total dose rate to the sum of the neutron and photon dose rates: results should be the same.

Poly (cm)	Dose rate (μSv/h)	
	Figure 8 total amount	Sum of Figure 8 neutron and photon
0	6.472	6.513
5	4.151	4.190
10	2.968	2.968
15	2.353	2.385
20	2.353	2.372
25	3.448	3.464

2.6.2 Benchmark Results

MAVRIC input files were constructed for the different measurements using the geometry and material information listed in the work by Ueki et al [29]. For the neutron source energy distribution, a Watt spectrum distribution of the form

$$\chi(E) = ce^{-E/a} \sinh(\sqrt{bE})$$

was used, with parameter values from Fröhner [30] ($a = 1.175$ MeV, $b = 1.040$ MeV⁻¹, and c is a normalization constant). For the Type 3 measurements, a photon source was also included. The fission photon energy distribution for ²⁵²Cf was taken from the ENDF data in SCALE, and the number of fission photons per fission neutron was set to 5.4167 based on data from Vega-Carrillo et al. [Vega-Carrillo

2006]. Point detector flux tallies were used to collect the energy-dependent flux and compute the dose rates. For the dose rate response function to be used in the simulations, five different neutron dose per fluence response functions were tested for the Type 1 measurements: ANSI/ANS-6.1.1-1977 [31], ANSI/ANS-6.1.1-1991 [32], International Commission on Radiation Units (ICRU)-57 [33] (both ambient dose and effective dose), and International Commission on Radiological Protection (ICRP)-116 [34]. The response values are shown in Figure 77 and Figure 78. Overall, the ANSI 1977 values matched the measurements from Ueki et al. the best. Only the results using the ANSI 1977 flux-to-dose-rate conversion factors are shown here.

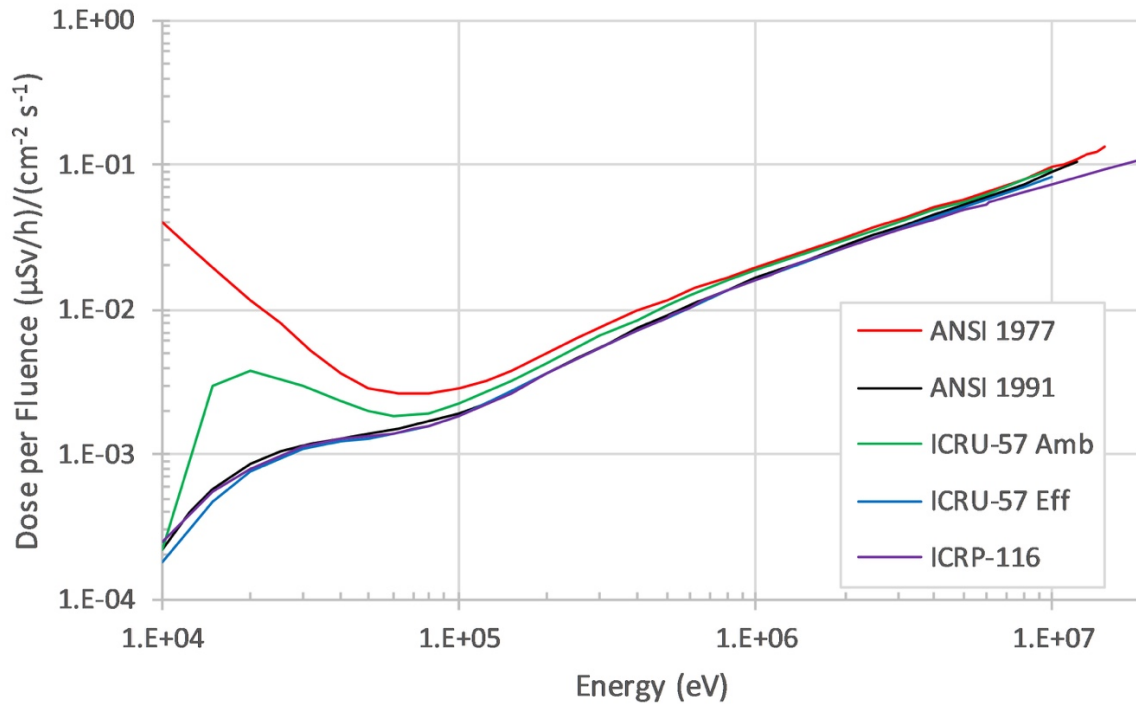


Figure 77. Response functions for computing neutron dose rate ($\mu\text{Sv/h}$) per unit flux ($\text{n cm}^{-2} \text{s}^{-1}$) using a log-log plot.

The CADIS variance reduction option was used in the MAVRIC simulations. The adjoint Denovo calculation times ranged from 1 to 5 minutes on a single AMD Operteron processor. Shorter times were used for thinner Type 1 geometries, and longer times were used for Type 3 coupled neutron and photon calculations. The Monaco Monte Carlo calculation used the SCALE CE cross sections and ran for 30 minutes for each case. A total of 46 cases was run. Simulations of the Type 1 measurements had relative uncertainties of 0.20% – 0.88%. Simulations of the Type 2 measurements had relative uncertainties of 0.75% – 1.3%. Simulations of the Type 3 measurements had relative uncertainties of 1.5% – 7.7% for the neutron dose rates and 3.9% – 8.6% for the photon dose rates.

The report by Ueki et al. does not give the specifics of the room in which the measurements were conducted. The geometry of the simulations was simple enough that no room return would be included. A second set of 46 simulations was performed with the cone cut-out containing paraffin. These values were subtracted from the 46 simulation values that did not include paraffin in the cone region, and the dose rates changed by only small relative amounts. The extra time and effort to run the filled-cone simulations and subtract them from the open-cone simulations appears to be more trouble than it is worth. The results presented below show the dose rates for each measurement computed using a single simulation with an open cone.

For the Type 1 measurements, MAVRIC simulation results matched results from Ueki et al. within about $\pm 20\%$, except for the polyethylene measurement results. Figure 79 shows that with larger amounts of polyethylene, the agreement becomes quite poor. The simulated polyethylene is less attenuating than the measured polyethylene. Figure 80 through Figure 83 show better agreement for the other materials over the whole range of thicknesses measured.

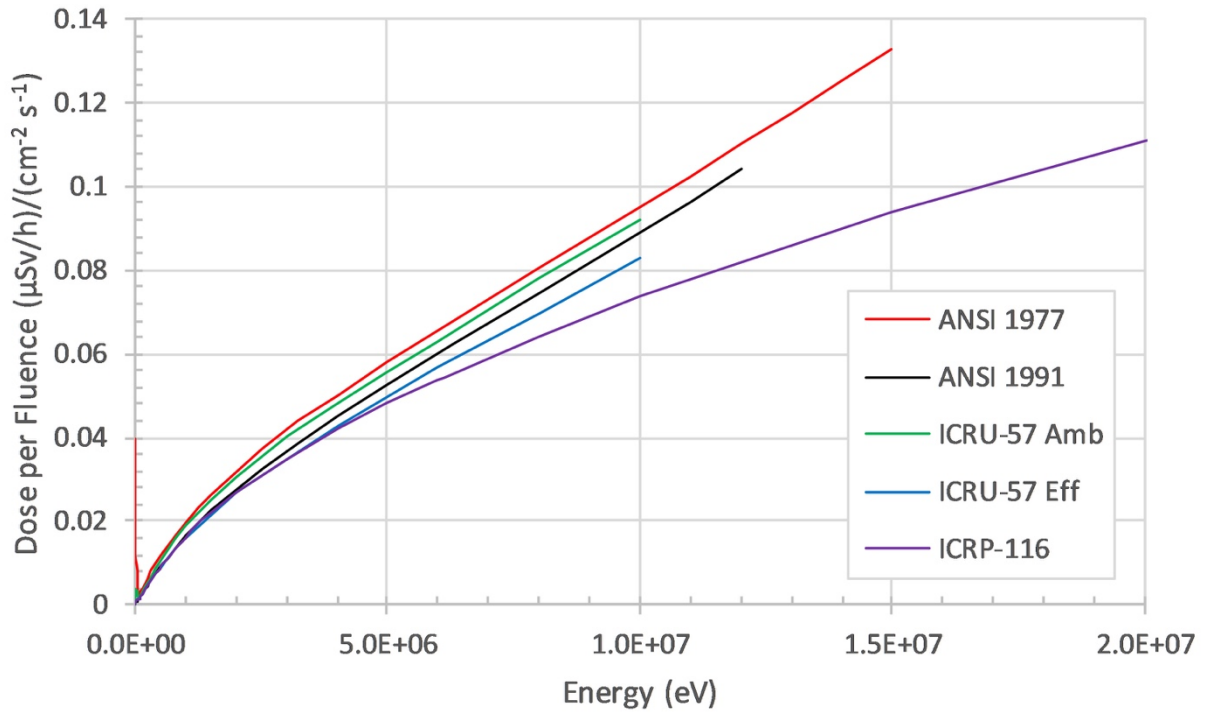


Figure 78. Response functions for computing neutron dose rate ($\mu\text{Sv/h}$) per unit flux ($\text{n cm}^{-2} \text{s}^{-1}$), using a semi-log plot.

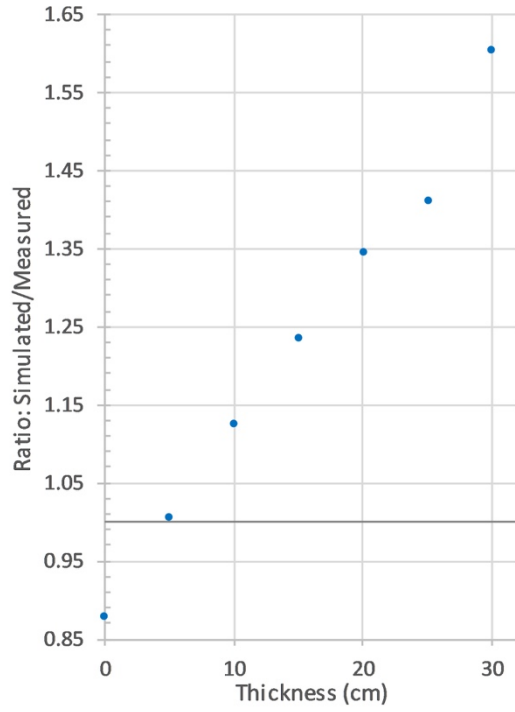


Figure 79. Type 1 measurements: ratio of simulated to measured dose rates with varying thicknesses of polyethylene.

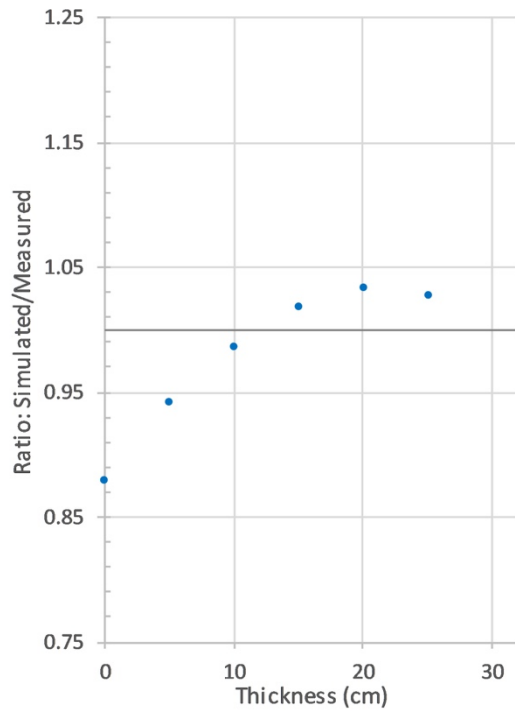


Figure 80. Type 1 measurements: ratio of simulated to measured dose rates with varying thickness of NS4-FR.

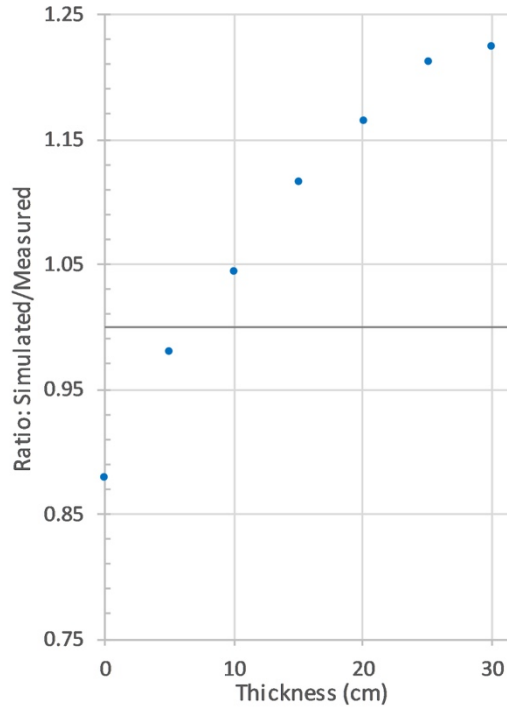


Figure 81. Type 1 measurements: ratio of simulated to measured dose rate with varying thickness of Resin-F.

Simulations of Type 2 measurements with a shield made of 25 cm of stainless steel first (source side) and a varying amount of polyethylene second (detector side) do not compare well with measurements when large amounts of polyethylene are used. The simulated polyethylene is more attenuating than the measured polyethylene (opposite of the Type 1 polyethylene measurements). These results are shown in Figure 84. For the Type 2 measurement with polyethylene first and 25 cm of stainless steel second, shown in Figure 85, the simulations match the measurements within about $\pm 10\%$.

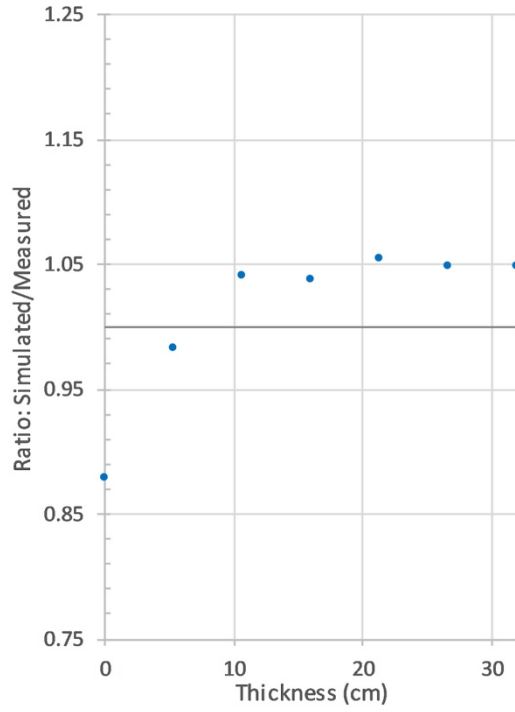


Figure 82. Type 1 measurements: ratio of simulated-to-measured dose rate with varying thickness of KRAFTON-HB.

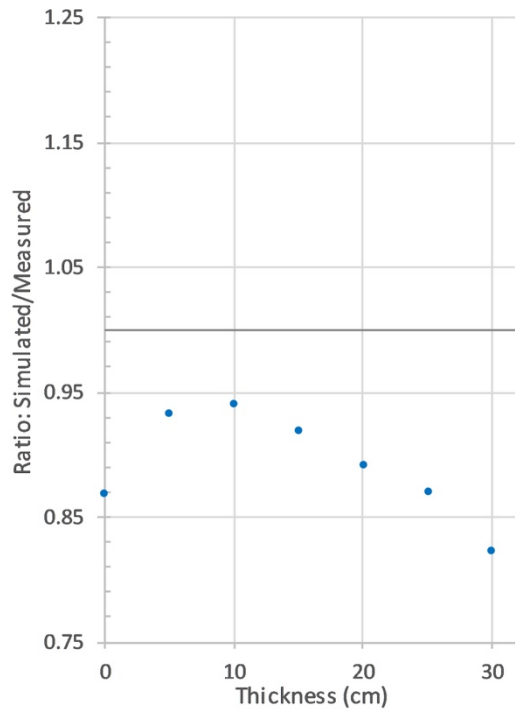


Figure 83. Type 1 measurements: ratio of simulated-to-measured dose rate with varying thickness of SUS-304 (stainless steel).

Type 3 simulations for the neutron and photon dose rates are poor matches to the measurements. Figure 86 and Figure 87 show the ratio of the simulated dose rates to the measured dose rates for neutrons and photons, respectively. Simulated neutron dose rates for when the polyethylene is nearer to the source match measurements in the range of +4% to -8%, but when the 15 cm of polyethylene is positioned closer to the detector side of the shield, simulated dose rates are lower by 30%. Photon dose rates for the polyethylene close to the source are 50% lower than rates from measurements, but they are much closer to the measured rates when the polyethylene is placed nearer to the detector side of the shield. The total dose rates, with dose rate ratios shown in Figure 88, have better agreement only because the proportion of the total dose rate from neutrons and photons happens to emphasize the areas where the simulated individual particle dose rates match measurement rates better. Figure 89 shows the neutron, photon, and total dose rates for both measurements and simulations all in one plot to better illustrate this.

Simulations with MCNP [35] have shown similar difficulty in matching the measurements from Ueki et al. that involve polyethylene.

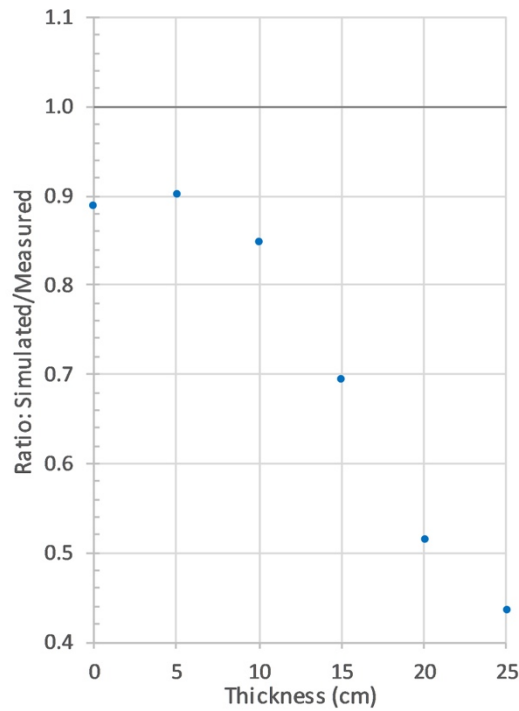


Figure 84. Type 2 measurement: ratio of simulated-to-measured dose rate with 25 cm of steel first and a varying thickness of polyethylene second.

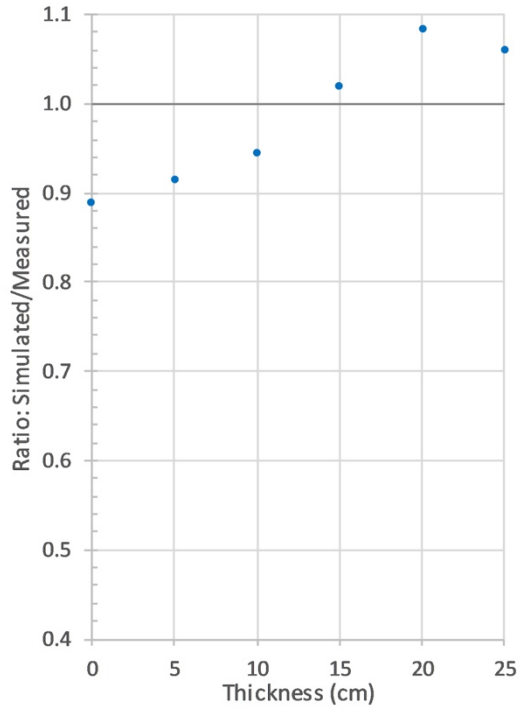


Figure 85. Type 2 measurement: ratio of simulated-to-measured dose rate with a varying thickness of polyethylene first and a 25 cm of stainless steel second.

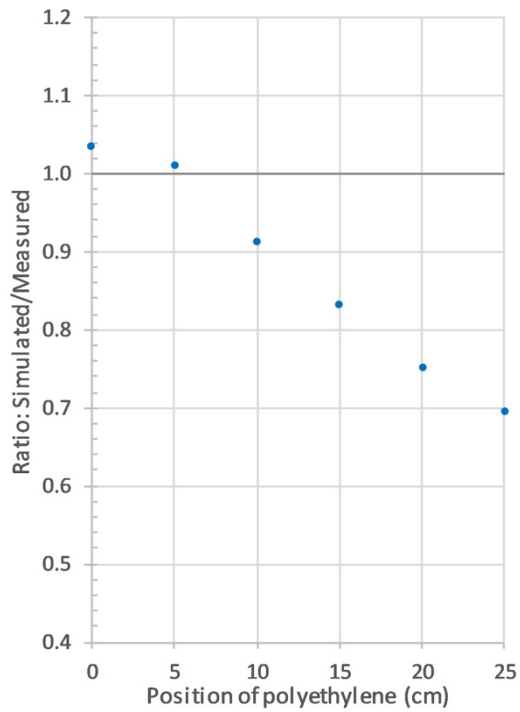


Figure 86. Type 3 measurement: ratio of simulated-to-measured neutron dose rate with a varying position of 15 cm polyethylene in a 40 cm steel/polyethylene shield.

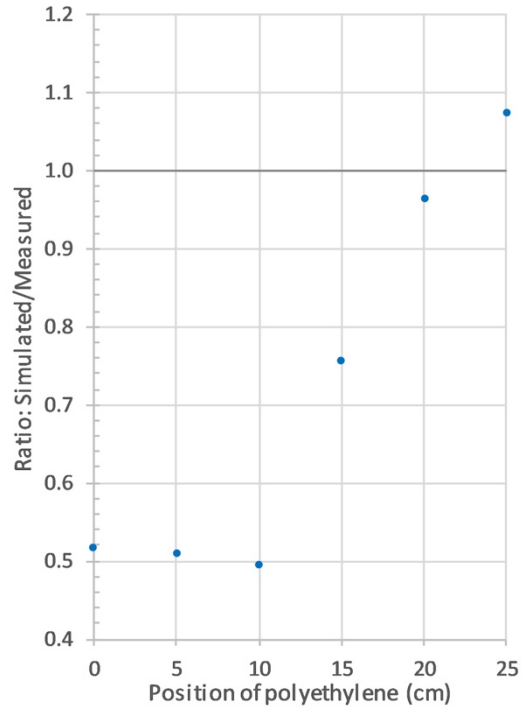


Figure 87. Type 3 measurement: ratio of simulated-to-measured photon dose rate with a varying position of 15 cm polyethylene in a 40 cm steel/polyethylene shield.

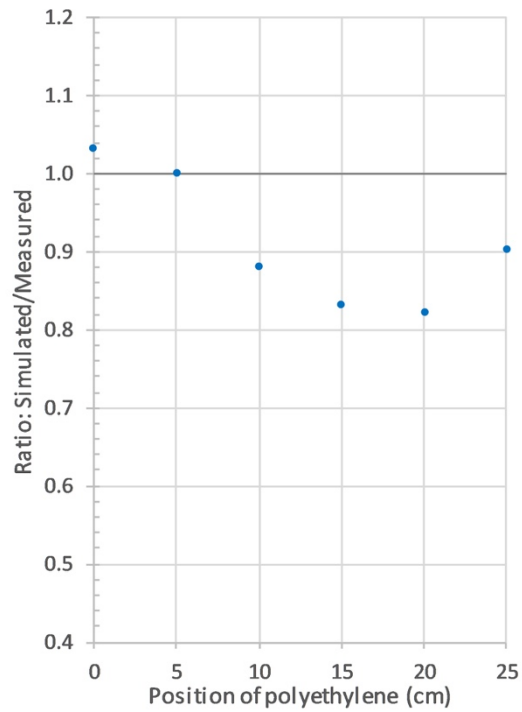


Figure 88. Type 3 measurement: ratio of simulated-to-measured total dose rate with a varying position of 15 cm polyethylene in a 40 cm steel/polyethylene shield.

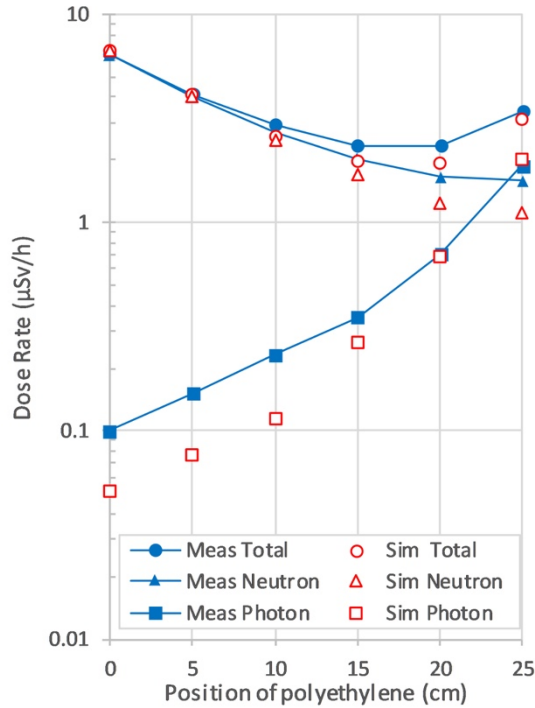


Figure 89. Type 3 measurement: measured and simulated dose rates as a function of the position of the polyethylene with a 40 cm steel/polyethylene shield.

2.7 SKYSHINE BENCHMARK

The photon skyshine experiment was performed at Kansas State University (KSU) in 1977 [36], and related work has been published by others [16, 37-39]. In the KSU experiment, exposure rates due to skyshine radiation produced by three different ^{60}Co sources of 10.33, 229.1, and 3,804 Ci were measured in air at distances of 50, 100, 200, 300, 400, 500, 600, and 700 m from the sources. Each ^{60}Co photon source was placed within a 228.6 cm (7.5 ft) high annular concrete silo with 91.44 cm (3 ft) thick walls. Concrete wedges and lead bricks were installed on the top of the silo to define a 150.5° vertical-conical beam. Each source was horizontally centered within the silo and was raised 2.54 cm above the top of one of the two special purpose-built transportation casks residing inside the silo. The elevation of the sources was 1.98 m above the grade. A 25.4 cm diameter, argon-filled, high-pressure ionization chamber (HPIC) was used to measure the 4π skyshine gamma radiation exposure rate at 1 m above grade. The measured exposure rates were reported per source activity unit. The ^{60}Co sources consisted of nickel-plated ^{60}Co pellets, and the spectra of the gamma rays exiting the three ^{60}Co sources were determined by Monte Carlo (MC) simulations of radiation attenuation within source materials [39]. The benchmark exposure rate measurements were performed on September 26, 1977. The estimated air density on that day was 1.096 kg/m^3 , which was based on reported environmental conditions, including a temperature of 304 K, local pressure of 962 mb, and relative humidity of 32.8%. A schematic drawing of the silo containing the three ^{60}Co sources is shown below in Figure 90. The experiments were conducted at the KSU Nuclear Engineering Shielding Facility. The topography of the location is shown in

Figure 91.

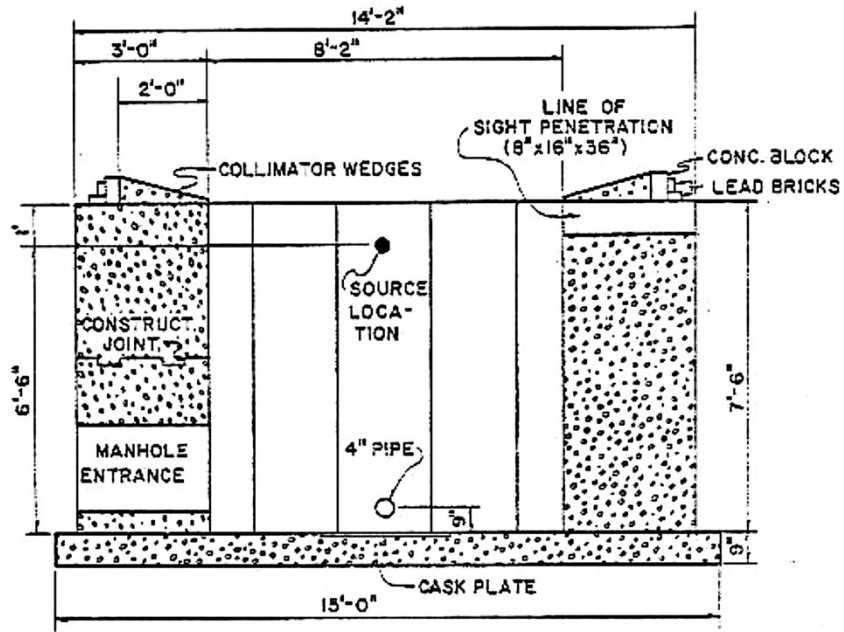


Figure 90. Schematic of the silo used in the experiment, corresponding to Fig. 2-4 from [36].

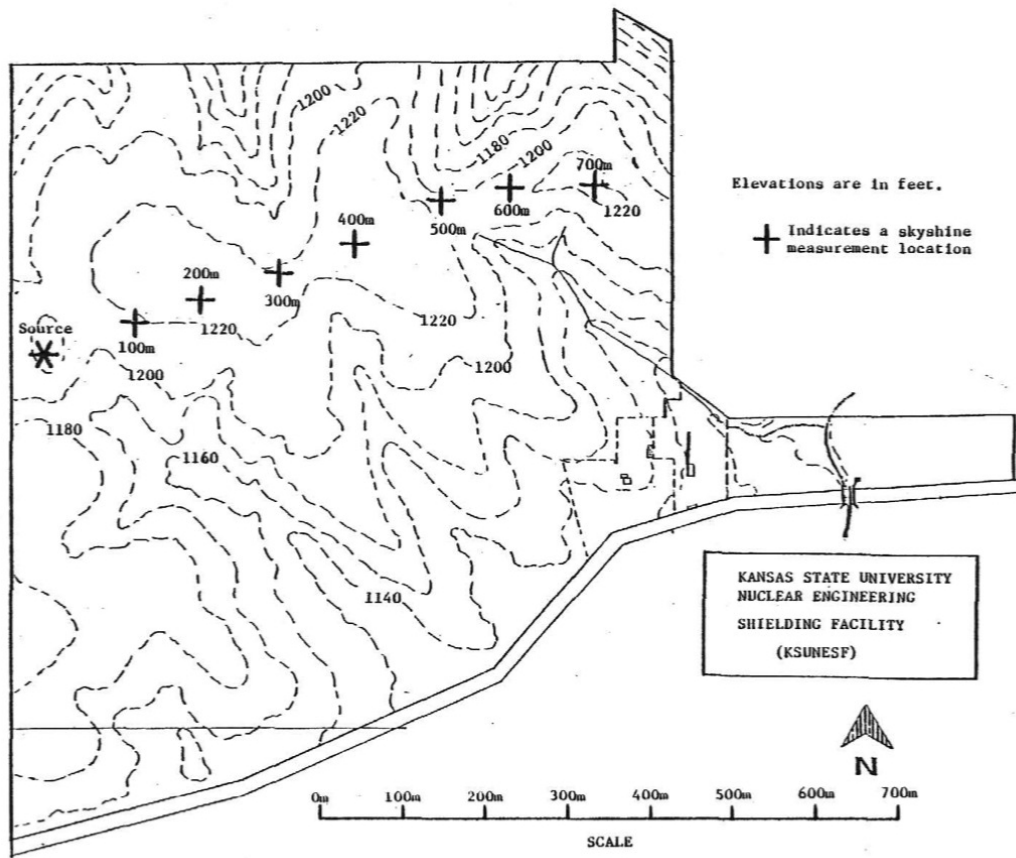


Figure 91. Topography of KSU Nuclear Engineering Shielding Facility, corresponding to Figures 1-3 from [1].

2.7.1 Benchmark Model

The unshielded source configuration of the KSU photon skyshine benchmark experiment [36, 38] was simulated with MAVRIC. This experiment was analyzed with MCNP and included in SINBAD [9], which is available from the Radiation Safety Information Computational Center (RSICC) at ORNL. Only the measurements at 50, 100, 200, 400, 600, and 700 m were included in SINBAD. A total measurement uncertainty of approximately 7% was estimated [36], which includes the uncertainties associated with a required HPIC energy response correction and the reported ^{60}Co source strengths. The uncertainty associated with the benchmark MCNP model [9] was approximately 8%. The largest model uncertainty was attributed to the modeled air density and composition. The silo portion of the SCALE MAVRIC benchmark model is shown in Figure 92.

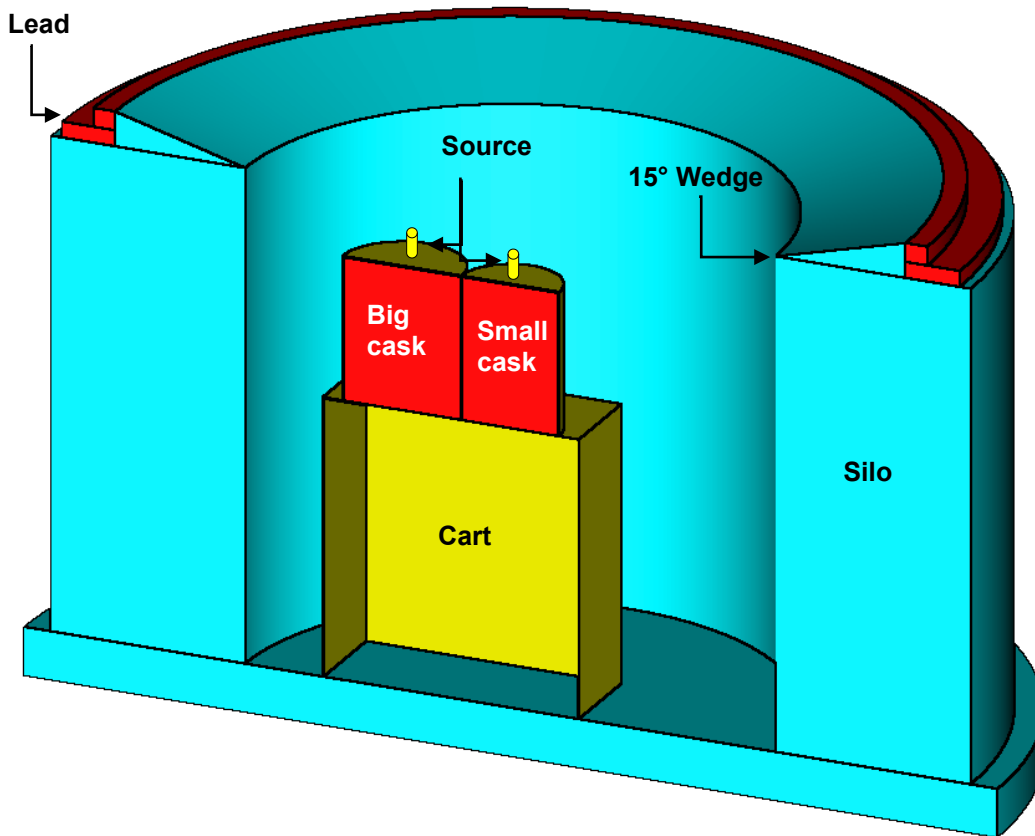


Figure 92. SCALE MAVRIC model of the silo used in the experiment.

2.7.2 Benchmark Results

The response functions in the MAVRIC calculations were ICRU-57 conversion coefficients [33] from photon air kinetic energy release in materials (kerma) in units of $(\text{Gy/h})/(\text{photon}/\text{cm}^2/\text{s})$. The effect of model uncertainty was not evaluated, but it is assumed to be similar to the 8% value determined based on MCNP benchmark evaluations. A comparison with the benchmark experimental data is shown in Table 24. The agreement between MAVRIC and benchmark experimental data is within measurement 2σ uncertainty. The exposure rate map for the strongest source in the experiment, 3804 Ci, is shown below in Figure 93 from the results of the MAVRIC calculations.

The largest disagreement of approximately 25% is between the calculated and measured dose rates and was observed for the mid-range (300 m to 500 m) measurements at 500 m, whereas close- (less than 200 m) and far-range (more than 500 m) calculated dose rates were within the measurement uncertainties. As seen in Table 24, all the mid-range calculated dose rates have similar high disagreements and can be related to either a change in the environment or a change in the detection instruments. For example, the measurement points for the mid-range rates, as shown in

Figure 91, seem to be starting on top of a slightly elevated hill toward the other side of the hill, impacting the direct line of sight contribution from the source as well as contribution from the skyshine particles, which are also reflected back from the surrounding landscape. Unfortunately, there is not enough information to determine the underlying reason for the mid-range discrepancies in the results.

Table 24. Comparison of exposure rates between measurement and calculation.

⁶⁰ Co source activity (Ci)	Distance to source (m)	Exposure rate (μR/h/Ci)				Relative difference (%)
		Measured [relative error %]		Calculated [relative error %] ¹		
10.33	50	24.24	[5]	25.3687	[0.44]	4.66
	100	9.660	[5]	9.6360	[0.39]	-0.25
	200	2.425	[5]	2.5583	[0.38]	5.50
229.1	300	0.760	[5]	0.8844	[0.59]	16.37
	400	0.310	[5]	0.3474	[0.57]	12.06
	500	0.117	[5]	0.1459	[0.62]	24.70
3804	600	0.0542	[5]	0.0583	[0.71]	7.56
	700	0.0244	[5]	0.0249	[0.72]	2.05

¹ Calculated relative error is the one-sigma statistical uncertainty for the Monte Carlo simulation and does not include uncertainties related to benchmark specifications.

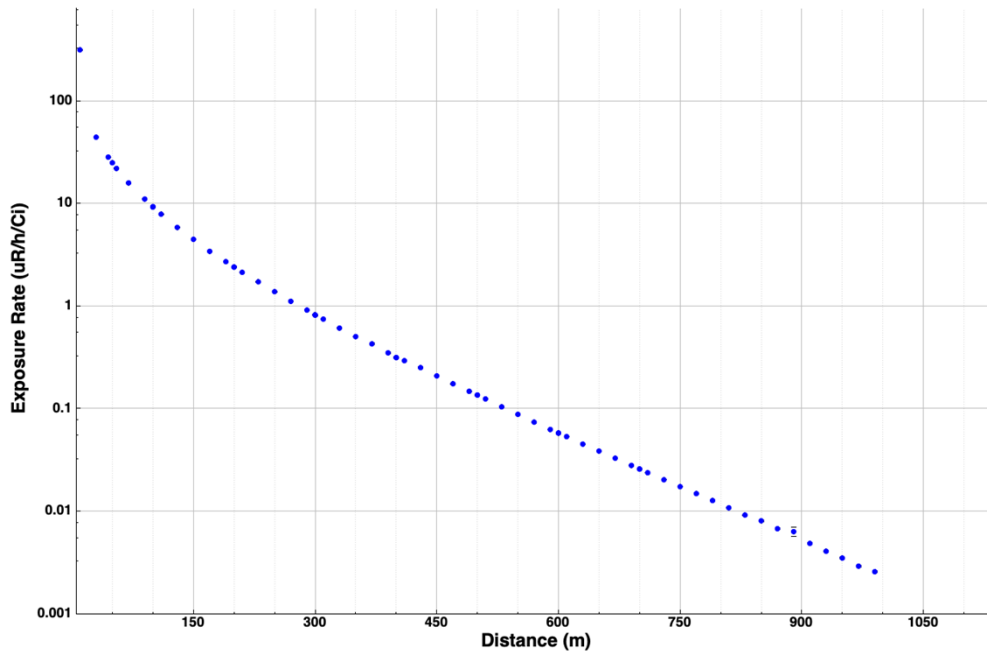


Figure 93. Radial distribution of the exposure rate calculated by MAVRIC for the source with 3804 Ci activity.

2.8 SILENE CRITICAL ASSEMBLY BENCHMARK

The SILENE benchmark experiments were a collaboration between the US Department of Energy (DOE) and the French Commissariat à l’Energie Atomique (CEA). The experiments were performed in 2010 in the SILENE critical assembly facility at CEA Valduc. The SILENE critical assembly is a uranyl nitrate solution with 93.5 wt% enriched ^{235}U . The goals of the experiments were (1) to measure neutron and gamma doses from critical pulses of SILENE under different shielding conditions and with different materials to replicate criticality accident conditions and (2) to perform CAAS validation and analysis. In Pulse 1, SILENE was bare (no shielding); in Pulse 2, a lead shield reflected the neutrons, and in Pulse 3, a polyethylene shield reflected the neutrons. Numerous publications originated from this work [40-43], including publications in the ICSBEP handbook entitled ALARM-TRAN-AIR-SHIELD-001 for the bare pulse, ALARM-TRAN-PB-SHIELD-001 for the lead reflected pulse, and ALARM-TRAN-CH2-SHIELD-001 for the polyethylene pulse. In this report, only some of the benchmark measurements are used: Pulse 1 (bare reactor) with only Collimator A (CA) and free field (FF) neutron foil activation analysis, and Pulses 2 and 3. Additional measurements from Pulse 3 will be included in the SCALE 6.3 validation report and in future validation reports.

2.8.1 Benchmark Model

The experiments included three configurations in which the SILENE reactor is at the center of a room and is surrounded by detection equipment. The first Pulse 1 configuration had no shielding, whereas the second Pulse 2 configuration was shielded by lead, and the final Pulse 3 configuration was shielded by polyethylene. These configurations were used to investigate the impacts of shielding materials in CAASs. The experimental setup used in the Pulse 1 bare reactor benchmark is shown in Figure 94. Neutron activation foils and thermoluminescent dosimeters (TLDs) were used to measure neutron reaction rates and gamma dose rates at various locations where the shielding materials and reflectors would have an impact on the count rates.



Figure 94. Experimental setup for SILENE Pulse 1 [43].

Pulse 1, the unshielded configuration, was chosen as a validation case for this report. The SCALE model of Pulse 1 is shown below in Figure 95. Measurements were taken for neutron activation reactions and gamma dose rates at each collimator, scattering box, and FF location. However, only CA and FF neutron foil activation measurements were analyzed in this report. The remaining locations and measurements are anticipated to be included in future validation studies. Neutron activation foils included high purity nickel, gold, indium, titanium, iron, manganese, and cobalt.

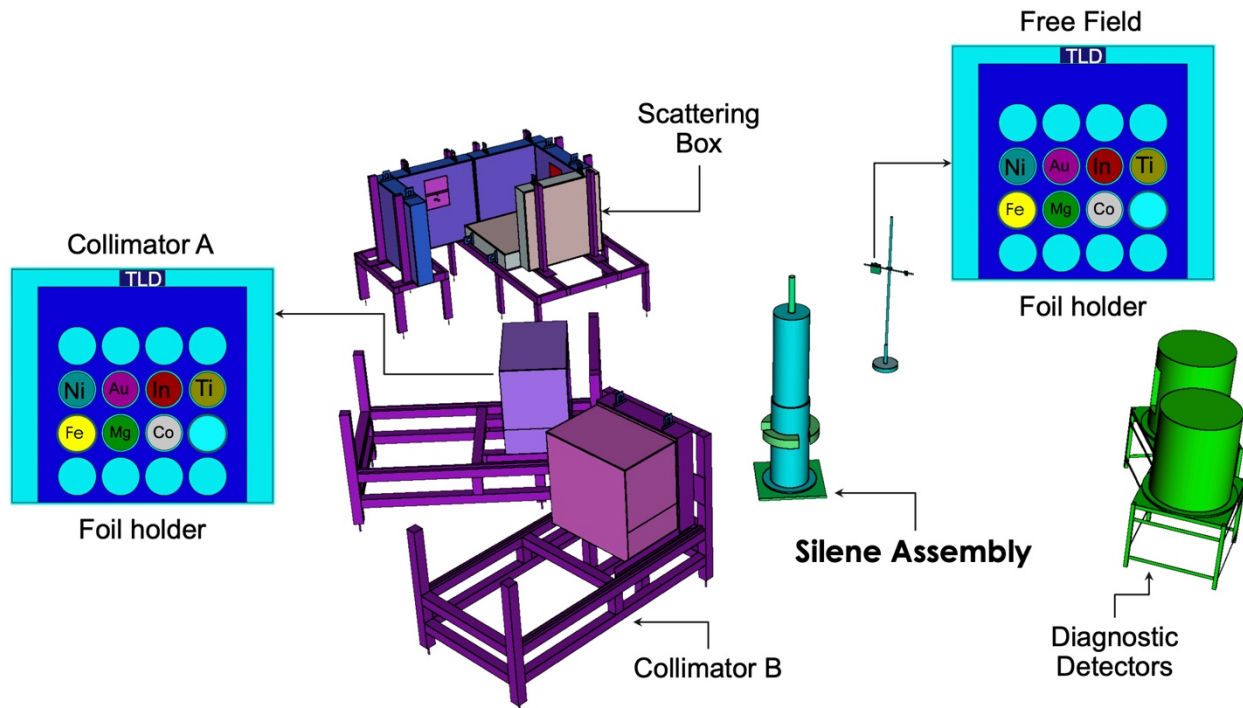


Figure 95. Benchmark model of SILENE Pulse 1.

The simplified SILENE assembly model is shown in Figure 96, and the measured fission rate spectrum for Pulse 1, measured by the diagnostic detectors, is shown in Figure 97. The assembly is modeled with cylindrical blocks of uranyl nitrate solution, upper and lower air tanks, and the control rod on top of the assembly. The pulse lasted around 30 seconds and yielded 1.88×10^{17} fissions.

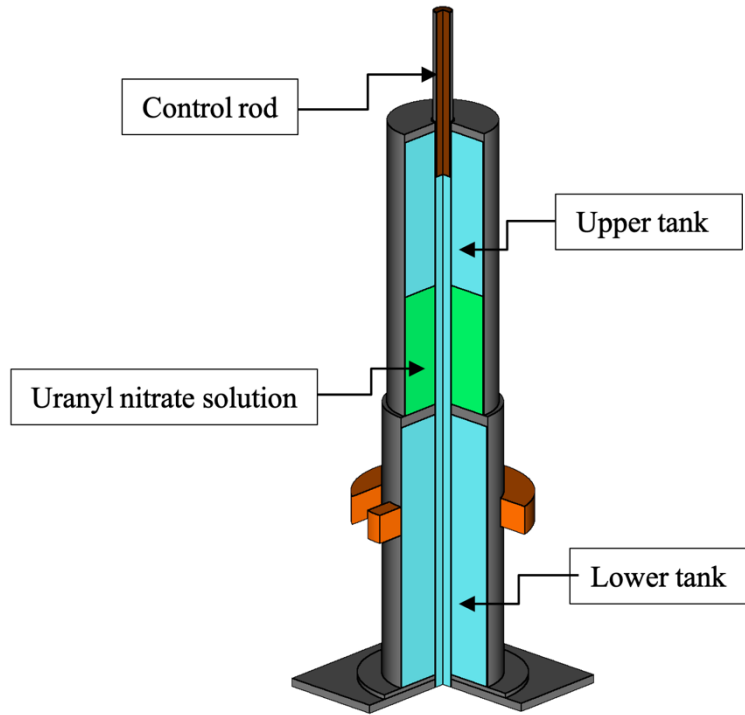


Figure 96. SILENE assembly model.

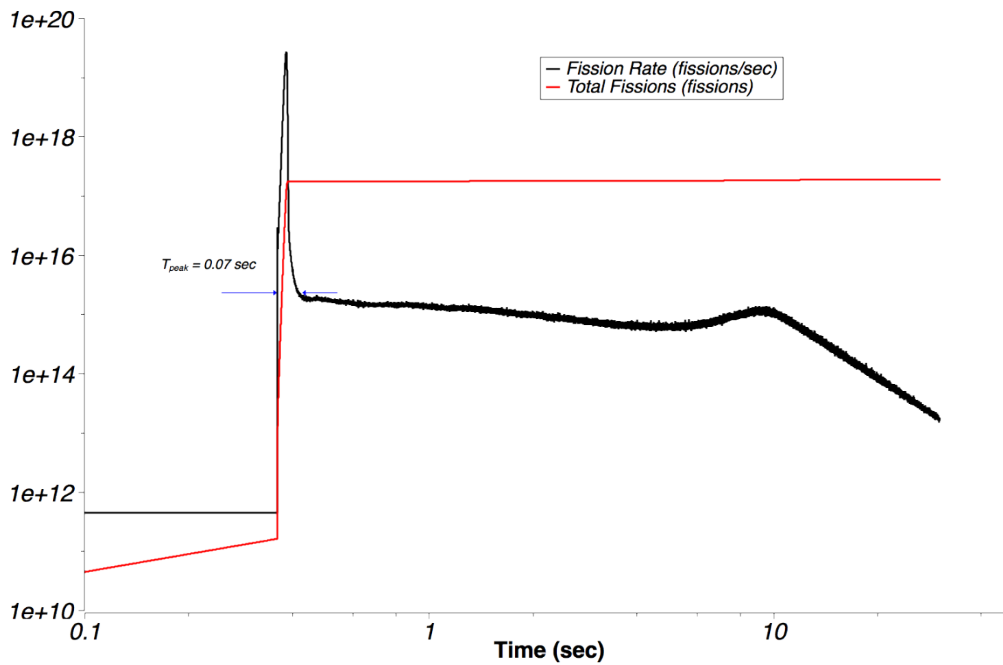


Figure 97. Fission rate spectrum for SILENE Pulse 1 [43].

2.8.2 Benchmark Results

The neutron activation measurements for Collimator A with SILENE Pulse 1 had an overall experimental uncertainty of approximately 7%, which was dominated by the uncertainty in the number of fissions [43]. Similarly, the FF measurements had an overall experimental uncertainty of approximately 7%. The gold foil measurement result at CA was believed to be erroneous and was disregarded during the validation of the SILENE benchmark [43]. The high-density concrete shields and impurities in the foils, particularly the iron foils, can be listed as other sources of uncertainties and discrepancies in the neutron activation results. The SCALE model employed the ENDF/B-VII.1 cross section libraries in this study, and responses generated from the International Reactor Dosimetry File (IRDF) [44] for the reactions of interest in the measurements were also included. The IRDF responses were included because of their better consistency and agreement with the measurements, including time-dependent and integrated reaction rates, whereas the ENDF/B cross section libraries represent prompt responses of the neutron reactions. The simulation results agree mostly within the experimental uncertainties of the benchmark measurements, as shown in

Table 25. Other than the uncertainties in the measurements, some of the discrepancies can be explained by accounting for only the prompt fission neutrons in the calculations while ignoring delayed neutron components that were known to contribute to activation results. However, it is difficult to model and quantify impacts of delayed neutrons since the fuel solution was drained after the pulse and no reactivity or solution height measurements were taken while draining the solution tank.

Table 25. Comparison of SILENE Pulse 1 benchmark results using IRDF [44] responses.

Position	Reaction	Activity (Bq/g)				C/E
		Measured [relative error %]		Calculated [relative error %] ²		
Collimator A	⁵⁹ Co (n,γ) ⁶⁰ Co	6.610e1	[2.57]	7.301e1	[1.23]	1.10
	¹¹⁵ In (n,γ) ¹¹⁶ In	9.110e6	[3.84]	9.646e6	[1.04]	1.06
	¹¹⁵ In (n,n'γ) ^{115m} In	8.030e3	[3.11]	7.905e3	[0.43]	0.98
	⁵⁴ Fe (n,p) ⁵⁴ Mn	2.062e-1	[3.98]	2.189e-1	[0.72]	1.06
	⁵⁶ Fe (n,p) ⁵⁶ Mn + ⁵⁵ Mn (n,γ) ⁵⁶ Mn	2.310e3	[2.64]	2.405e3	[1.87]	1.04
	²⁴ Mg (n,p) ²⁴ Na	6.110e1	[3.76]	7.114e1	[3.02]	1.16
	⁵⁸ Ni (n,p) ⁵⁸ Co	1.436e1	[3.06]	1.456e1	[0.70]	1.01
Free field	⁵⁹ Co (n,γ) ⁶⁰ Co	6.620e1	[2.42]	7.676e1	[1.44]	1.16
	¹⁹⁷ Au (n,γ) ¹⁹⁸ Au	6.950e4	[3.02]	7.790e4	[1.44]	1.12
	¹¹⁵ In (n,γ) ¹¹⁶ In	8.780e6	[4.90]	9.193e6	[1.27]	1.05
	¹¹⁵ In (n,n'γ) ^{115m} In	6.860e3	[3.21]	6.817e3	[0.58]	0.99
	⁵⁴ Fe (n,p) ⁵⁴ Mn	1.961e-1	[4.13]	2.012e-1	[0.91]	1.03
	⁵⁶ Fe (n,p) ⁵⁶ Mn + ⁵⁵ Mn (n,γ) ⁵⁶ Mn	2.403e3	[2.79]	2.603e3	[1.28]	1.08
	²⁴ Mg (n,p) ²⁴ Na	5.910e1	[4.06]	6.970e1	[3.95]	1.18
⁵⁸ Ni (n,p) ⁵⁸ Co	1.299e1	[3.16]	1.359e1	[0.87]	1.05	

² Calculated relative error is the one-sigma statistical uncertainty for the Monte Carlo simulation and does not include uncertainties related to benchmark specifications.

3. SUMMARY

MAVRIC is the main radiation shielding analysis tool in the SCALE code suite. It has been extensively used around the world for a wide range of shielding applications. In this first version of the SCALE validation report for shielding, SCALE v6.2.4 was tested against eight benchmark experiments. SCALE MAVRIC models were either used from previous publications or were developed specifically for this study. Of all the cases tested, outside of rare outliers, the MAVRIC calculations generally agree with the experimental results within 50%. Outlier cases with significant discrepancies are discussed in the text and are commonly attributed to unknown materials or dimensions from the benchmark description. In some cases, an MCNP benchmark already existed and was also compared to the MAVRIC results. Code-to-code comparisons generally agree within 20% relative error, indicating issues related to modeling, measurement, or nuclear data when there are discrepancies between simulated and measured results. Based on comparisons of SCALE results with experimental measurements and MCNP results as described in this report, SCALE v6.2.4 is considered to be validated for radiation shielding analyses. In future validation reports, additional cases will be added from validated benchmarks, as noted for the SILENE benchmark in Section 2.8. Furthermore, other benchmarks will be added to the report, such as a benchmark with fission rates from a fission chambers experiment involving platinum, which will only be available in ENDF/B-VIII.0 in SCALE v6.3. Finally, more SCALE model renderings and data visualizations for some benchmark cases will be added in subsequent reports.

4. REFERENCES

- [1] W. A. Wieselquist, R. A. Lefebvre, and M. A. Jessee, Eds., "SCALE Code System," Oak Ridge National Laboratory, Oak Ridge, TN, ORNL/TM-2005/39, Version 6.2.4, 2020.
- [2] D. E. Peplow, "Monte Carlo Shielding Analysis Capabilities with MAVRIC," *Nuclear Technology*, vol. 174, no. 2, pp. 289-313, 2011.
- [3] T. M. Evans, A. S. Stafford, R. N. Slaybaugh, and K. T. Clarno, "Denovo: A New Three-Dimensional Parallel Discrete Ordinates Code in SCALE," *Nuclear Technology*, vol. 171, no. 2, pp. 171-200, 2010, doi: 10.13182/NT171-171.
- [4] A. Haghghat and J. C. Wagner, "Monte Carlo Variance Reduction with Deterministic Importance Functions," *Progress in Nuclear Energy*, vol. 42, pp. 25-53, 2003.
- [5] J. C. Wagner, E. D. Blakeman, and D. E. Peplow, "Forward-Weighted CADIS Method for Global Variance Reduction," *Transactions of the American Nuclear Society*, vol. 97, pp. 630-633, 2007.
- [6] M. B. Chadwick *et al.*, "ENDF/B-VII.1 Nuclear Data for Science and Technology: Cross Sections, Covariances, Fission Product Yields and Decay Data," *Nuclear Data Sheets*, vol. 112, no. 12, pp. 2887-2996, 2011, doi: <https://doi.org/10.1016/j.nds.2011.11.002>, accessed February 2021.
- [7] T. Goorley *et al.*, "Initial MCNP6 Release Overview," *Nuclear Technology*, vol. 180, pp. 298-315, 2012.
- [8] "International Handbook of Evaluated Criticality Safety Benchmark Experiments," NEA Nuclear Science Committee, NEA/NSC/DOC(95)03, 2016.
- [9] I. Kodeli, A. Milocco, P. Ortego, and E. Sartori, "20 years of SINBAD (Shielding Integral Benchmark Archive and Database)," *Progress in Nuclear Science and Technology*, vol. 4, pp. 308-311, 2014.
- [10] E. Sajo, M. L. Williams, and M. Asgari, "Comparison of Measured and Calculated Neutron Transmission Through Steel for a ^{252}Cf Source," *Annals of Nuclear Energy*, vol. 20, no. 9, pp. 585-604, 1993.
- [11] K. Banarjee, C. Celik, G. G. Davidson, T. M. Evans, B. T. Rearden, and W. A. Wieselquist, "The MAVRIC-Shift Sequence in SCALE for Radiation Transport and Shielding Calculations with Automated Variance Reduction and Parallel Computing," Oak Ridge National Lab.(ORNL), Oak Ridge, TN (United States), ORNL/TM-2019/1358, 2019.
- [12] P. F. Rose (ed.), "ENDF/B-VI Summary Documentation," Brookhaven National Laboratory, BNL-NCS-17541 (ENDF-201), 1998.
- [13] B. Janský, Z. Turzík, E. Novák, J. Kyncl, F. Cvachovec, and P. Tiller, "Comparison of Measured and Calculated Neutron Transmission Through Heavy Water for ^{252}Cf Source Placed in the Center of 30 cm Diameter Sphere," *Annals of Nuclear Energy*, vol. 24, no. 15, pp. 1189-1212, 1997.
- [14] R. J. McConn, C. J. Gesh, R. T. Pagh, R. A. Rucker, and R. Williams III, *Compendium of Material Composition Data for Radiation Transport Modeling*, Pacific Northwest National Laboratory (PNNL), Richland, WA (United States), PNNL-15870 Rev. 1, March 2011.
- [15] W. Mannhart, "Status of the Cf-252 fission neutron spectrum evaluation with regard to recent experiments," International Atomic Energy Agency (IAEA), 1989. Accessed: February 2021. [Online]. Available: http://inis.iaea.org/search/search.aspx?orig_q=RN:20083146, accessed February 2021.

- [16] D. E. Peplow, K. Banerjee, G. G. Davidson, I. R. Stewart, M. W. Swinney, and J. N. Wagner, "Preliminary Validation of the Shift Monte Carlo Code for Fixed-Source Radiation Transport Problems," *Nuclear Technology*, vol. 206, no. 1, pp. 107-125, 2020, doi: 10.1080/00295450.2019.1625663.
- [17] D. E. Peplow and C. R. Daily, "Comparison of ADVANTG Simulations to Simple Shielding Measurements," presented at the ANS RPSD 2014 - 18th Topical Meeting of the Radiation Protection & Shielding Division of ANS, Knoxville, TN, Sept. 14 – 18, 2014.
- [18] J. Risner, D. Wiarda, M. Dunn, T. Miller, D. Peplow, and B. Patton, "Production and Testing of the VITAMIN-B7 Fine-Group and BUGLE-B7 Broad-Group Coupled Neutron/Gamma Cross-Section Libraries Derived from ENDF/B-VII.0 Nuclear Data," U.S. Nuclear Regulatory Commission, NUREG/CR-7045, Oak Ridge National Lab.(ORNL), Oak Ridge, TN (United States), Agency Document Access and Management System (ADAMS) Accession No. ML11294A199, 2011.
- [19] D. Wiarda, M. E. Dunn, D. E. Peplow, T. M. Miller, and H. Akkurt, "Development and Testing of ENDF/B-VI.8 and ENDF/B-VII.0 Coupled Neutron-Gamma Libraries for SCALE 6," US Nuclear Regulatory Commission, Office of Nuclear Material Safety and Safeguards, Washington, DC, NUREG/CR-6990 ORNL/TM-2008/047, 2009.
- [20] M. Nikolaev, N. Prokhorova, and T. Ivanova, "Neutron Fields in Three-section Concrete Labyrinth from Cf-252 Source," in "International Handbook of Evaluated Criticality Safety Benchmark Experiments, Volume VIII—Criticality Alarm/Shielding Benchmarks," Organization for Economic Co-operation and Development/Nuclear Energy Agency, NEA/NSC/DOC/(95)03/VIII, 2007.
- [21] J. N. Wagner and D. E. Peplow, "Validation of the Shift Monte Carlo Code – Neutron Field Measurements in a Concrete Labyrinth," in *Transactions of the American Nuclear Society*, 2019, vol. 120, pp. 763–766. [Online]. Available: <https://www.osti.gov/biblio/1546531>, accessed February 2021.
- [22] D. Bogart, D. F. Shook, and D. Fieno, "Transport Analysis of Measured Neutron Leakage Spectra from Spheres as Tests of Evaluated High-Energy Cross Sections," *Nuclear Science and Engineering*, vol. 53, no. 3, pp. 285-303, 1974, doi: 10.13182/NSE74-A23354.
- [23] R. L. Alexander, D. Fieno, and C. H. Ford, "Tests of Evaluated Beryllium (n, 2n) Cross Sections by Analysis of 1.4-eV Flux in Water for an Americium-Beryllium Source Enclosed in Beryllium Spheres," *Nuclear Science and Engineering*, vol. 44, no. 1, pp. 95-102, 1971, doi: 10.13182/NSE71-A18909.
- [24] N. E. Hertel, "High-Energy Neutron Transport Through Tungsten and Iron," PhD Thesis, University of Illinois at Urbana-Champaign, 1979.
- [25] N. E. Hertel, R. H. Johnsons, B. W. Wehring, and J. J. Dorning, "Transmission of Fast Neutrons Through an Iron Sphere," *Fusion Technology*, vol. 9, no. 2, pp. 345-361, 1986, doi: 10.13182/FST86-A24721.
- [26] M. L. Williams, C. Aboughantous, M. Asgari, J. E. White, R. Q. Wright, and F. B. K. Kam, "Transport Calculations of Neutron Transmission Through Steel Using ENDF/B-V, Revised ENDF/B-V and ENDF/B-VI Iron Evaluations," *Annals of Nuclear Energy*, vol. 18, no. 10, pp. 549-565, 1991, doi: [https://doi.org/10.1016/0306-4549\(91\)90055-3](https://doi.org/10.1016/0306-4549(91)90055-3), accessed February 2021.
- [27] SINBAD, "University of Illinois Iron Sphere Benchmark (1975)," NEA-1553/26 SBE 13.00, 2006, vol. August 2006 update. Accessed: February 2021. [Online]. Available: <https://www.oecd-nea.org/science/wprs/shielding/sinbad/sinbadis.htm>, accessed February 2021.

- [28] K. Ueki, A. Ohashi, and Y. Anayama, "Neutron Shielding Ability of KRAFTON N2 - Mannan - KRAFTON N2 Sandwich-type Material and Others," *Proc. Topical Mtg. on New Horizons in Radiation Protection and Shielding*, ANS, Pasco, 1992.
- [29] K. Ueki *et al.*, "Systematic Evaluation of Neutron Shielding Effects for Materials," *Nuclear Science and Engineering*, vol. 124, no. 3, pp. 455-464, 1996, doi: 10.13182/NSE124-455.
- [30] F. H. Fröhner, "Evaluation of ^{252}Cf Prompt Fission Neutron Data from 0 to 20 MeV by Watt Spectrum Fit," *Nuclear Science and Engineering*, vol. 106, no. 3, pp. 345-352, 1990, doi: 10.13182/NSE89-177.
- [31] *American National Standard: Neutron and Gamma-Ray Flux-to-Dose-Rate Factors*, ANSI/ANS-6.1.1-1977 (N666), A. N. S. S. C. W. G. ANS-6.1.1, United States, March 17, 1977. [Online]. Available: <https://www.osti.gov/biblio/5538262>, accessed February 2021.
- [32] *American National Standard for Neutron and Gamma-Ray Fluence-to-Dose Factors*, ANSI/ANS-6.1.1-1991, A. N. S. S. C. W. G. ANS-6.1.1, United States, August 26, 1991. [Online]. Available: <https://www.osti.gov/biblio/5538262>, accessed February 2021.
- [33] ICRU, "ICRU Report 57: Conversion Coefficients for use in Radiological Protection Against External Radiation," International Commission of Radiation Units and Measurements, Bethesda, MD, 1998.
- [34] N. Petoussi-Hens *et al.*, "Conversion Coefficients for Radiological Protection Quantities for External Radiation Exposures," *Annals of the ICRP*, vol. 40, no. 2-5, pp. 1-257, March 1, 2010, doi: 10.1016/j.icrp.2011.10.001.
- [35] C. J. Solomon, A. Sood, and R. D. Mosteller, "A study of a polyethylene and stainless steel composite deep shield benchmark of MCNP," ANS 14th Biennial Topical Meeting of the Radiation Protection and Shielding Division of the American Nuclear Society, LA-UR-06-2349 (text) and LA-UR-06-2350 (slides) April 3-6, 2006.
- [36] M. L. Roseberry, "Benchmark Skyshine Exposure Rates," Master of Science, Nuclear Engineering, Kansas State University, 1980.
- [37] E. D. Blakeman, "Photon Skyshine Experiment Benchmark," in *2010 ANS RPSD, IRD & BMD Joint Topical Meeting*, Las Vegas, NV, ANS, Ed., April 19-23 2010: ANS.
- [38] R. R. Nason, J. K. Shultis, R. E. Faw, and C. E. Clifford, "A Benchmark Gamma-Ray Skyshine Experiment," *Nuclear Science and Engineering*, vol. 79, no. 4, pp. 404-416, 1981, doi: 10.13182/NSE81-A21391.
- [39] R. H. Olsher, H.-H. Hsu, and W. F. Harvey, "Benchmarking the MCNP Monte Carlo Code with a Photon Skyshine Experiment," *Nuclear Science and Engineering*, vol. 114, no. 3, pp. 219-227, 1993, doi: 10.13182/NSE93-A24035.
- [40] T. M. Miller *et al.*, "Evaluation of the concrete shield compositions from the 2010 criticality accident alarm system benchmark experiments at the CEA Valduc SILENE facility," in *ICNC 2015 - International Conference on Nuclear Criticality Safety*, 2015, pp. 1647-1658. [Online]. Available: <https://www.osti.gov/biblio/1215597>, accessed February 2021.
- [41] T. M. Miller *et al.*, "Neutron Activation Foil and Thermoluminescent Dosimeter Responses to a Lead Reflected Pulse of the CEA Valduc SILENE Critical Assembly," Oak Ridge National Lab. (ORNL), Oak Ridge, TN (United States), ORNL/TM-2016/316; Other: DP0909010; DPDP097; alarm-tran-pb-shield-001; TRN: US1700292 United States 10.2172/1326508, 2016. Accessed: February 2021. [Online]. Available: <https://www.osti.gov/servlets/purl/1326508>, accessed February 2021.

- [42] T. M. Miller *et al.*, "Neutron Activation Foil and Thermoluminescent Dosimeter Responses to a Polyethylene Reflected Pulse of the CEA Valduc SILENE Critical Assembly,"; Oak Ridge National Lab. (ORNL), Oak Ridge, TN (United States), ORNL/TM-2016/317; Other: DP0909010; DPDP097; alarm-tran-ch2-shield-001; TRN: US1700310 United States 10.2172/1327663, 2016. [Online]. Available: <https://www.osti.gov/servlets/purl/1327663>, accessed February 2021.
- [43] T. M. Miller *et al.*, "Neutron Activation and Thermoluminescent Detector Responses to a Bare Pulse of the CEA Valduc SILENE Critical Assembly,"; Oak Ridge National Lab. (ORNL), Oak Ridge, TN (United States), ORNL/TM-2015/462; Other: DP0902090; DPDP097; alarm-tran-air-shield-001 United States 10.2172/1224756, 2016. [Online]. Available: <https://www.osti.gov/servlets/purl/1224756>, accessed February 2021.
- [44] *International Reactor Dosimetry File 2002 (IRDF-2002)*. Vienna: INTERNATIONAL ATOMIC ENERGY AGENCY, 2006.

